5-1-2013

In situ measurement, characterization, and modeling of two-phase pressure drop incorporating local water saturation in PEMFC gas channels

Evan See

R·I·T | KATE GLEASON *College of* ENGINEERING

In Situ Measurement, Characterization, and Modeling of Two-Phase Pressure Drop Incorporating Local Water Saturation in PEMFC Gas Channels

by

Evan J. See

A Thesis Submitted in Partial Fulfillment of the Requirements for the Degree of

MASTER OF SCIENCE
in
MECHANICAL ENGINEERING

DEPARTMENT OF MECHANICAL ENGINEERING
KATE GLEASON COLLEGE OF ENGINEERING
ROCHESTER INSTITUTE OF TECHNOLOGY
ROCHESTER, NY 14623
MAY 2013

Approved by:

Dr. Satish G. Kandlikar	Date
Thesis Advisor	
Professor, Department of Mechanical Engineering	

Dr. Mario W. Gomes	Date
Committee Member	
Professor, Department of Mechanical Engineering	

Dr. Jason R. Kolodziej	Date
Committee Member	
Professor, Department of Mechanical Engineering	

Dr. Agamemnon L. Crassidis	Date
Department Representative	
Professor, Department of Mechanical Engineering	

I. Abstract

Proton Exchange Membrane Fuel Cells (PEMFCs) have been an area of focus as an alternative for internal combustion engines in the transportation sector. Water and thermal management techniques remain as one of the key roadblocks in PEMFC development. The ability to model two-phase flow and pressure drop in PEMFCs is of significant importance to the performance and optimization of PEMFCs. This work provides a perspective on the numerous factors that affect the two-phase flow in the gas channels and presents a comprehensive pressure drop model through an extensive in situ fuel cell investigation. The study focused on low current density and low temperature operation of the cell, as these conditions present the most challenging scenario for water transport in the PEMFC reactant channels. Tests were conducted using two PEMFCs that were representative of the actual full scale commercial automotive geometry. The design of the flow fields allowed visual access to both cathode and anode sides for correlating the visual observations to the two-phase flow patterns and pressure drop.

A total of 198 tests were conducted varying gas diffusion layer (GDL), inlet humidity, current density, and stoichiometry; this generated over 1500 average pressure drop measurements to develop and validate two-phase models. A two-phase 1+1 D modeling scheme is proposed that incorporates an elemental approach and control volume analysis to provide a comprehensive methodology and correlation for predicting two-phase pressure drop in PEMFC conditions. Key considerations, such as condensation within the channel, consumption of reactant gases, water transport across the membrane, and thermal gradients within the fuel cell, are reviewed and their relative importance illustrated. The modeling scheme is shown to predict channel pressure drop with a mean error of 10% over the full range of conditions and with a mean error of 5% for the primary conditions of interest. The model provides a unique and comprehensive basis for developing a fundamental adiabatic two-phase flow pressure drop predictive scheme for PEMFC reactant channels.

II. Acknowledgments

I would like to express my deep gratitude for the opportunities and guidance that my advisor, Dr. Satish Kandlikar, provided throughout my research and beyond. The knowledge and skills that I have developed as a result of his support exceed that of what I could have expected to learn. His endless enthusiasm for the pursuit of knowledge and his students has been a continuous inspiration.

I would also like to thank my fellow members of the Thermal Analysis, Microfluidics, and Fuel Cell Lab. Their discussions, insight, unique perspectives, and support helped to shape my work and provided numerous learning opportunities. I would also like to acknowledge the support of the entire Mechanical Engineering Department staff that provided an amazing work environment and supported me throughout every step of my research.

This work was supported by US Department of Energy under contract no. DE-EE0000470 through General Motors. The input from General Motors Electrochemical Energy Research Laboratory is greatly appreciated and this work could not have been completed without their support.

I would also like to thank my family for their unending support. Without my parents', David and Cynthia, guidance and encouragement throughout the challenges and obstacles I would not have been able to reach this point. I would also like to thank my brother, Brendan, whose advice and competition has compelled me to aim for perfection in everything I do. This work is dedicated to my grandmother, Madeline Mahran, who taught me the importance of instilling quality in everything that I do. Her love, support, and advice has driven me to strive for the absolute best in every action I take.

Contents

III. Table of Figures

IV. Index of Tables

V. Nomenclature

Abbreviation	Description
BA	Baseline
BPP	Bipolar plate
CCM	Catalyst coated membrane
CL	Catalyst layer
FR	Freudenberg
GDL	Gas diffusion layer
MEA	Membrane electrode assembly
MPL	Microporous layer
OCV	Open circuit voltage
PEM	Proton exchange membrane
PFSA	Perfluorosulfonic acid
PTFE	Polytetrafluoroethylene
RH	Relative humidity
Stoich	Stoichiometry

Symbol	Description
A_r	Active reaction area, m^2
A_c	Cross-sectional Area, m^2
C	Chisholm parameter
D_h	Hydraulic diameter, m
F	Faraday constant, C/mol
fRe	Frictional factor, Reynolds number product (=Po, Poiseuille number)
i	Current density, A/m^2
j	Superficial Velocity, m/s

L	Length, m
M	Molecular mass,
m	Fraction of product water to cathode
n	Number of electron per mole species
P	Pressure, Pa
T	Temperature, °K
W	Mass flux, kg/s
x	Mass quality ratio
Φ	Two-phase multiplier
μ	Viscosity, kg/ms^2
ρ	Density, kg/m^3
X	Martinelli parameter

Subscript	**Description**
An	Anode
Ca	Cathode
g	Gaseous phase
k	Element number
l	Liquid phase
R	Reaction
tot	Total

1. Introduction

With increasing focus on energy independence and environmental concerns alternative fuel sources for transportation application have been an area of focus. Proton exchange membrane fuel cells (PEMFCs) offer many advantages for use in transportation applications. Their low operating temperature, relatively rapid start time, ability to have supply tanks quickly refilled, and clean operation make them excellent candidates. PEMFCs are electrochemical energy conversion devices, which utilize hydrogen and oxygen to create energy, water, and heat. The half reactions that take place within the PEMFC are as follows:

$$\text{Anode: } H_2 \rightarrow 2H^+ + 2e^- \tag{1.1}$$

$$\text{Cathode: } \frac{1}{2}O_2 + 2H^+ + 2e^- \rightarrow H_2O \tag{1.2}$$

$$\text{Net cell reaction: } H_2 + \frac{1}{2}O_2 \rightarrow H_2O + \text{waste heat} + \text{electrical energy} \tag{1.3}$$

Figure 1 shows a schematic of a typical PEMFC, identifying key PEMFC components. The function and relative thickness of each component are described in Table I.

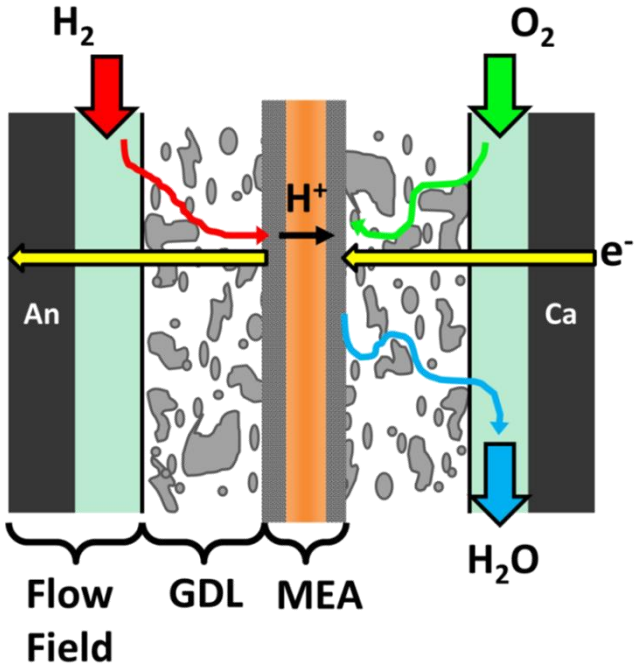

Figure 1 – Schematic of PEMFC component and electrochemical reaction. Not to scale.

In the PEMFC, the reactants (hydrogen and oxygen) are delivered to anode and cathode gas channels through the manifolds at the end of each cell. The reactants flow through the flow field and diffuse through the porous gas diffusion layer (GDL) and microporous layer (MPL), reaching the membrane electrode assembly (MEA). The MEA is the combined cathode and anode catalyst layers (CL) and the proton exchange membrane (PEM). In the anode CL, hydrogen gas is decomposed through oxidation into H^+ and electrons. The H^+ are transported through the PEM. The electrons are conducted through the GDL and bipolar plates (BPP) through an external circuit and back to the cathode BPP and GDL, thus creating usable current. In the cathode CL, O_2 reacts with H^+ from the PEM and electrons from the external circuit, producing water. The product water and reactants are then removed through the GDL and flow field.

Table 1 – Key Components of PEMFCs and their function

Component	Thickness (μm)	Pore size	Primary Functions	Key Challenges
Proton Exchange Membrane	12 - 175	N/A	▪ Proton transport ▪ Electron insulation	▪ High temperature operation (>100 °C)
Catalyst Layer	5 - 30	~ 50 nm	▪ Reaction site	▪ Cost of precious metals
Microporous Layer	5 - 45	~100 nm	▪ Reduce contact resistance ▪ CL Protection	▪ Understanding mechanism of transport
Gas Diffusion Layer	175 - 400	100 – 500 μm	▪ Gas distribution ▪ Water removal ▪ Electron conduction	▪ Cost ▪ Performance of water removal
Flow Field	200 - 2000	N/A	▪ Gas distribution ▪ Water removal	▪ Contact resistance ▪ Optimal configuration
Bipolar Plate	1500 - 4000	N/A	▪ Electron conduction ▪ Heat removal ▪ Structural support	▪ Thickness/mass ▪ Corrosion

In order to understand the barriers to PEMFC performance, the electrochemistry which governs PEMFC operation should be reviewed to understand the fundamental reasons of losses and

inefficiencies. The performance of a PEMFC is characterized by the current and voltage at which it is operating as shown in Figure 2.

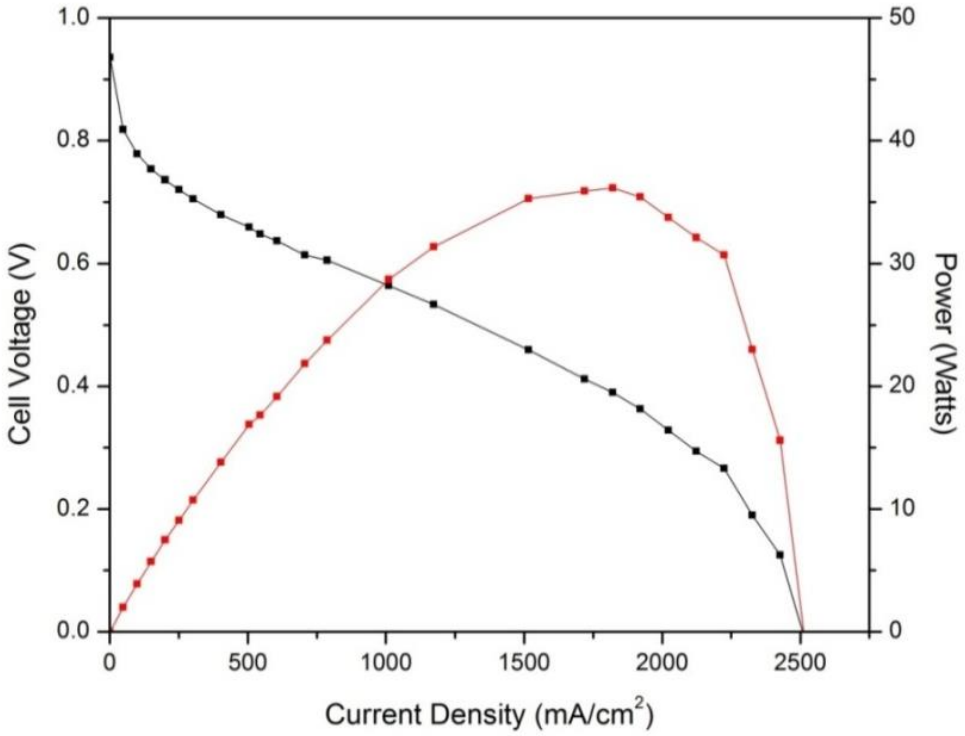

Figure 2 – Generic Polarization Curve

The real cell voltage can be expressed by the equation below

$$E_{cell} = E^o(T,P) - n_{a,a} - |n_{a,c}| - n_r - n_{m,a} - |n_{m,c}| - n_x \tag{1.4}$$

where:

$$\mathrm{E^o(T,P)} = \frac{-\Delta \mathrm{G^o(T)}}{\mathrm{nF}} + \frac{\mathrm{R_u T}}{\mathrm{nF}} \ln\left[\frac{\mathrm{a_{H_2}(a_{O_2})^{1/2}}}{\mathrm{a_{H_2O}}}\right] \tag{1.5}$$

Equation 1.5 represents the theoretical maximum for the PEMFC to operate at a set temperature and pressure. Additionally, the terms η_a, η_r, η_m, and η_x represent activation, resistance, mass transport, and crossover losses respectively. Although theoretical maximum voltage is primarily based on the ideal gas law, the effect of temperature on the entropy of the system is important. As temperature increases

the entropy of the system increases, thus the potential energy that can be utilized increases. This suggests that PEMFCs should be run at higher temperatures, however the traditionally used membranes cannot operate properly well above 80°C. This limits performance and potentially the efficiency of the fuel cell. Additionally, the effect of pressure is not directly seen in Equation 1.5. However, it is seen through the partial pressures and concentrations inside the natural log of Equation 1.5. This creates a need for forced "backpressure" to increased performance and pressurized gas flow. Thus a blower or compressor is needed to supply the gases, which adds considerable inefficiencies.

The activation losses (η_a) of a PEMFC are given by the Butler-Volmer Equation and its simplifications, which the full derivations have little influence on the overall performance characteristics. They are more simply linked to the activation losses or the performance of the MEA and the catalysts. By using improved materials or high platinum loadings, these losses can be minimized. However, the platinum required becomes both an economic and social concern on where it is sourced from.

Resistance losses (η_r) are given by summation of contact resistances, mostly ionic relative to electronic resistance in a properly made fuel cell. The resistance losses of a fuel cell are the simplest to understand and see the effect of on a fuel cell. The contact resistances of each component add to a total cell resistance, which creates a linear drop in the I-V curve.

$$\eta_r = iA\sum_{j=1}^{n} R_i; \tag{1.6}$$

The concentration losses (η_m) are also known as the "mass-transport" losses, which are based on the increasing resistance to the flow of reactants due to high flow rates. This also incorporates the resistance to mass flow created by liquid water in the fuel cell.

$$\eta_{m,a} + \eta_{m,c} = -B_a \ln\left[1 - \frac{i}{i_{l,a}}\right] - B_c \ln\left[1 - \frac{i}{i_{l,c}}\right] \tag{1.7}$$

The final key loss, crossover losses, simply quantifies the losses due to H_2 diffusing across the PEMFC membrane without reacting.

$$\eta_x = \frac{i_x A}{nF} \tag{1.8}$$

Water transport in PEM fuel cells presents issues due to the additional mass transport losses associated with two-phase flow: the combination of reactant gas, evaporated water, and liquid water. The liquid water in the PEMFC gas channel covers part of the area available for reaction, effectively reducing the usable size of the fuel cell channel-GDL interface, as shown in Figure 3. This diminishes fuel cell performance and limits the maximum current densities possible within the cell. This in-turn lowers the maximum power, and power density. Any improvement in water transport and management within the cell greatly improves its performance. Many methods to improve this have been attempted including changing the surface energy of the materials, different geometries for flow fields, and sizing of flow fields. Additionally, one of the simplest methods of removing liquid water is to increase the flow rates (and consequently the stoichiometric ratio). However, increased flow rates add weight, complexity, and inefficiency through wasted reactants and additional pumps. Additionally, the membrane requires a minimal hydration level, so this water balance must be actively maintained to prevent excess resistance losses.

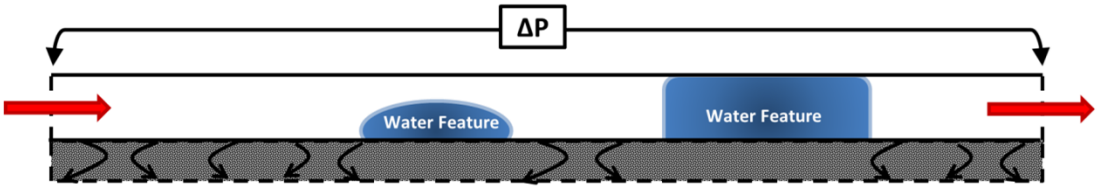

Figure 3 – Schematic of Transport within a PEMFC gas channel

Water and thermal management techniques remain as one of the key roadblocks in PEMFCs. The ability to model two-phase flow and pressure drop in PEMFCs is of significant importance to the fundamental study and optimization of PEMFC performance. Pressure drop has been repeatedly

linked to overall fuel cell performance as noted by Bosco and Fronk [1], and directly affects cost and sizing of fuel cell subsystems. Within several regions of PEMFC operating conditions the potential for flooding hinders potential performance and operation at high current densities is subject to potentially sizeable mass transport losses. These factors lead to the need for more complex systems and expensive blowers for reactant delivery. Increasing accuracy in pressure drop modeling within the PEMFC field can significantly reduce this need. Extensive review of two-phase flow in microchannels has been summarized by Anderson et al. [2] and Kandlikar et al. [3]. Fluid flow within PEMFCs is currently an extensively studied subject matter. This research is typically classified by the layer of the PEMFC that is being investigated. The areas of fluid flow research within the PEMFC community are summarized in Figure 4 with the areas investigated in this study highlighted in orange.

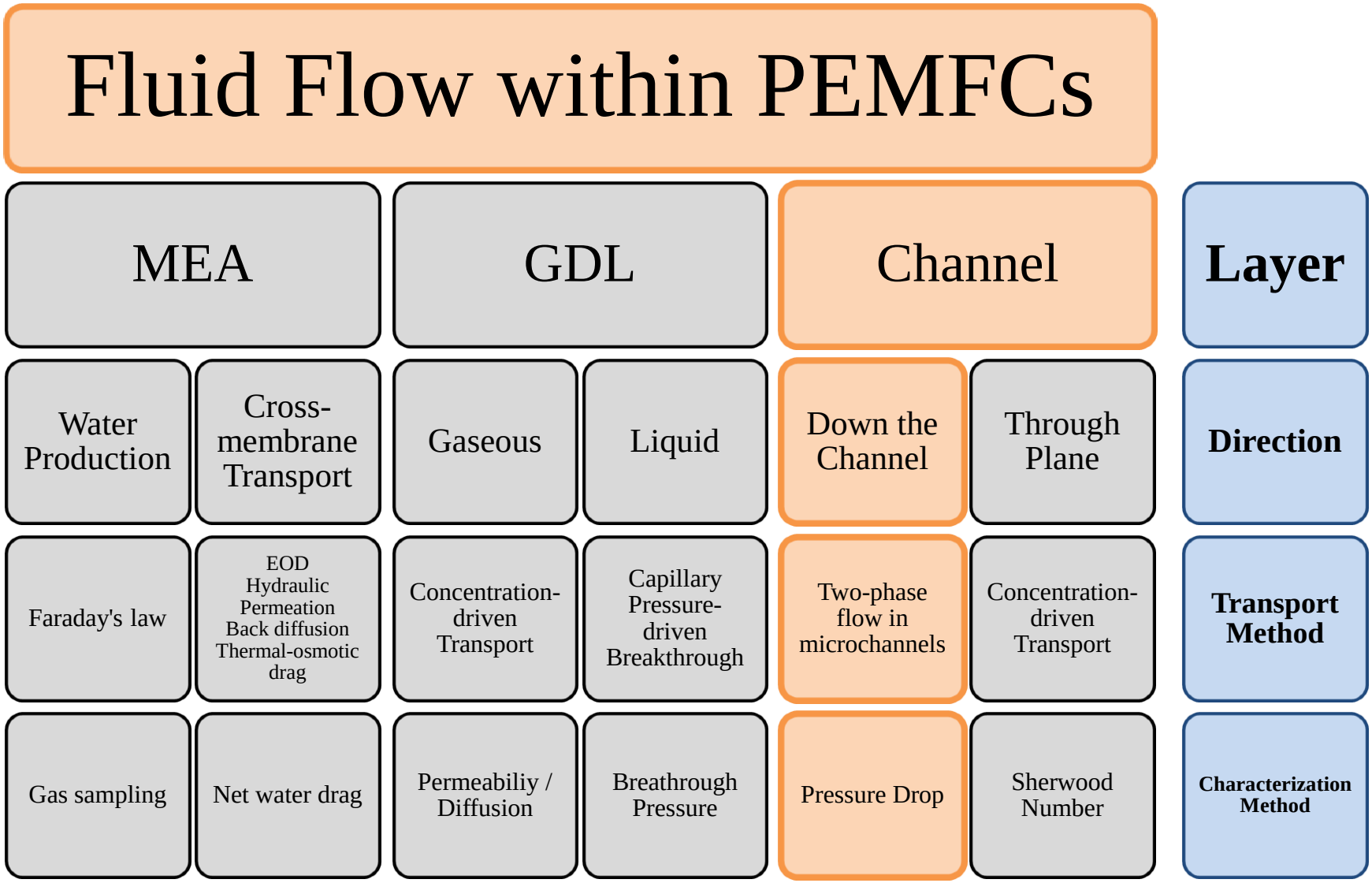

Figure 4 – Summary of Research in PEMFC Community on Fluid Flow

2. Literature Review

Down-the-channel (DTC) water transport in PEMFCs presents an issue due to the additional mass transport losses associated with two-phase flow: the combination of reactant gas, evaporated water, and liquid water. Two-phase flow can be divided into many different flow regimes, which were initially studied and classified by Mishima and Hibiki [4]. There are three main flow regimes of which are considered in this work: slug flow, film (annular) flow, and mist flow. The key differences between these flow regimes are characterized by the frequency of their pressure drop fluctuations and their two-phase multiplier, which scales the single-phase pressure drop based on flow conditions.

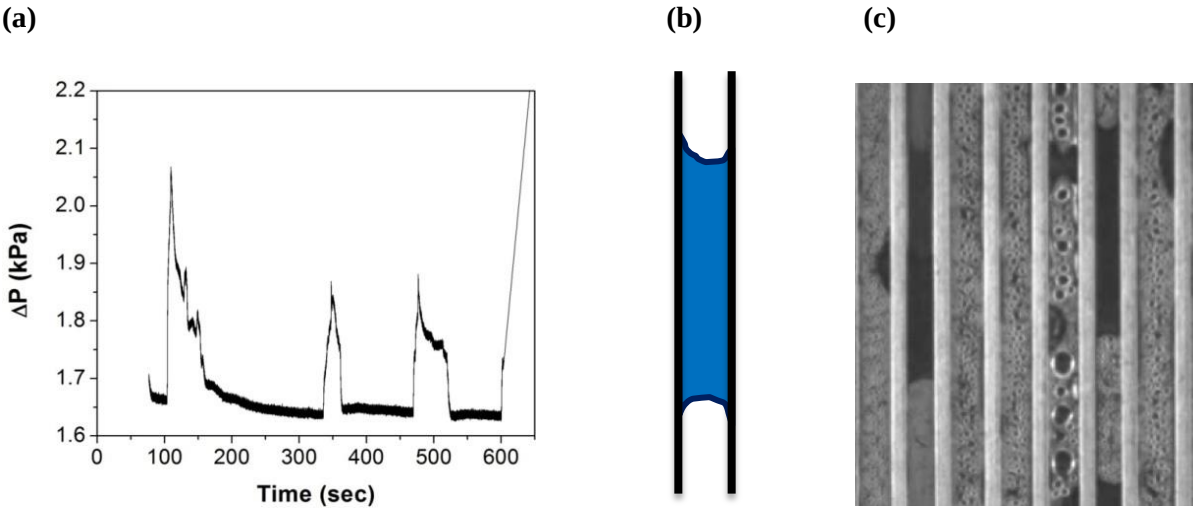

Figure 5 – Observations of Slug Flow

(a) Pressure drop signature of Slug flow (b) Schematic of Slug flow
(c) Image of Slugs in PEMFC channel

Slug flow is defined as large liquid plugs separated by relatively large gas pockets, in which the liquid plugs completely fill the channel geometry. Slug flow typically results in a higher two-phase pressure drop multiplier and low frequency fluctuations in the pressure drop of a system.

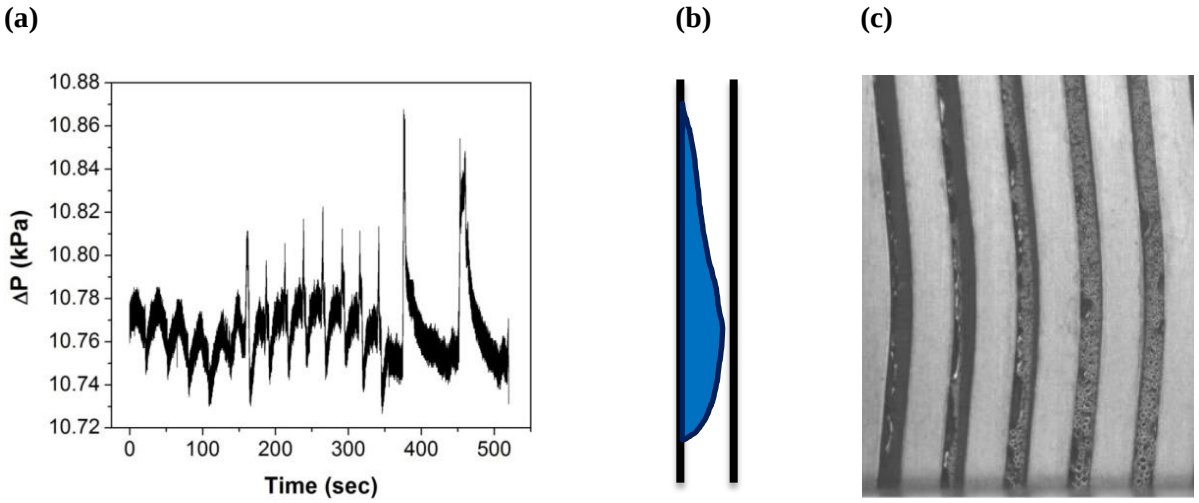

Figure 6 – Observations of Film Flow

(a) Pressure drop signature of Film flow (b) Schematic of Film flow
(c) Image of Films in PEMFC channel

Film flow is defined as liquid film on channel wall with significant gas pockets. These are typically annular in round channels or cover only one channel wall in rectangular geometries. Film flow typically causes a relatively low two-phase multiplier compared to slug flow, but induces higher frequency pressure drop fluctuations.

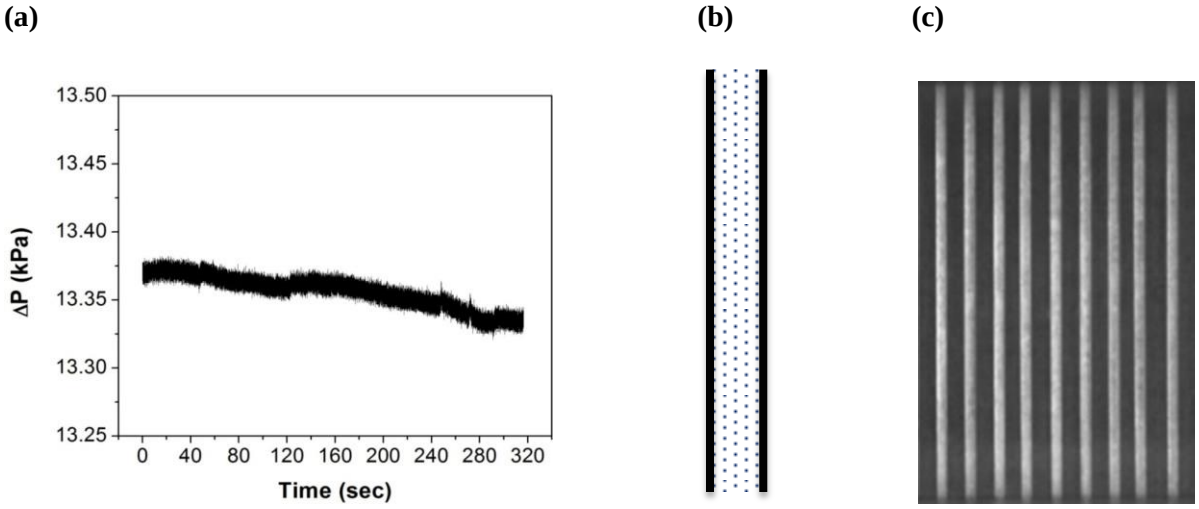

Figure 7 – Observations of Mist Flow

(a) Pressure drop signature of Mist flow (b) Schematic of Mist flow
(c) Image of Mist in PEMFC channel

Mist flow is defined as both phases being equally distributed throughout each other. Usually the liquid is entrained as very small droplets in the gas flow. Mist flow regularly has a two-phase multiplier close to one in PEMFC applications, and produces with minimal fluctuation in the pressure drop.

2.1. Pressure Drop Modeling

The water transport in a PEMFC most closely relates to the fundamental field of condensation within microchannels. A primary consideration in characterizing two-phase flow within channels is the method of flow through the channel. This flow pattern provides the foundation for the fundamental pressure drop and heat transfer characteristics. The majority of literature on two-phase flow regimes focuses on adiabatic flow, which can provide both benefit and potential pitfall for use in the PEMFC community. Primarily these experiments utilize working fluids of air-water or nitrogen-water at or near atmospheric conditions, which mimic that of the cathode of a PEMFC. However, the lack of heat of condensation and continuous addition of condensate should be noted [3]. Additionally, this literature focuses on simultaneous air and water introduction at the inlet of the channel [4–15], unlike PEMFCs which experience continuous water introduction. As the quality changes along the PEMFC microchannel, progression between different flow patterns is seen and develops distinct flow regimes. Scaling of large tube correlations for pressure drop do not yield accurate results due to the dissimilar comparative magnitude of the gravitational, viscous, and surface tension forces between large scale tubes and microchannels [3].

2.1.1. Notable Models

Two-phase pressure drop has been investigated from two fundamental perspectives, classified as either homogenous or separated models. In homogenous models, the superficial velocity of both phases is considered to be equal and it follows that the fluid properties are estimated by a two-phase density and viscosity. These correlations were well reviewed by Saisorn and Wongwises [5]. Notably,

Dukler [6] proposed the two-phase viscosity as a function of volumetric quality in applying homogeneous flow model.

Conversely, in separated flow models the superficial velocity of each phase is calculated separately. A two-phase multiplier is utilized based on flow conditions to scale the single-phase pressure drop. Most notably, this form of modeling is strongly based on the model by Lockhart and Martinelli [7] which gave the two-phase multiplier (φ) as:

$$\phi_L^2 = 1 + \frac{C}{X} + \frac{1}{X^2} \tag{2.1}$$

for liquid single-phase pressure drop and:

$$\phi_G^2 = 1 + CX + X^2 \tag{2.2}$$

for gas single-phase pressure drop, where X is given by:

$$X = \left(\frac{\mu_l}{\mu_g}\right)^{0.1} \left(\frac{\rho_g}{\rho_l}\right)^{0.5} \left(\frac{1-x}{x}\right)^{0.9} \tag{2.3}$$

Chisholm [8] later provided a basis for predicting C (the Chisholm parameter) based on the liquid and gas Reynold's numbers. This parameter has become the primary basis for furthering two-phase pressure drop correlations.

In 1996, Mishima and Hibiki [4] conducted experiments with 1 to 4 mm hydraulic diameter channels with both circular and rectangular cross-sections. Flow was forced in a vertical upwards direction through both glass and aluminum tubes. Over a wide range of superficial velocities, turbulent flow was observed in both the liquid and gaseous phases. It was noted that the hydraulic diameter affected the two-phase multiplier. The Chisholm parameter was then correlated to hydraulic diameter.

$$C^* = 21\left(1 - e^{-.319D_h}\right) \tag{2.4}$$

In 2006, English and Kandlikar [9] observed two-phase flow in horizontal channels while studying the effects of surfactants. Rectangular channels in Lexan with a hydraulic diameter of 1.018 mm were used. Over the range of superficial velocities studied, laminar flow conditions were observed. It was concluded that in laminar conditions the Chisholm parameter was similarly correlated hydraulic

diameter. The correlation by Mishima and Hibiki [4] was modified to include the constant for laminar-laminar flow.

$$C^* = 5\left(1 - e^{-.319D_h}\right) \tag{2.5}$$

In 2001, Lee and Lee [10] conducted experiments varying aspect ratio with channels of hydraulic diameter from 0.78 to 6.67 mm. The width of the channel was held constant at 20 mm while the height of the channel was varied. The effect of aspect ratio, as well as the effect of hydraulic diameter, was highlighted and a further correlation was proposed. They proposed a Chisholm parameter as a function of three non-dimensional parameters which describe the fluid properties of the liquid phase.

$$C^* = A * Re_L^r * \lambda^q * \psi^b \tag{2.6}$$

where

$$Re_{Lo} = \frac{\rho_L U_L D_h}{\mu_L}; \quad \lambda = \frac{\mu_L^2}{\rho_L \sigma D_h}; \quad \psi = \frac{\mu_L (U_G + U_L)}{\sigma} \tag{2.7}$$

In 2010, Saisorn and Wongwises [11] provided an additional data set using three circular tubes varying in hydraulic diameter made of fused silica. In order to fit data, Lee and Lee's model used and provided alternative constants and exponents.

$$C^* = 7.599x10^{-3} * \lambda^{-0.631} * \varphi^{0.005} * Re_{Lo}^{-0.008} \tag{2.8}$$

In 2009, Sun and Mishima [13] reviewed prediction methods for two-phase pressure drop in microchannels. Eighteen papers were reviewed, and 2092 data points from all of the studies were compared against popular correlations. While many of the correlations work well specific regions, the general trend of data strongly indicated that changes in pressure drop strongly relate to the change in quality. A modified version of the Chisholm correlation was proposed which incorporates the effect of quality.

$$\phi_L^2 = 1 + \frac{C}{X^{1.19}} + \frac{1}{X^2} \tag{2.9}$$

$$C = 1.79 \frac{Re_g^{0.4}}{Re_l} \frac{1-x^{0.5}}{x} \tag{2.10}$$

In 2012, Grimm et al. [16] utilized a test section that provided continuous water introduction in lieu of simultaneous introduction at the entrance. The study provided modifications to English and Kandlikar [9] model to incorporate mass quality, as well as a three part flow regime separated model based on Lee and Lee's [10] work. For the flow regime separated model, Grimm et al. provided transition criteria from slug to film and film to mist. For the transition from slug to film flow, the ratio between gas inertial force and surface tension are compared.

$$\frac{\mathrm{Re_G}}{\mathrm{Re_L}} = \mathrm{We_L^{-1}} \tag{2.11}$$

For the transition from film to mist the ratio between viscous and inertial forces is compared.

$$\left[\frac{\mathrm{Re_G}}{\mathrm{Re_L}}\right]^{-1} = \frac{\mu_G U_G}{\sigma} \tag{2.12}$$

For the slug flow regime the Chisholm parameter was given by:

$$C = 0.772 Re_L^{0.051} \lambda^{0.016} \psi^{-1.716} X^{0.034} \tag{2.13}$$

For the film flow regime the Chisholm parameter was given by:

$$C = 1.9087 Re_L^{-0.405} \lambda^{-0.134} \psi^{-0.421} \chi^{-0.107} \tag{2.14}$$

where

$$\chi = \frac{1-x}{x} \tag{2.15}$$

Two-phase pressure drop was given by a traditional homogeneuos model where two-phase properties are given by the correlation proposed by Dukler [6], as shown.

$$\Delta P = \frac{2PoG}{\rho_{tp}\mu_{tp}D_h^2} \tag{2.16}$$

Grimm et al. [16] also provide a single model based on the update of the English and Kandlikar [9] model which incorporates the changing mass quality into the modified Chisholm parameter.

$$C = A\left(\frac{1-x}{x}\right)^b \tag{2.17}$$

where

$$A = 0.0856(u_L)^{-1.202}\ ; \quad b = 0.004(u_L)^{-0.526} \tag{2.18}$$

These notable studies and their contributions are summarized in Table 1, each of which updated the correlation for the Chisholm parameter.

Table 2 - Relevant Two-Phase Pressure Drop Investigations

Investigator	Hydraulic Diameter	Orientation / Cross-section	Superficial Velocity Range	Key Conditions / Findings
Mishima and Hibiki (1996)	1-4 mm	Vertical Upwards	$0.0896 < j_g < 79.3$ m/s $0.0116 < j_l < 1.67$ m/s	Observed turbulent flow Correlated C to D_h
Lee and Lee (2001)	0.78, 1.90, 3.64, 6.67 mm	Horizontal / Width constant at 20 mm	$0.03 < j_g < 18.7$ m/s $0.05 < j_l < 2.66$ m/s	Correlated C to a function of ψ, λ, and Re
English and Kandlikar (2006)	1.018 mm	Horizontal / 1.124 x 0.930 mm	$3.19 < j_g < 10.06$ m/s $0.0005 < j_l < 0.0217$ m/s	Observed laminar flow Investigated surfactants Correlated C to D_h
Sun and Mishima (2009)	0.506 to 12 mm	Data from 18 studies and 2092 data points, covering 11 working fluids		Well reviewed previous methods, identified quality as key variable
Saisorn and Wongwises (2010)	0.15, 0.22, 0.53 mm	Horizontal / Circular	$0.37 < j_g < 42.36$ m/s $0.005 < j_l < 3.04$ m/s	Used model proposed by Lee and Lee
Grimm *et al.* (2012)	0.51 mm	Vertical / 0.4 x 0.7 mm	$0.5 < j_g < 29.5$ m/s $1.5 \cdot 10^{-4} < j_l < 1.5 \cdot 10^{-3}$ m/s	Incorporated continuous water introduction

2.1.2. Applicability to PEMFC Conditions

While most work in two-phase pressure drop focuses primarily on simultaneous air and water introduction at the inlet of the channel, this is not representative of PEMFC gas channels. Continuous water introduction from the reaction through the gas diffusion layer and condensation of water vapor from the flow stream play a primary role in a changing quality along the channel. The continuous water introduction creates a variable liquid mass flow rate, which creates the potential for flow regime changes along the channel. Furthermore, mass consumption of reactant gases is neglected in

all the previous studies reported in Table 1. The consumption of species along the channel creates a variable reactant mass flow rate, which further causes changes in local flow patterns.

The consumption of species along the channel has been studied using segmented PEMFCs. The first notable investigation which directly studied molar concentrations along the channel was by Mench et al. [17] in which measure molar fraction of H_2O and reactants along the length of a serpentine flow channel. This work focused primarily on the functional relationship between molar concentration of reactants and the water distribution in operating PEMFC. The measurements were taken via gas chromatograph with discrete measurements every 2 minutes. Anode water distribution was found to not be greatly influence by current density, while the cathode water uptake showed some dependence on current density.

At the typical operating temperature (80°C), with thermal equilibrium and an inlet relative humidity as high as 75%, the reactants on the cathode side can still carry nearly all product water in gaseous form. This relationship between inlet temperature, inlet relative humidity, and the percentage of the product water that can theoretically be removed is shown in Figure 8. The assumption of thermal equilibrium can be relaxed to capture the effect of air flow rate on local relative humidity in each element through further investigation.

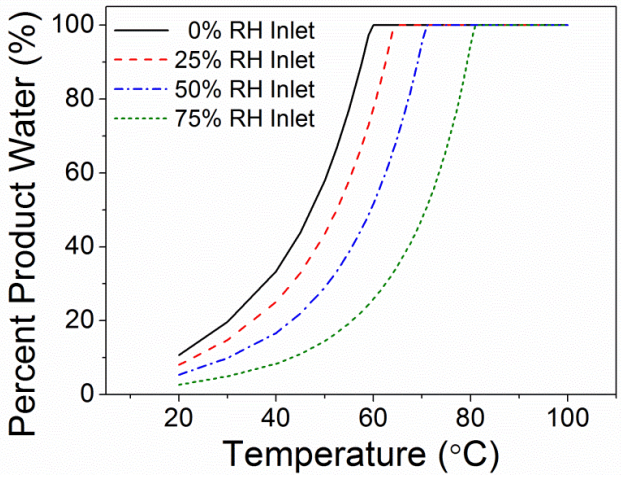

Figure 8 - Comparison of cathode reactant stream's ability to remove product water at a stoichiometry of 2.

This concept for gas sampling along a segmented PEMFC was later extended by Yang et al. [18] to study reactant concentrations in low humidity conditions. This investigation focused on measuring species and current distributions similar to those reviewed by Wang [19], while maintaining the performance expected of a non-segmented PEMFC. They achieved local current densities as high as 1.4 A/cm^2, while sampling local species and current profiles. The study focused around low humidity cathode inlet gases (25% and 50% RH) and 80°C operation. In these conditions, it was seen that the cathode O_2 concentration profile was generally linear and could be very well predicted by a simple mass balance approach. Similar trends were seen with the H_2 profile with measurements matching mass balance predictions.

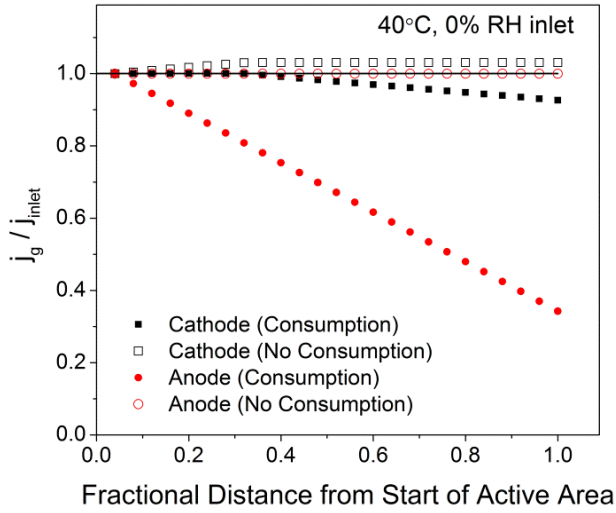

Figure 9 - Comparison of superficial gas velocity along reactant channel.

Consumption of reactants has been assumed to be negligible by many studies including [2,20]. Due to the combined fact that O_2 comprises only 21% of the cathode reactant stream at the inlet and a stoichiometric ratio of 2 or higher is generally employed, the mass consumption on the cathode side is typically ignored. This introduces an error of approximately 10% in pressure drop prediction. It is important to note that stoichiometry plays a crucial role in the effect of consumption. As the stoichiometric ratio approaches 1 the change in superficial velocity in the reactant channel increases significantly. On the anode side, neglecting consumption induces significant error and does not

properly predict the non-linear pressure drop on the anode side. The magnitude of this discrepancy is shown in Figure 9, with superficial reactant velocities normalized by the inlet velocity.

Through studies incorporating segmented PEMFCs, the need for a spatially resolved modeling approach has been illustrated. Lu et al. [21] extended the work of these previous studies through the use of straight channel PEMFC and a spatially resolved modeling approach. Notably, the experimental PEMFC in this study was 6 cm^2 active area as compared to 50 cm^2 for Wang [19] and Yang [18]. However, Lu et al. introduced a material balance analysis around 10 discrete differential volumes within the PEMFC. This differential volume was evaluated under steady state operation to predict net water transport across the membrane. Using this approach, net water drag coefficients were reported as a function of distance along the channel, in lieu of a bulk coefficient. This modeling approach can be easily mapped to other areas of interest within PEMFC channel two-phase studies.

In many of these studies, channel dimensions are not representative of typical PEMFC reactant channels. The hydraulic diameter of a typical PEMFC reactant channel is on the order of 500 μm, while most studies have hydraulic diameters of greater than 1 mm. The cross-section of the PEMFC reactant channels is typically rectangular or trapezoidal with a narrow range of aspect ratios, while typical studies are often circular and include aspect ratios well outside the range for use in PEMFC.

It has been shown in several studies [11, 12, 22, 23] that the material and consequently surface energy of the flow channel affects flow pattern transitions. Typical materials that have been used in PEMFC reactant channels are stainless steel, graphite, and gold plating. However, most two-phase pressure drop studies used alternative materials; Grimm et al. [16], English and Kandlikar [9], and Lee and Lee [10] all used Lexan channels, while Saisorn and Wongwises [11] used fused silica tubes, and Mishima and Hibiki [4] used both glass and aluminum. The variance in contact and (and consequently surface energy) is shown in Table 3.

Table 3 – Wettability of Common PEMFC Materials

Material	Static Contact Angle	Advancing Contact Angle	Receding Contact Angle
Aluminum	61°	75°	48°
Copper (Machined Surface)	76°	91°	47°
Copper (Polished)	79°	98°	47°
Copper (Gold Plated)	63°	79°	42°
Graphite (GM)	98°	105°	63°
Graphite (Los Alamos)	93°	95°	75°
Stainless Steel	59°	69°	44°
Lexan	86°	95°	61°
MRC-105 GDL (Carbon Paper)	148°	148°	138°

A final key parameter that has not been well investigated in two-phase pressure drop in microchannels is elevated temperatures. It is well known that PEMFCs typically have improved performance at 80°C. However, all of the most prominent two-phase pressure drop studies have been conducted at room temperature [4–11].

2.1.3. Multichannel Effects within PEMFCs

Single channel experimentation as a simplified method to mimic parallel channel arrangements implicitly implies that channels will experience uniform flow distribution. However, flow maldistribution can be inherently caused by many factors. In 2009, Kandlikar et al. [24] identified two main causes of maldistribution in parallel channels:

1) Manifold design and local pressure distribution across inlet/exit
2) Uneven flow resistance (due to changes in channel geometry, flow length, and fluid properties or presence of two-phase flow)

Kandlikar et al. [24] proposed a technique for experimental measurement of flow maldistribution in each of parallel channels to quantify flow maldistribution through minimally invasive measurement. Through the use of the non-linear pressure drop within the entrance region, the Hornbeck Equation was used to correlate flow rate to pressure drop. Pressure taps were located within entrance region of each channel, and known flow rates were supplied to create individual calibrations. This method was then tested using 4 circular stainless steel tubes of various lengths. The measured flow rates averaged an error of 3.3% when validated against established theoretical predictions. This methodology presented by Kandlikar et al. [24] has been extended to use with ex situ and in situ PEMFC flow channel studies [16,25–27] as well as flow distributor design.

In order to study multichannel effects on water management in 2009, Owejan et al. [16] designed a standardized geometry 50 cm^2 fuel cell design that could meet the needs for in situ and ex situ experimentation. In order to ensure the robustness of the studies, the design was specified in accordance with the United States Department of Energy (USDOE) performance targets.

A channel width of 0.7 mm was selected for both anode and cathode sides. A land width of 0.5 mm was selected for the cathode in order to obtain a land-to channel ratio of 1.4. However, the anode land width was selected to be 1.5 mm for three reasons. Firstly, reducing channels would increase the hydrogen volumetric flow rate in each channel. Secondly, it would increase the contact area greatly reducing ohmic losses. Finally, it would minimize any pinching effect between cathode and anode channels. A channel depth of 0.4 mm was selected to allow for a reasonable repeat distance to meet USDOE energy density targets. A channel length (183 mm) was back calculated from peak power density prediction. The channels were arranged as parallel straight channels, with a 15 switchback to prevent shearing of the GDL or MEA. This design has provided insight into water management through in situ studies [24,28], ex situ studies [25,26,29], as well as direct visualization [28] and neutron radiography [16].

The flow maldistribution seen by Kandlikar et al. [24] led to an investigation into how the GDL compresses under channels and lands of a flow field. In a following study, Kandlikar et al. [27]

investigated GDL intrusion into the gas channel and its effect on flow. A flow field made of Lexan® with the channel geometry suggested by Owejan et al. [16] was developed for visualization from two sides of the channel to measure intrusion. A confocal digital microscope (Keyence VHX-500) was used to optically image the cross-section of the channel, as well as create 3-D scans of the GDL perpendicular to the flow direction. Additionally, flow rate measurement was used to quantify the intrusion's effect on flow within the channel. The intrusion was measured at compressions ranging from 1.03 MPa to 10.34 MPa. A minimum intrusion of 0.2 μm was observed, while a maximum of 111.0 μm was observed at the highest compressive pressure. At typical operating ranges an intrusion of 30 – 70 μm was observed, which can significantly constrict the flow channel. Significant variance in intrusion between channels was also seen to create significant flow maldistribution.

In order to investigate the combined result of the multichannel effects, Lu et al. [25] developed an ex situ PEMFC test section made of Lexan® with a set of 8 parallel channels, 4 water introduction chambers, and 12 water inlet holes representing active area. The apparatus allowed for the measurement of individual channel flow rates, pressure drop, and direct optical visualization of the flow field. The flow conditions were tested over range of stoichiometric ratios from 1 to 50 for equivalent current densities from 0 to 2.0 A/cm^2. A significant amount of water holdup was noted at the outlet manifold. One phenomenon which was observed was sharp spikes in the airflow rate of an individual channel. These spikes were seen to be caused by the water removal at the channel outlet. Additionally, it was found that slug residence time in the channel generally decreased with superficial air velocity. At a superficial air velocity of 4 m/s the residence time no longer decreases and above 7.4 m/s the flow maldistribution and slug flow significantly reduces. Using pressure drop from various flow conditions, Lu et al. [25] identified pressure drop signatures indicative of slug, film and mist flow.

In 2011, Lu et al. [25] investigated the effect of surface wettability, channel geometry, and orientation. Three surfaces with different wettability were tested including a baseline (85°), hydrophobic (116°), and hydrophilic coating (11°). The hydrophilic coating was observed to provide

a more uniform water distribution with less maldistribution, while hydrophobic and baseline channels acted very comparable to one another. Channel geometry was varied from a rectangular shape (meant to represent laboratory studies), to sinusoidal geometry (meant to represent stamped plates), to trapezoidal (meant to represent molded plates) while the hydraulic diameter was held similar to allow for comparison. The sinusoidal channels showed a predilection to forming film flow due to its small angle with the GDL surface. Both the rectangular and trapezoidal acted comparably, and formed slugs more regularly than the sinusoidal channels.

2.2. Local Water Saturation

In 2009, Dai et al. [30] provided an excellent review of water balance and major transport mechanisms in PEMFC. Each of the major transport mechanisms (electro-osmotic drag, back diffusion, pressure driven hydraulic permeation, and thermal-osmotic drag) and their previously published values were reviewed. Electro-osmotic drag obtained by many researchers was compared, and significant variance was seen within Nafion 117 above the room temperature. Dai et al. [30] highlighted the importance of the net water drag coefficient due to the complexities of independently measuring each mechanism. The net water drag coefficient is defined as net number of water molecules transported across the membrane per proton conducted.

One of the most notable investigations into water transport across the PEMFC membrane was performed by Atiyeh et al. [31] in 2007. A highly reliable system for measuring overall water balance was developed and tested on a 100 cm^2 PEMFC, exceeding overall accuracy from the previous studies. Tests were conducted using a Hydrogenics FCATS-S800 test stand, which was evaluated for accuracy. The standard humidification loop was found to be inadequate for water balance studies, often reporting dew point of the reactant gas stream off by 3-8 °C. In order to achieve meaningful net drag coefficients, modifications to the humidifier's dew point sensing and water collection system were made. Condensers with water knockouts were added to ensure complete water collection on the outlet of the water balance system. An accuracy within 5% for overall water balance was achieved; however it required an average of 23 hours of water collection.

Similarly in 2012, Kuhn el at. [32] performed the validation of a dynamic humidification system for water balance experiments. The importance of accurate knowledge of water content at the reactant inlet was emphasized. Three primary methods of reactant humidification are reviewed, gas-gas membrane, direct water injection, and saturation bubbler. Saturation bubbler based humidification is proposed as the most desirable choice; however accuracy is seen to be lower than desired. The system

was validated using a dew point mirror, which resulted in 1-3 °K variation, which at high flow rates can result in significant fluctuations in water content at the inlet.

While most water balance studies focus on transport across the membrane, quantification of water within the reactant channels is critical for the understanding of two-phase flow within a PEMFC. Sergi and Kandlikar [28] investigated a direct visualization method to quantify water in PEMFC reactant channels using image processing. A 50 cm^2 PEMFC was used that matched design parameters from previous studies [16]. Two high speed cameras with full megapixel resolution (1024 x 1024) were used to visualize inside the transparent PEMFC's reactant channels. Through morphological processing, water was quantified in the form of a new parameter, water coverage ratio. Additionally, flow regime detection was included in the study allowing for differentiation of flow regimes based on operating parameters. Similar test hardware was used in neutron radiography studies by Owejan et al. [16] for purge analysis. Most notably, neutron radiography imaging does not differentiate water in the reactant channel and water in the GDL, thus requiring additional post-processing for pressure drop applications.

2.3. Summary of Research Needs

It can be seen from the literature that there is a lack of a comprehensive methodology and correlation for predicting two-phase pressure drop within PEM fuel cell reactant channels. A methodology needs to be developed to fully incorporate these key considerations and operating parameters. It will also provide a valuable tool for the design and optimization of PEM fuel cells. The aforementioned key differences from adiabatic two-phase literature that have previously been neglected in PEMFC reactant channel two-phase pressure drop modeling can be applied to two-phase pressure drop in order to improve accuracy. These unique conditions merit a step-wise modeling approach to predict local water saturation, flow patterns, and pressure drop. Additionally, a large dataset over a targeted range of conditions must be developed for these conditions to validate and develop the complex sub-components of the modeling.

2.4. Scope of Work

The goal of this work is to create a comprehensive basis for understanding two-phase transport and pressure drop with PEM fuel cell reactant channels. The following objectives have been established to meet key research needs and to contribute to the PEMFC and two-phase flow research community:

Objective #1

- Develop two small scale PEM fuel cells which represent actual automotive geometry using both traditional and optically transparent materials

Objective #2

- Generate a large database of pressure drop, performance, and visual data targeted at low operating temperature and current density

Objective #3

- Development of a 1+1D PEMFC gas channel two-phase pressure drop model
  - Expansion of an elemental modeling technique for two-phase flows for two-phase pressure drop analysis
  - Provide methodology for characterization and prediction of local water saturation in PEMFC gas channels

3. Experimental Methodology

In this work, a fuel cell test facility for PEM fuel cell performance testing and two fuel cell designs are utilized. Modifications are made to the existing facility to allow the extensive data collection and increased testing time needed for this work. The primary objective of the experimental PEM fuel cell designs is to simulate commercial stack performance through the use of a visualization cell and a baseline cell. The influence of key components and operating parameters on performance and two-phase flow within the cell is investigated. The 50 cm^2 PEM fuel cells are developed to represent scaled current industry design and performance targets [33]. This allows for both traditional and visualization fuel cells, comprehensive temperature control, water collection, and automated testing protocols.

3.1. System Overview

The PEMFC is tested using a Greenlight Innovation G40 Fuel Cell Test Stand operated under constant current control from a TDI Load Bank. The air is supplied via a Parker Balston Zero Air Generator, while hydrogen and nitrogen are supplied from ultra-high purity grade compressed gas cylinders. The G40 test stand includes an integrated humidification system providing humidification via mist injection and optional dry gas bypass system. The water for used for the humidification system is supplied on-demand from a custom Siemens water de-ionization system. To provide back pressure, Fairchild T6000 electro-pneumatic E/P Transducers were used in conjunction with Go Regulator Inc. BP-Series Pneumatic Back Pressure Regulators. Control for test stand systems is provided through HYWARE II testing software on a Dell Optiplex 790, while auxiliary systems, visualization, and data acquisition systems are controlled and monitored through an HP Z800 Workstation.

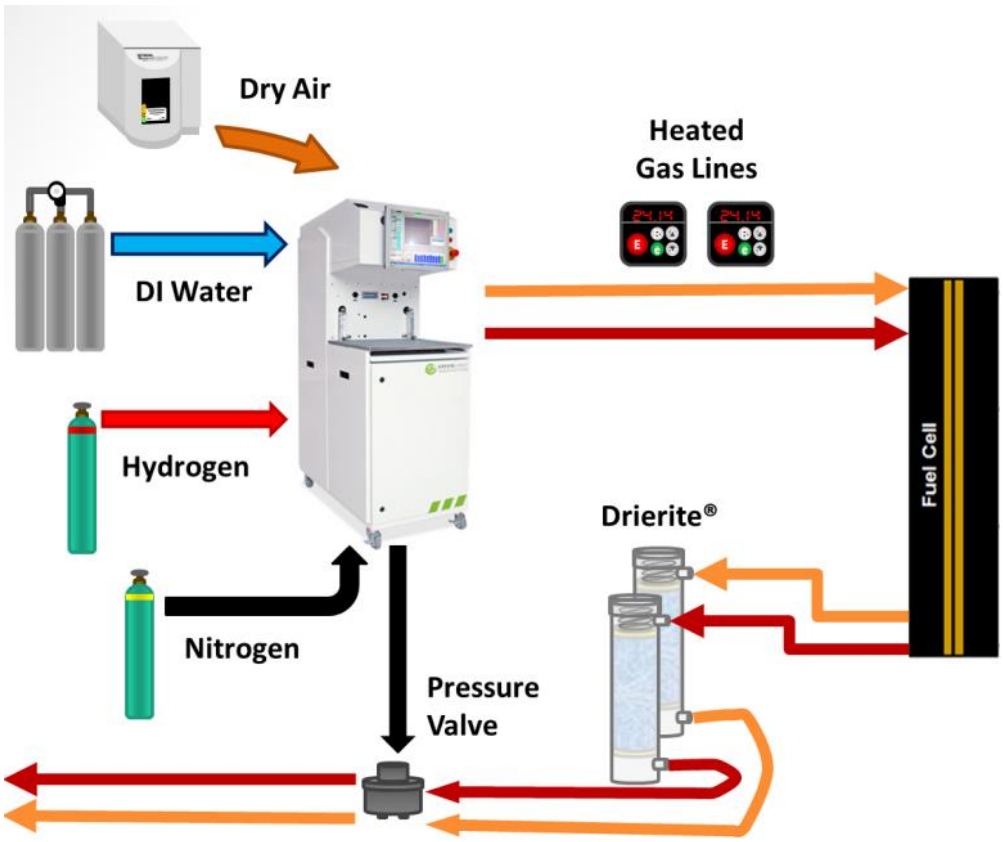

Figure 10 – Schematic of PEM Fuel Cell Testing Facility

Reactant gases are supplied via ¼ inch 316 stainless steel tubing through an in-house developed heated gas line system. The stainless steel lines are coated with Kapton polyamide film to prevent electrical discharge to reactants and minimize static accumulation. Each reactant line is heated via an Omega 120V rope heater through the use of 30VDC switch solid state relays and insulated using braided fiberglass insulation. Control for heating is provided through a Watlow EZ-Zone Integrated PID Limit Controller with full auto-tuned PID output with K-type thermocouple feedback loop. Limit control is monitored through the Watlow EZ-Zone system via K-type thermocouples inside the insulation connected to a non-sparking mechanical relay which disconnects all power in limit situations. The thermal management systems are shown in Figure 11.

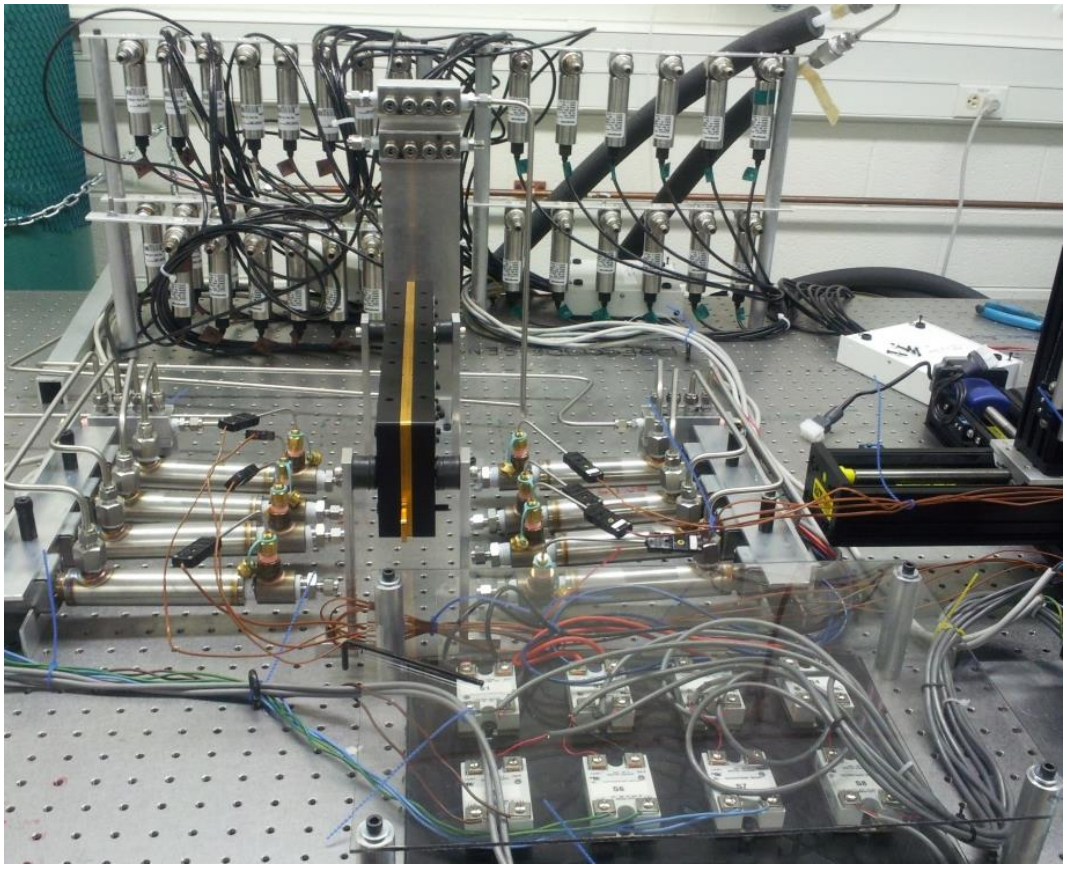

Figure 11 – Thermal Management System

A comprehensive thermal management system has been developed in order to effectively control and monitor operating conditions. Two Thermo Scientific ARCTIC model EW-12127-20 refrigerated circulating baths with SC-150 controllers provide a stable coolant temperature, with circulation provided by a 1/3 HP three phase electric motor attached to a Micropump®. Control and monitoring is performed through the RS-232 interface with control software programmed in LabVIEW. The operating temperatures range from -25 to 150°C for coolant circulation. In the current work, distilled water is being utilized as a coolant, while glycol can be utilized in this configuration to decrease temperature below 10°C if needed in revised testing. Eight Omega AHPF-061 in-line heaters are utilized to provide discrete temperature control to each of the eight integrated coolant loops within the experimental PEMFC. Each heater can provide up to a 15°C temperature increase from the constant

temperature circulating bath. All eight coolant loops are controlled using auto-tuning PID loops through two Omega CN1504TC multi-zone controllers, eight Omega SSRL240DC25 Solid State Relays, and integral J-type thermocouple feedback loops. Fuel cell temperature is monitored via twelve K-type thermocouples integrated into the compression plates; one for each of the coolant loops. Additionally, coolant temperature is monitored at the outlet of each integrated coolant loop.

The experimental PEMFC is dual vibration isolated with a Newport SMART Table UT2 and rubber isolation mounts with a 50A durometer. The manifold-to-manifold anode and cathode pressure drop are measured with Honeywell FDW differential pressure transducers with a range of 0-5 psi. Thirty three Honeywell 060-G763-07 pressure sensors are used to acquire individual channel pressure drops in the entrance region to obtain individual channel flow rates, as demonstrated by Kandlikar et al. [24].

3.2. PEM Fuel Cell Design

3.2.1. Baseline Fuel Cell Design

Flow field design features, such as aspect ratio and channel geometry, are applied from a previous DOE funded water management investigation [16]. These design features are summarized in **Table 4**.

Table 4 – Summary of PEMFC Channel Dimensions

	Reactant Channel	Coolant Channel
Channel Depth	0.4 mm	1 mm
Channel Width	0.7 mm	1 mm
Channel Length	233 mm	43 mm/pass 11 passes
Channel Geometry	Rectangular	Square
Flow Field Geometry	Straight*	Serpentine
Number of Channels	11 Anode Side 22 Cathode Side	4

* 11° switchback every 5 cm to prevent mechanical shearing

The incorporation of an adaptable cooling system with a water collection system allows detailed insight into how operating parameters affect down the channel transport resistances. Additionally, the use of integrated micro-thermocouples within the unipolar plates (UPPs) allows for the characterization of localized temperature profiles. An expanded view of the PEMFC assembly is shown in Figure 4.

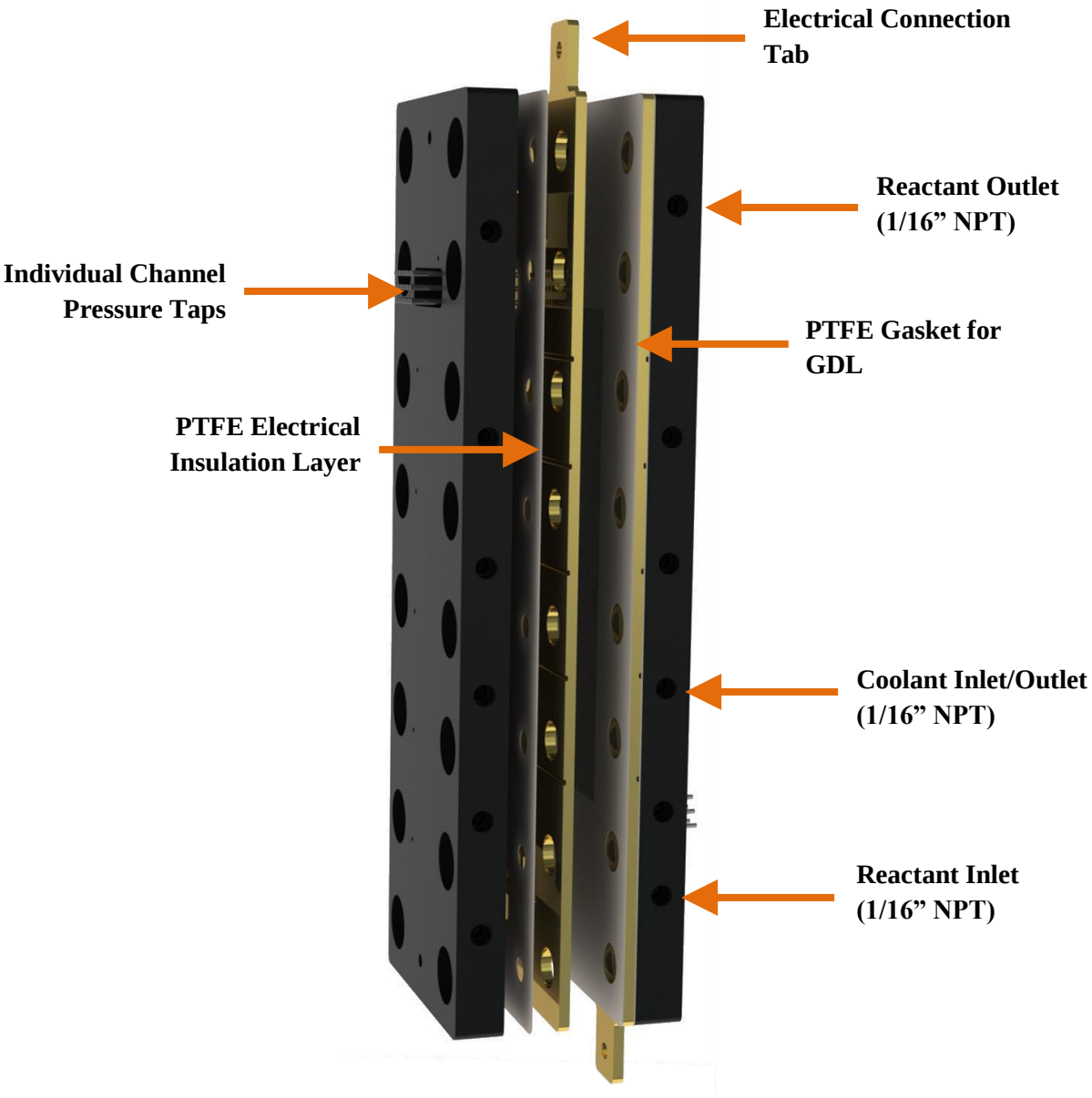

Figure 12 - Baseline Cell Assembly View

In order to provide precise thermal control, two design iterations of coolant channels are being utilized. The original design, which provides the ability for the smoothest temperature gradients, consists of 4 serpentine coolant channels were machined into the compression plate. Each section allows for independent control, allowing up to 20°C in variation between cooling circuits via in line electric heaters regulated with PID controls. This allows for the application of temperature profiles from PEMFC stack measurements; allowing it to simulate any location within a fuel cell stack. For the majority of testing, isothermal compression blocks are desired; consequently a secondary design with 10 larger straight coolant passages was implemented for more uniform cooling. The passages can be configured for isothermal operation, localized hot zones, or with a temperature gradient.

Commercially available FC stacks often use composite graphite bipolar plates due to the low electrical contact resistance they offer. Coatings of gold and titanium nitride are used to decrease the contact resistance for other plate materials, but are prohibitively expensive for mass production [34]. Although composite graphite is the preferred material, it could not be used due to its low flexural strength, which causes it to be highly susceptible to fracture in the 400 micrometer thick lands. Due to thickness constraints of the channels, the experimental UPP must be considerably thicker than commercial hardware. In order to offset the change in thickness, the thermal conductivity of the experimental UPP must be higher than that of composite graphite. Copper provides adequate thermal conductivity, while also providing sufficient flexural strength. In order to prevent corrosion of the UPP and maintain low electrical contact resistance, gold plating was applied to the copper.

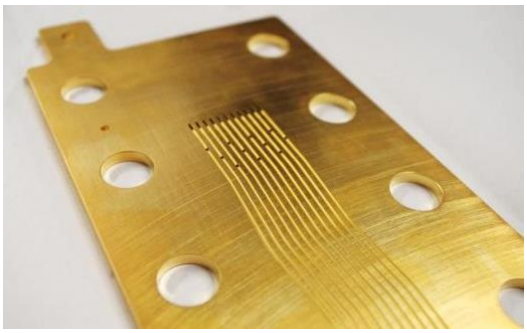

Figure 13 – Baseline Fuel Cell Flow Field

3.2.2. Visualization Fuel Cell

In order to complement the baseline fuel cell and provide direct visual access to the local two-phase flow conditions, a 50 cm^2 optically transparent fuel cell was developed. The flow field design and overall dimensions of the active area were identical to that of the baseline cell. The flow fields were 400 µm gold-plated copper plates which were cut via wire EDM (electrical discharge machining). The gold-plated copper flow fields form two of the channel walls within the visualization cell, while the GDL forms the third wall. The fourth wall is created by an optically transparent sheet of Lexan® which also provides mechanical support. Two machined 6061 aluminum blocks provided compression as well an inlets and outlets for reactants. The lack of coolant passages necessitated heaters to be placed on the aluminum compression blocks to heat the fuel cell during operation. At higher current densities, the heaters are disconnected and heat output from the reaction is used to maintain the cell temperature. In order to monitor the temperature of the MEA, four thin film thermocouples were placed on the edge of the active area on both anode and cathode at the inlet and outlet.

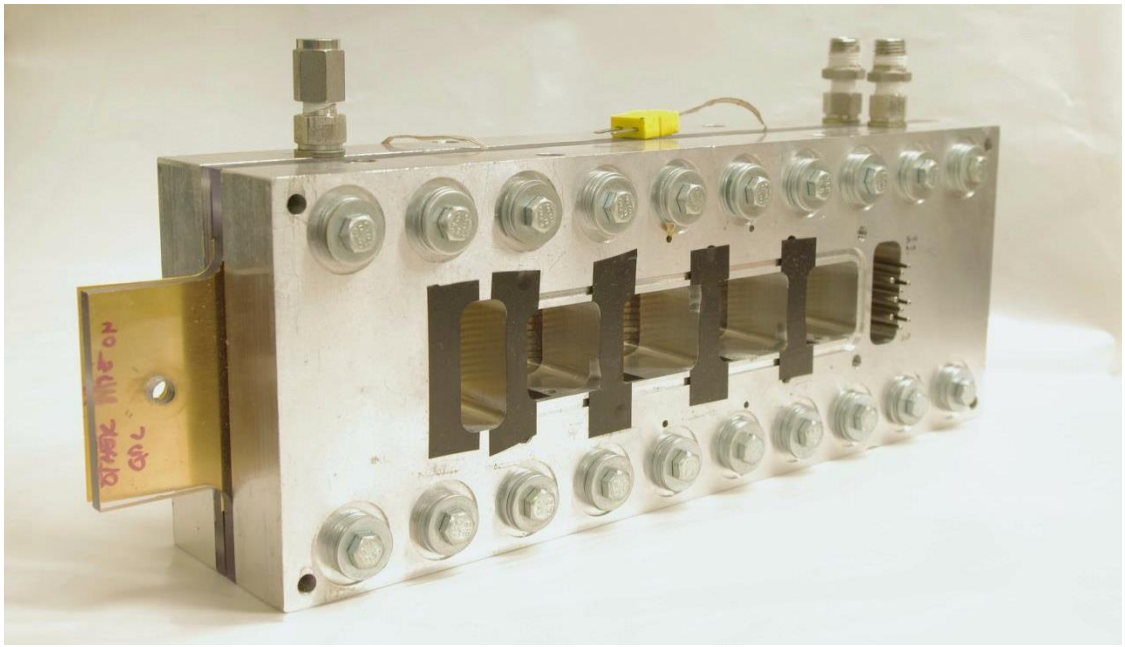

Figure 14 – Assembled Visualization PEM Fuel Cell

3.3. Water Balance System Design

In order to quantify the mass of water exiting the cathode and anode sides of the experimental PEMFC, a water balance measurement system was developed. The system consists of dewpoint sensors at the reactant inlets, desiccant water collection, and outlet relative humidity sensors.

To accurately monitor the mass of water entering the fuel cell, dewpoint sensors are located inside of the reactant humidification system. Initial testing showed inaccuracy in water mass prediction based on humidification water temperature. In order to minimize this error, thermocouples with a 150 µm tip were installed in the fully saturated reactant stream to provide a faster response to changing dewpoint.

A desiccant based water collection system was selected over a traditional condenser system due to several complexity and accuracy concerns. A primary concern was droplet pinning within the condenser system. A significant amount of water hold-up could occur in the tubing of the condenser system, causing inherent inaccuracy in the measurement. Most water collection to be performed is on the order of 10 g of water and as low as 0.5 g of water. The hold-up within a condenser system can be as high as 3 g, introducing significant error.

The selected desiccant system uses Drierite®, a gypsum (calcium sulfate) desiccant that can be regenerated and is not affected by the presence of hydrogen. The desiccant holds the collected water securely in the form of the hemihydrate of calcium sulfate altering the weight of the granules rather than the volume. Therefore, if the unit is weighed on a balance before and after testing, the exact mass of water that has been collected can be determined accurately. The Drierite® desiccant material is held in a commercially available laboratory gas drying unit (Drierite® Stock #26800). The liquid water is collected in the bottom of the unit, while vapor is collected by the desiccant. The gas drying unit is pictured below in Figure 6. The system is attached to the experimental PEMFC through self-

sealing quick disconnects. In order to ensure accurate timing of water collection and provide a bypass system, a solenoid valve system controlled by an Omega PTC-13 programmable timer was implemented.

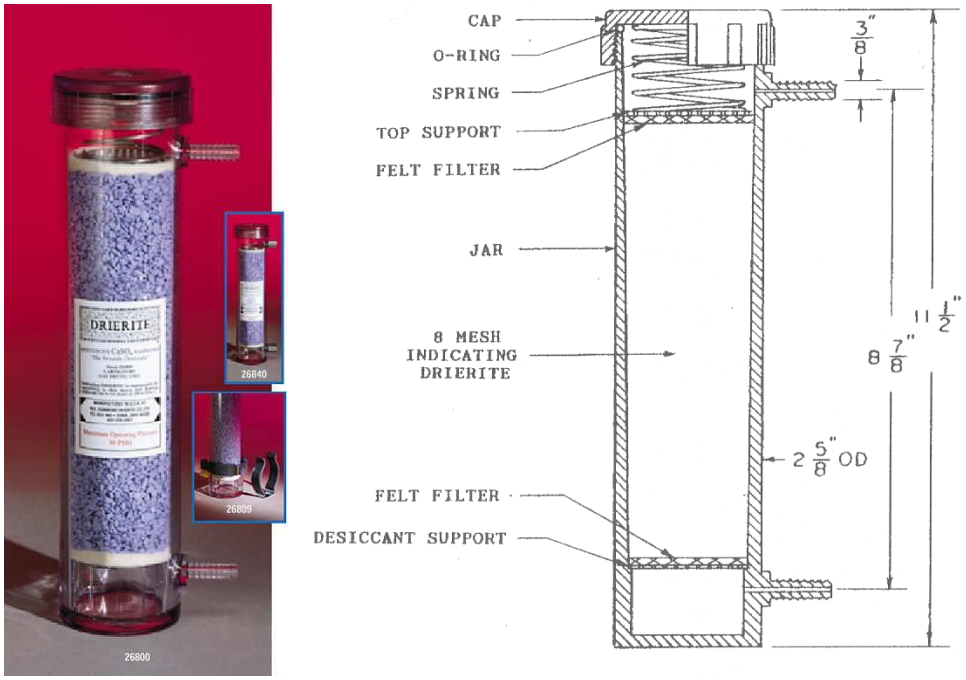

Figure 15 – Drierite® Laboratory Gas Drying Unit [35]

A Mettler Toledo® precision balance is used to accurately measure the weight of the desiccant before and after tests. The balance features a 1620 g capacity with 10 mg precision and is manually calibrated with ASTM Class 1 Calibration weights as well as automatically calibrated for temperature and humidity throughout the testing. The desiccant can be either replaced with new granules or dehydrated in an oven at 450 °F for two hours for reuse in later experiments. Because the unit requires a very high temperature to release the water unlike other desiccants, it ensures that the water collected will remain in the desiccant during testing cannot be accidentally released due to high temperature testing. In order to ensure that the desiccant system collects all water exiting the experimental PEMFC, relative humidity sensors are placed just after the desiccant.

3.4. Data Acquisition

A comprehensive data acquisition system (DAQ) has been developed in order to effectively record and integrate this data in to the modeling techniques. A National Instruments PXIe-1075 18 slot chassis is being utilized for a high-bandwidth backplane providing 4 GB/s of data logging, shown in Figure 16. Three PXIe-4353 have been selected to provide 96 thermocouple inputs logging a maximum of 8640 S/s. In order to obtain pressure and flow measurements, 64 single ended voltage channels have been added, with a maximum aggregate sampling rate of 4 MS/s. Additionally, all operating parameters are logged by an integrated DAQ in the Greenlight Innovations G40 test stand at 1 S/s.

Figure 16 - National Instruments PXIe-1075 Data Acquisition System

As described in Section 3.1, the PEM fuel cell control is provided through HYWARE II testing software on a Dell OptiPlex 790, while auxiliary systems, visualization, and data acquisition systems are controlled and monitored through an HP Z800 Workstation. A set of VIs (virtual instruments) were developed to monitor cooling systems, pressure drop, and data acquisition during testing as shown in Figure 17.

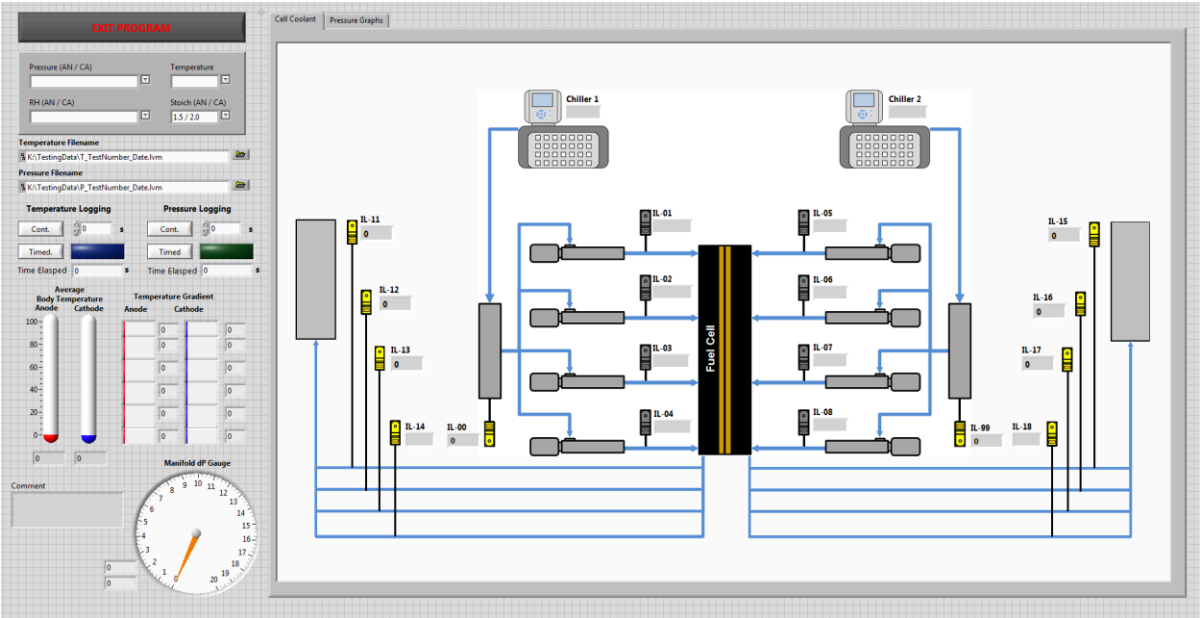

Figure 17 – LabVIEW VI used for Data Collection and Fuel Cell Monitoring

3.5. Tested Conditions and Cell Components

In order to generate a large database of fuel cell performance and pressure drop data, 198 tests were performed that varied six parameters. These parameters are summarized in Table 5. A complete list of tested conditions is presented in Section 9.

Table 5 – Range of Variables for Testing Database

GDL	Inlet Relative Humidity	Current Density (A/cm^2)*	Stoichiometry	Cell Temperature
MRC-105	0%	0.05	1.5 : 2.0	40
Freudenberg	95%	1.00	1.5 : 2.5	50
Toray 060			1.5 : 5.0	60
SGL 25 BC			3.0 : 8.0	

* Increments of 0.05 A/cm^2 up to 0.4 A/cm^2, Increments of 0.10 A/cm^2 up to 0.6 A/cm^2

In both PEM fuel cells, the membrane used was a W.L. Gore Inc. 18 μm perfluorosulfonic acid (PFSA) membrane. The anode catalyst layer had a target loading of 0.05 mg Pt/cm^2. The cathode catalyst layer had a target loading 0.3 mg Pt/cm^2. Four commercially available GDLs were tested in order to investigate its role in liquid water transport in the channel. All samples had a MPL coating, nominally 5 wt. % PTFE treatment, and approximate thickness of ~210 μm. The material; properties for all four GDLs are summarized in Table 6. Despite their similar material properties, there are significant differences in the structure of each GDL. The GDL samples used are shown in Figure 18 using confocal laser scanning microscopy. The fiber structure of MRC-105, SGL-25BC, and Toray 060 are very similar, all 2-D fiber orientation and typically straight fiber orientation. Freudenberg due to its air-laid hydro-entangled manufacturing process has significantly different fiber orientation with a truly 3-D orientation and curved fibers. Additionally, the binder which holds the fiber together varies between each GDL. The binder used in the SGL 25 BC sample is extremely coarse and does not span between fibers. On the other end of the spectrum, the binder used in the Toray 060 sample is smooth and spans fibers restricting the open area.

Table 6 – Summary of material properties of tested GDLs.

Property	Freudenberg H2315	MRC-105	Toray TGP-H-060	SGL 25BC
Type*	Air-laid hydro-entangled CFP	CFP	Wet-laid CFP	2D CFP
MPL Coating	Yes	Yes**	Yes	Yes
Thickness* (μm)	210	245	190	235
Contact Angle (°)	153	148	150	-
PTFE wt. %	5	5**	5	5

* As reported by manufacturer ** In-house by General Motors

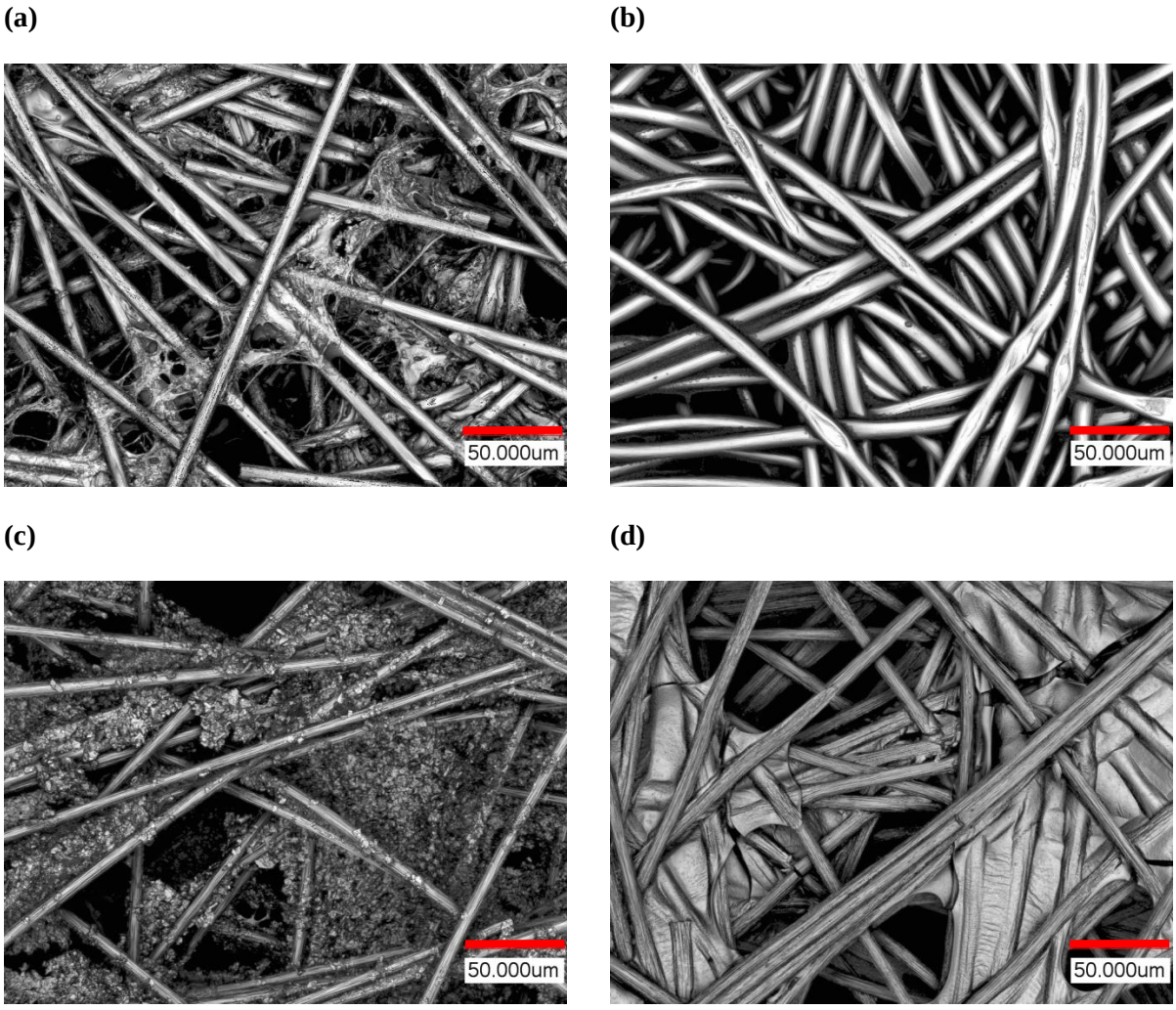

Figure 18 – Laser confocal images of tested GDLs

(a) MRC-105 (b) Freudenberg (c) SGL 25BC (d) Toray 060

3.6. Experimental Procedure

In order to ensure steady state measurement, testing followed a standardized protocol defined through previous studies and the steady state verification discussed in Section 5.4. Fuel cell conditioning was performed for a minimum of 8 hours after first assembly of the PEM fuel cell to ensure the membrane has been properly hydrated. At the beginning of each test run (typically a set of approximately 3-10 test conditions), the PEM fuel cell was conditioned for a minimum of 2 hours with fully humidified gases at 40 °C and operation at ~0.60 V. Constant current control was maintained and the load was

adjusted every 15 minutes to maintain ~0.60 V. At the beginning of each test run, the OCV was recorded and compared to previous test runs to ensure no performance degradation had occurred. If the test run was to consist of tests with a dry inlet stream, the G40 test stand was set to bypass the humidifiers and conditioned at ~0.6V for an additional hour before commencing the test run.

Once the PEM fuel cell was properly conditioned, tests covering the full range of variables summarized in Table 5 were performed. For the visualization cell the following procedure was followed during testing:

1) Current density was increased to next test condition.
2) Cell temperature, gas temperature, and humidifier dewpoint were set and allowed to reach steady operation.
3) Prior to data acquisition, the fuel cell operated for up to 60 minutes to reach steady state
4) Pressure drop data was recorded for 30 minutes at each of four windows
5) Simultaneously, video was recorded of the two-phase flow at each window. Flow regime observations were manually recorded for each window.
6) After data acquisition, the load and voltage were recorded via the G40 test stand.

After each test condition, the process was repeated until either the desired conditions were completed or the PEM fuel cell is unable to increase load without becoming unstable. Testing with the baseline PEM fuel cell was completed in the same manner, however pressure drop data was recorded for a continuous 90 minutes.

4. Two-Phase Pressure Drop Modeling

4.1. Model Development

Due to the unique conditions inside PEMFC gas channels, an exhaustive elemental modeling scheme is needed to provide accurate prediction of pressure drop within an operating PEMFC. Key factors, including mass consumption, temperature variation, local flow patterns, and the method of water introduction must be integrated into a modeling scheme utilizing traditional two-phase pressure drop correlations to increase the applicability to the PEMFC field.

The presence of variable flow rates along the channel of both reactants and product water merit a 1D analysis with element division along the flow length to evaluate the effects of local water saturation and flow pattern transition on pressure drop. The use of an elemental approach allows for the identification of flow pattern transitions along the channel length. These varied flow patterns have been shown to significantly affect local pressure drop [9–12,14]. For the proposed model, 14 elements are utilized to represent a typical PEMFC reactant channel, as presented in Figure 18.

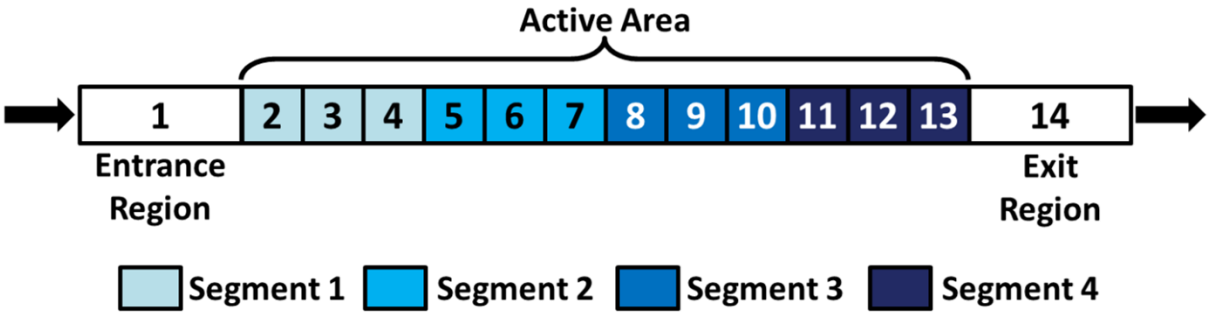

Figure 19 - Schematic of element division in the proposed PEM fuel cell pressure drop model.

The single-phase entrance region and the two-phase exit region are represented by elements 1 and 14 respectively. Elements 2 through 13 are distributed evenly along the active area of the fuel cell. These elements are grouped into four segments which correspond to key visualization areas in the experimental set-up.

At each element, a mass flow balance is applied on the control volume to determine the liquid water and reactant flow rates. The mass fluxes of reactants, liquid water, and water vapor are shown in Figure 9. In each control volume, liquid water and water vapor are treated separately in order to account for the effects of temperature and relative humidity on the reactant stream's fluid properties. At typical PEMFC operating temperatures, a significant portion of the product water can be transported as water vapor if the inlet stream is not fully humidified.

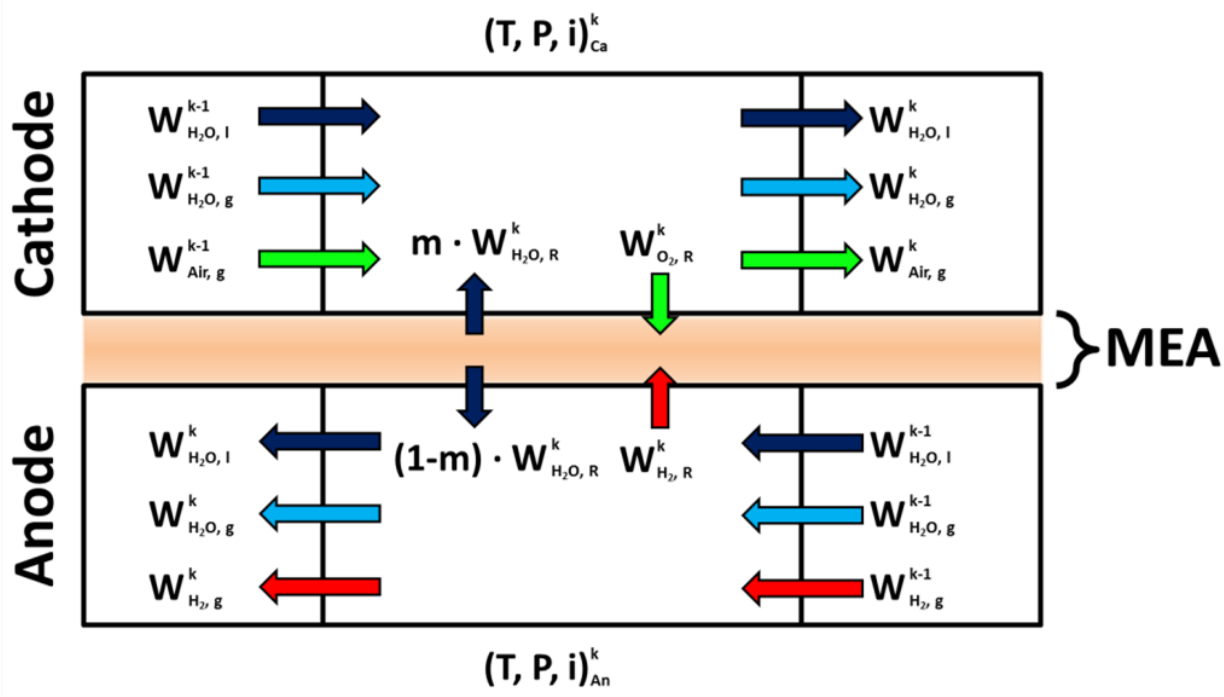

Figure 20 - Control volume for mass flow balance in a control volume.

An added feature in this model is the incorporation of mass consumption along the channel length. This has been assumed to be negligible by many studies including Grimm et al. [16]. Due to the combined fact that O_2 comprises only 21% of the cathode reactant stream at the inlet and a stoichiometric ratio of 2 or higher is generally employed, the mass consumption on the cathode is typically ignored. While this assumption holds reasonably well on the cathode side, it does not properly predict the non-linear pressure drop on the anode side.

When a dry reactant inlet stream is assumed, the mass flow of liquid product water into a dry reactant stream will cause an increase in the reactant stream's relative humidity based on evaporation rates. Conversely, mass consumption along the channel causes a reduction in the mass flow of water vapor that can be held within the stream causing condensation within the channel. This effect is accounted for using a limiting factor for evaporation based on local flow conditions. For this investigation, thermal equilibrium is assumed such that the limiting factor is 1.

One of the key factors to consider in PEMFC reactant channel's local conditions is the linkage between anode and cathode reactant channels. This linkage results in mass flux of water between anode and cathode due to electro-osmotic drag, thermo-osmosis, hydraulic permeation, and back diffusion, as well as the variable reduction of mass flow rate along the channel due to local reaction rates. Without expanding this model to include predictive cell performance, the effects of reaction rates are captured through the use of local current density. In order to encapsulate the effect of electro-osmotic drag and back diffusion, the net water transport is represented as m, the fraction of product water to the cathode.

4.2. Governing Equations

4.2.1. Minor Losses

While many previous studies offer idealized measurement of pressure drop, PEMFC research requires multichannel measurement and accounting for minor losses in the manifold. This yields an overall pressure drop given by:

$$\Delta P_{tot} = \Delta P_{in} + \Delta P_c + \Delta P_{er} + \sum_{k=a}^{b}\left(\Delta P_{E,k}\right) + \Delta P_e + \Delta P_{ex} \tag{4.1}$$

where ΔP_{tot} is the total pressure drop in the PEMFC, ΔP_{in} is entrance region effects, ΔP_c the contraction effects entering the channel, ΔP_{er} is the entrance region, $\Delta P_{E,k}$ is the pressure drop at each

element k over the active area, ΔP_e is the expansion effects, and ΔP_{ex} is the pressure drop in the exit region. The pressure drop due to entrance region effects is:

$$\Delta P_{in} = \left.\frac{K_{in}\rho_g U_g^2}{2}\right|_{k=0} \tag{4.2}$$

where U_g is the superficial velocity of reactant, ρ_g is the density of the reactant, and K_{in} is the entrance effects constant. The entrance effects constant is a function of channel dimensions and can calculated by:

$$K_{in} = 0.6796 + 1.2197\alpha + 3.3089\alpha^2 - 9.592\alpha^3 + 8.9089\alpha^4 - 2.9959\alpha^5 \tag{4.3}$$

where α is the aspect ratio of the channel cross-section. The contraction and expansion effects entering the channels, respectively, are given by:

$$\Delta P_c = \left.\frac{N_c K_c \rho_g U_g^2}{2}\right|_{k=0} \tag{4.4}$$

$$\Delta P_e = \left.\frac{N_c K_e \rho_g U_g^2}{2}\right|_{k=k_{max}} \tag{4.5}$$

where N_c is the number of channels per manifold and K_c / K_e are loss coefficients. K_c / K_e are functions of area ratio and Reynold's number which for microchannels can be obtained from an investigation by Kays and London [36]. The pressure drop within the entrance region (k = 1) is:

$$\Delta P_{er} = fRe \left.\frac{2L_{er}\,\mu_g\,W_{tot}}{\rho_g\,A_c\,D_h^2}\right|_{k=1} \tag{4.6}$$

where L_{er} is the length of the entrance region, W_{tot} is the total inlet reactant mass flow rate, A_c is the cross-sectional area of the channel, and D_h is the hydraulic diameter of the channel. The friction factor, fRe, is given by:

$$\mathrm{fRe} = 24(1 - 1.3553\alpha + 1.9467\alpha^2 - 1.7012\alpha^3 + 0.9564\alpha^4 - 0.2537\alpha^5) \qquad (4.7)$$

4.2.2. Control Volume Analysis

At each element, the mass flow balance is evaluated to calculate the local two-phase flow conditions. The mass consumption of species within each element is governed by Faraday's Laws. Thus, the general equation for rate of mass consumption is:

$$\mathrm{W_{consumed}} = \frac{\mathrm{i_k A_r}}{\mathrm{nF}}(\mathrm{M_{reactant}}) \qquad (4.8)$$

where i_k is the local current density, A_r is the active reaction area per element, n is the number of electrons transferred per mole of species, $M_{reactant}$ is the molar mass of the reactant of interest, and F is Faraday's constant. Applying this equation to a generic element on each of the cathode and anode sides respectively yields:

$$W_{air,k} = W_{air,k-1} - \frac{i_k A_r}{n_{ca} F}(M_{air}) \qquad (4.9\ a)$$

$$W_{H_2,k} = W_{H_2,k-1} - \frac{i_k A_r}{n_{an} F}\left(M_{H_2}\right) \qquad (b)$$

where W_{k-1} is the mass flow rate from the previous element. Similarly, applying Faraday's Laws to the total water flow rate within each element yields:

$$W_{H_2O,an,k} = W_{H_2O,an,k-1} + \frac{i_k A_r M_{H_2O}}{n_{H_2O} F}(1 - m) \qquad (4.10\ a)$$

$$W_{H_2O,ca,k} = W_{H_2O,ca,k-1} + \frac{i_k A_r M_{H_2O}}{n_{H_2O} F}(m) \qquad (b)$$

where the scaling factor *m* denotes the fraction of product water transported to the cathode gas channels. The simplified form is used to quantify the net water transport across the membrane due to several transport mechanisms with varying dependence on the local operating conditions. While a

value of *m* can be obtained from in depth analysis of electro-osmotic drag, back diffusion, hydraulic permeation, and thermo-osmosis, it can also be obtained more directly from experimental data or as a net drag coefficient. Depth of analysis in this parameter should be judiciously selected, as these factors introduce significant complexity and require further investigation [30].

Within each element, the local saturation pressure can be calculated through a polynomial fit:

$$P_{sat,k} = [-2846.4 + 411.24\mathrm{T} - 10.554\mathrm{T}^2 + 0.16636\mathrm{T}^3]_k \tag{4.11}$$

where T_k is the temperature at each element [37]. Utilizing the local saturation pressure, element pressure, and net flow of reactant through the element, the maximum flow rate of water that can be evaporated into the stream is calculated by Equation 4.12.

$$W_{H_2O,g,k}^{max} = \left[\frac{W_{reactant}\left(\frac{P_{sat}}{P}\right)}{1-\left(\frac{P_{sat}}{P}\right)}\right]_k \tag{4.12}$$

The rate of evaporation and magnitude of change in water mass flow rate can affect whether this value is achieved in each element which is accounted for using a limiting factor. The assumption of thermal equilibrium forces the limiting factor to 1 which reduces the equation for gaseous water mass flow rate to a simple logic statement as shown in Equation 4.13.

$$W_{H_2O,g,k} = \begin{cases} W_{H_2O,k}\,, & W_{H_2O,g,k}^{max} \geq W_{H_2O,an,k} \\ W_{H_2O,k}^{max}\,, & W_{H_2O,g,k}^{max} < W_{H_2O,an,k} \end{cases} \tag{4.13}$$

The assumption of thermal equilibrium could be relaxed to capture the effect of air flow rate on local relative humidity in each element through further investigation. The local humidified reactant properties, most notably density and viscosity, can be calculated through a number of widely available correlations, which were summarized well by Tsilingiris [38].

Using local fluid properties, the generic equation for the Lockhart-Martinelli parameter is:

$$\mathrm{X}_k = \left[\left(\frac{\mu_l}{\mu_g}\right)^{0.1}\left(\frac{\rho_g}{\rho_l}\right)^{0.5}\left(\frac{1-x}{x}\right)^{0.9}\right]_k \tag{4.14}$$

where μ_g is the viscosity and ρ_g is the density of the humidified reactant stream. The mass quality ratio, x, for the cathode and anode sides respectively is given by:

$$x_{ca,k} = \left[\frac{W_{air}+W_{H_2O,g}}{W_{air}+W_{H_2O}}\right]_k \tag{4.15a}$$

$$x_{an,k} = \left[\frac{W_{H_2}+W_{H_2O,g}}{W_{H_2}+W_{H_2O}}\right]_k \tag{b}$$

Many widely available correlations for the Chisholm parameter can be used, however none have been developed specifically for PEMFC conditions. Using the correlation proposed by English and Kandlikar [9], the Chisholm parameter is:

$$C = 5\left(1 - e^{-0.319\mathrm{D}_h}\right) \tag{4.16}$$

where D_h is the hydraulic diameter. This was later modified by Grimm et al. [16] through the use of:

$$C = \mathrm{A}\left(\frac{1-x}{x}\right)^b \tag{4.17}$$

where A is given by:

$$A = 0.0856(U_L)^{-1.202} \tag{4.18}$$

and where b is given by:

$$b = 0.0856(U_L)^{-0.526} \tag{4.19}$$

The two-phase pressure drop is then calculated using the correlation proposed by Lockhart [7] shown in Equations 4.20 and 4.21:

$$\phi_{g,k}^2 = [1 + CX + X^2]_k \tag{4.20}$$

$$\Delta P_{E,k} = \left[\phi_g \, \Delta P_g\right]_k \tag{4.21}$$

where ΔP_g is the single-phase gas pressure drop, which is given by:

$$\Delta P_{g,k} = \left[fRe \frac{2 L_e \, \mu_g \, W_{tot}}{\rho_g \, A_c \, D_h^2}\right]_k \tag{4.22}$$

Additionally, it should be noted that in the case of mist flow a homogenous two-phase pressure drop model can be substituted. The two-phase viscosity can be calculated by:

$$\mu_{tp} = \left[\beta \mu_g + \mu_l (1 - \beta)\right]\Big|_{k=1} \tag{4.23}$$

where β is the volumetric quality which is given by:

$$\beta = \left[\frac{Q_{air} + Q_{H_2O,g}}{Q_{air} + Q_{H_2O}}\right] \tag{4.24}$$

as proposed by Dukler [6]. The two-phase density is given by the ratio of mass quality to phase density, as shown in Equation 4.25.

$$\rho_{tp} = \left[\frac{x}{\rho_g} + \frac{(1-x)}{\rho_l}\right] \tag{4.25}$$

By modifying Equations 4.20 and 4.21 to represent the exit region, the pressure drop can be represented by Equations 4.26 and 4.27.

$$\Delta P_{g,ex} = fRe \frac{2 L_{ex} \, \mu_g \, W_{tot}}{\rho_g \, A_c \, D_h^2}\Big|_{k=k_{max}} \tag{4.26}$$

$$\Delta P_{ex} = \phi_{g,k_{max}} \Delta P_{g,ex} \tag{4.27}$$

The summation of these ΔP values along the length of the channel provides the total PEMFC pressure drop (Equation 4.1).

4.3. Model Implementation

4.3.1. Model Flow Structure

The complete modeling procedure is represented by the combination of the control volume analysis and elemental pressure drop summation as represented in Figure 21.

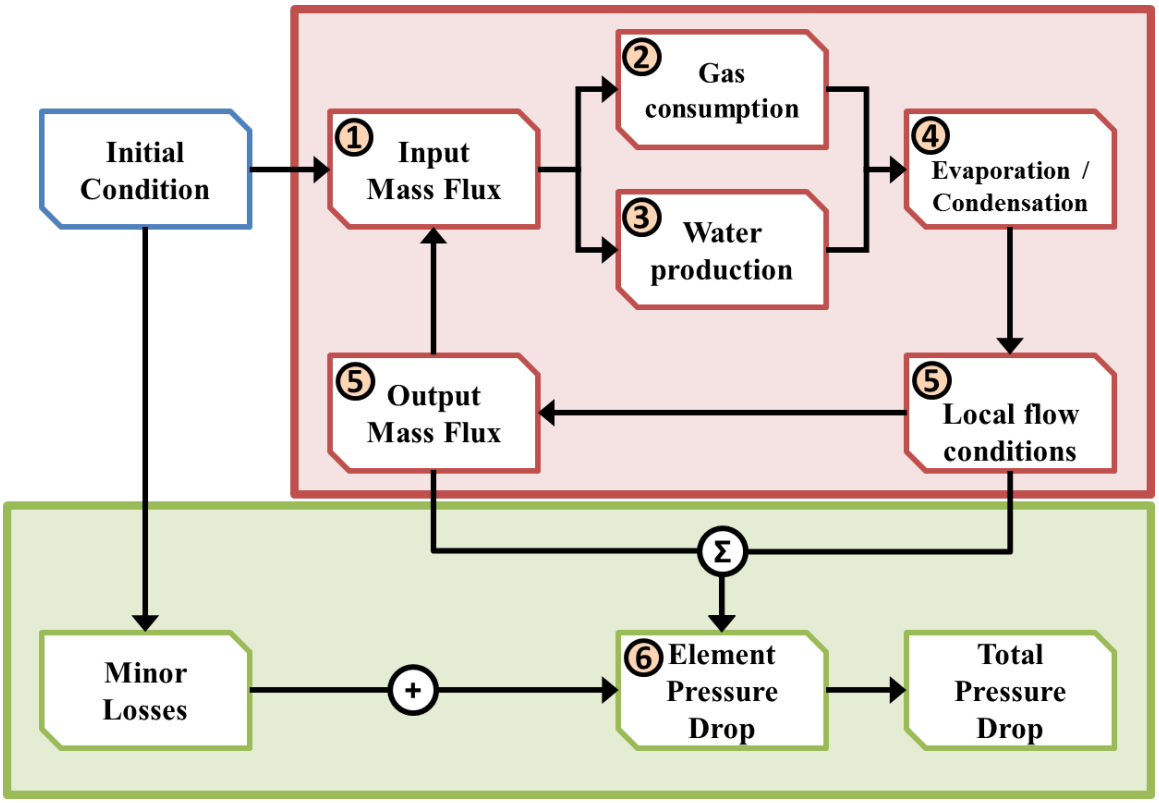

Figure 21 – Flow Diagram of Modeling Scheme

Blue – Operating Condition, Red – Control Volume Analysis,
Green – Elemental Pressure Drop Summation

Further details of the procedure within each element are as follows; equations are shown for cathode side only for brevity.

1) Using the previous element or initial condition, the input mass flux of water and reactant gases is assigned.

2) Using Faraday's law, the mass flux of reactant gas is calculated based on current density at the element.

$$W_{consumed} = \frac{i_k A_r}{n_{reactant} F}(M_{reactant}) \tag{4.28}$$

3) Similarly using Faraday's law, the mass flux of water is increased or reduced based on the current density and a factor, m, which represents the fraction of product water to the cathode.

$$W_{H_2O,k} = W_{H_2O,k-1} + \frac{i_k A_r M_{H_2O}}{n_{H_2O} F}(m) \tag{4.29}$$

4) A corresponding saturation pressure for the element is used to calculate the maximum water carried by the reactant stream in gaseous form. The mass flux of water is then split into its corresponding phases (liquid and gaseous) and a thermal equilibrium is assumed.

$$W_{H_2O,g,k}^{max} = \left[\frac{W_{reactant}\left(\frac{P_{sat}}{P_k}\right)}{1-\left(\frac{P_{sat}}{P_k}\right)}\right]_k \tag{4.30}$$

5) Resulting mass flux of liquid water, gaseous water, and reactant gases are used to calculate density, viscosity and quality for both phases. These fluid properties are used to calculate two-phase multiplier and single-phase gas pressure drop.

$$\Delta P_{g,k} = \left. fRe \frac{2 L_k \mu_g W_{tot}}{\rho_g A_c D_h^2} \right|_k \tag{4.31}$$

6) The pressure drop from each element is summed as steps 1-5 are repeated.

In Step 5, many widely available correlations for the Chisholm parameter, C, can be used, including those summarized in Table 1. However, very few correlations have been developed specifically for PEMFC conditions. Correlations proposed by Grimm et al. [16], English and Kandlikar [9], and Lee and Lee [10] provide reasonable predictions. However, additional research in the correlation for Chisholm parameter is merited.

4.4. Convergence Study

As described in Section 4.1, the channel was split into 14 elements for this work. However, several factors, such as design of test apparatus, length of reactant channels, stoichiometric ratio of reactants, and current density should be taken into account when selecting the number and sizing of elements. The minimum size of elements is bounded by the computing constraints on the model. The maximum size is recommended to not exceed 30 mm, as change in temperature, quality, and mass flux can be significant over the length of the channel. The relative error for a set number of elements was check to ensure that the prediction converged before 14 elements, as shown in Figure 22. Acceptable error values were seen at 8 elements corresponding to an element length of 29.13 mm.

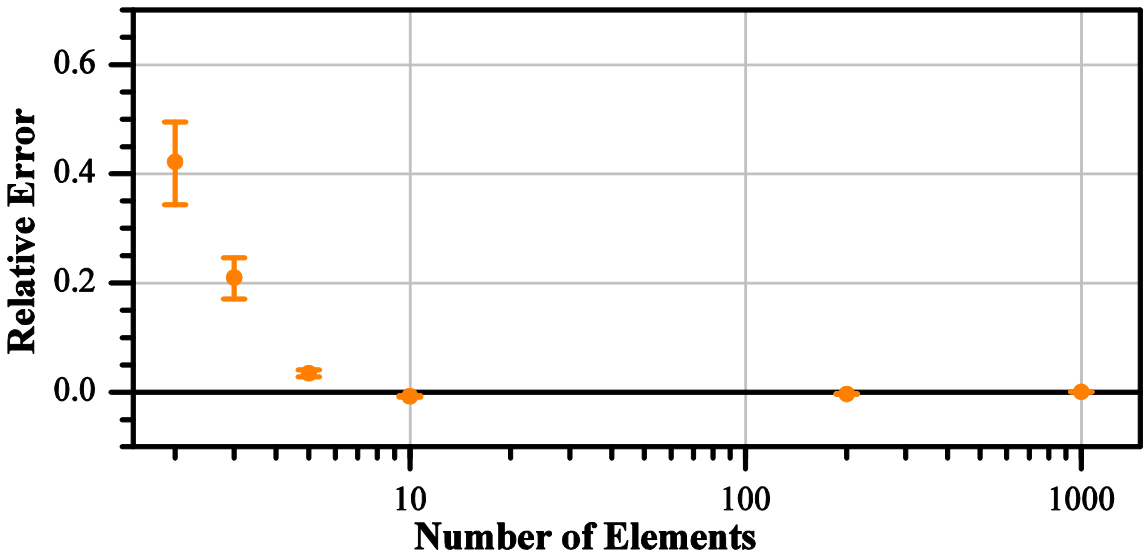

Figure 22 – Error relative to converged value of several common PEMFC conditions with changing element size.

5. Results and Discussion

5.1. Performance Evaluation

In order to ensure results were representative of commercial automotive PEMFCs, each PEM fuel cell described in Section 3.2 was performance validated. The performance of each cell was evaluated using a Greenlight Innovation G40 Fuel Cell Test Stand operated under constant current control from a TDI Load Bank for the full operating range. Each cell was broken in by constant current operation at approximately 0.6 V for 8 hours after first assembly to ensure membrane hydration.

Table 7 – Power Density of Experimental PEM Fuel Cells at 40 °C

	1.5 : 2 (Baseline)	**1.5 : 2.5 (Visualization)**	**1.5 : 5 (Visualization)**	**3 : 8 (Visualization)**
Baseline GDL Inlet RH 0%	-	0.183 W/cm^2 at 0.35 A/cm^2	0.143 W/cm^2 at 0.3 A/cm^2	0.100 W/cm^2 at 0.2 A/cm^2
Baseline GDL Inlet RH 95%	0.333 W/cm^2 at 0.5 A/cm^2 *	0.254 W/cm^2 at 0.5 A/cm^2	0.248 W/cm^2 at 0.5 A/cm^2	0.221 W/cm^2 at 0.5 A/cm^2
Freudenberg GDL Inlet RH 0%	-	0.186 W/cm^2 at 0.3 A/cm^2	0.126 W/cm^2 at 0.3 A/cm^2	0.100 W/cm^2 at 0.2 A/cm^2
Freudenberg GDL Inlet RH 95%	-	0.267 W/cm^2 at 0.5 A/cm^2	0.262 W/cm^2 at 0.5 A/cm^2	0.281 W/cm^2 at 0.5 A/cm^2

* Maximum Power Density 0.710 W/cm^2 at 1.82 A/cm^2

During pressure drop testing, a polarization curve was generated for each assembly and testing condition. The results for both PEM fuel cells are summarized in Table 5. As seen in the table, in dry conditions produced very similar maximum power densities. However, in wet conditions the Freudenberg GDL produced higher power densities by up to 20%. This was investigated by Sergi [39] and attributed to membrane hydration through high frequency resistance (HFR) measurements. Sergi [39] also attributed the decreased performance at higher current densities to the transparent materials as the “Lexan windows have an insulating effect and can cause internal cell temperature to

increase significantly at higher current densities." The baseline fuel cell showed comparable power output at low current densities; however the baseline fuel cell's more sophisticated and efficient cooling system allowed for much higher power density to be reached and higher current density operation. A power density of 0.710 W/cm^2 was achieved, over 2.5 times higher than possible with the visualization fuel cell. This is attributed to the ability to prevent membrane dehydration and more uniform temperature profiles.

As seen in Figure 23, performance did not show much variance due to stoichiometry with a fully humidified inlet and the MRC-105 GDL. However, as the stoichiometry increased with a dry inlet the performance decreased significantly. As the stoichiometry increases with a dry inlet, the amount of water that can be transported in the vapor phase increases, thus drying the fuel cell. This supports the conclusion that membrane dehydration was the primary cause for poor performance at higher current densities in the visualization fuel cell. It is important to note that at very low current densities, all showed similar performance and activation losses as should be expected.

Similarly in Figure 24, performance showed almost no variance due to stoichiometry with a fully humidified inlet and the Freudenberg GDL. However, as the stoichiometry increased with a dry inlet the performance decreased significantly. For current densities below 0.35 A/cm^2, the fully humidified and dry inlet tests for 1.5:2.5 stoichiometry showed near identical polarization curves. This suggests that both activation and ohmic losses are not directly to blame for poor performance above 0.35 A/cm^2.

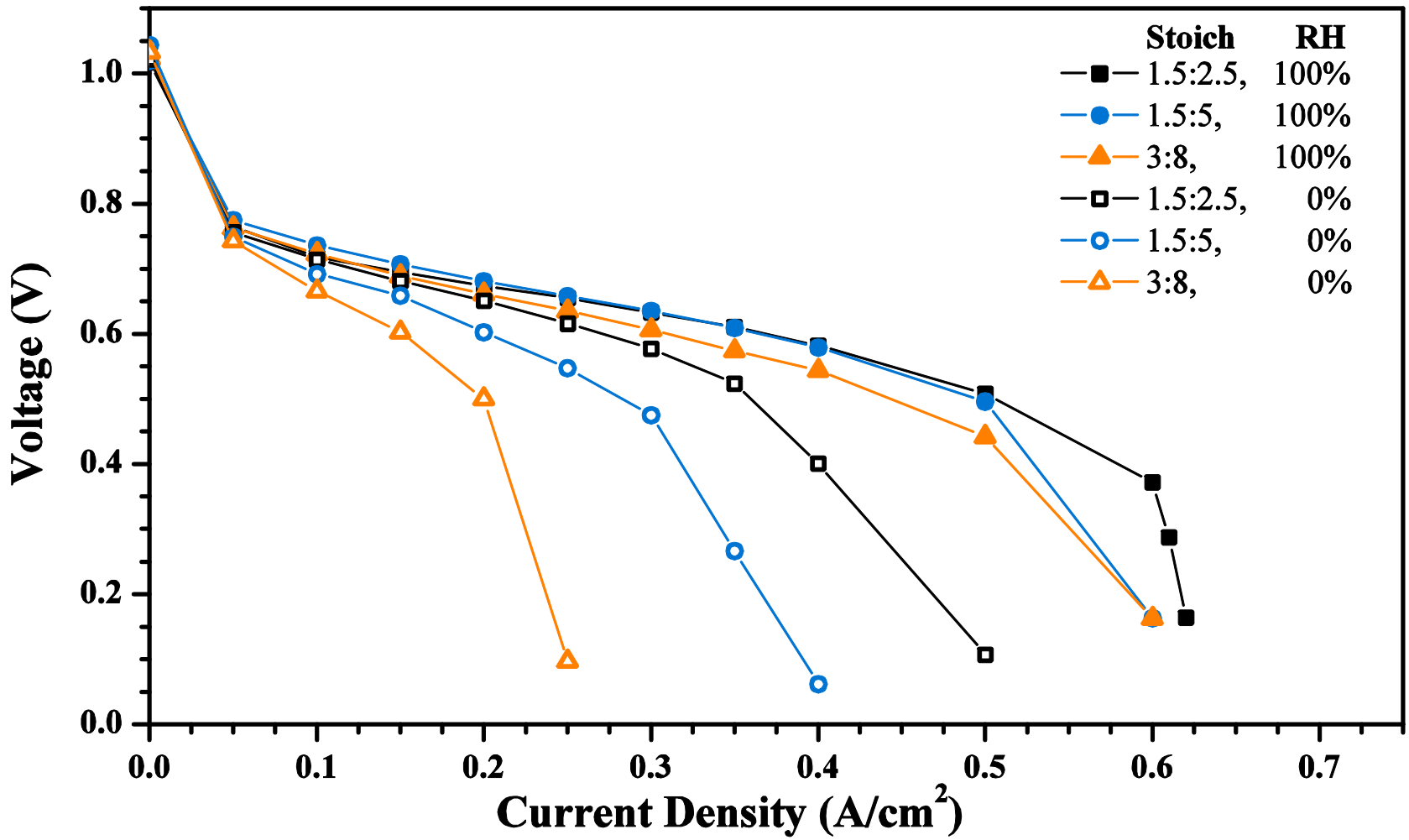

Figure 23 – Performance of Visualization PEM Fuel Cell with MRC-105 GDL

Cell temperature 40 °C, Atmospheric pressure

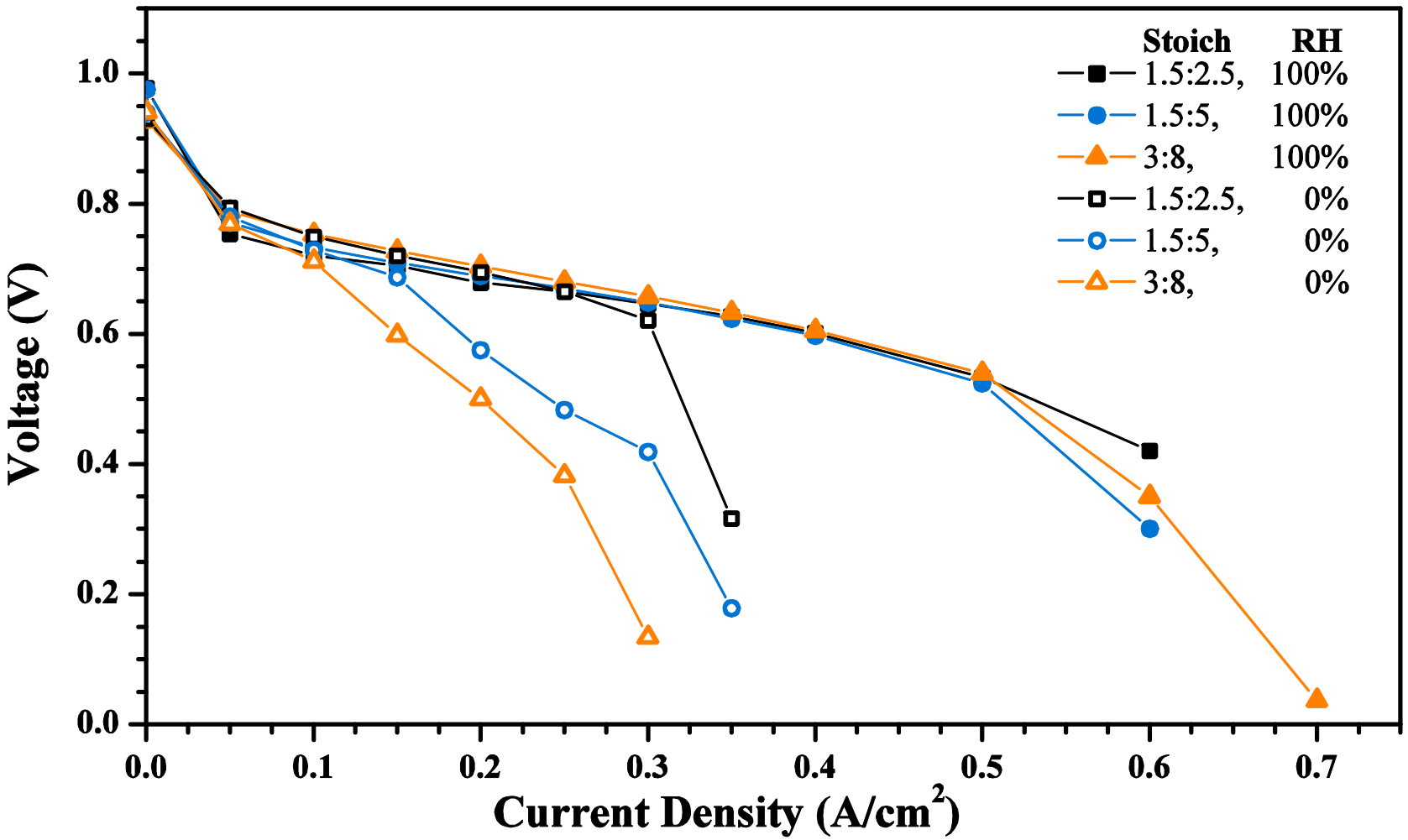

Figure 24 – Performance of Visualization PEM Fuel Cell with Freudenberg GDL

Cell temperature 40 °C, Atmospheric pressure

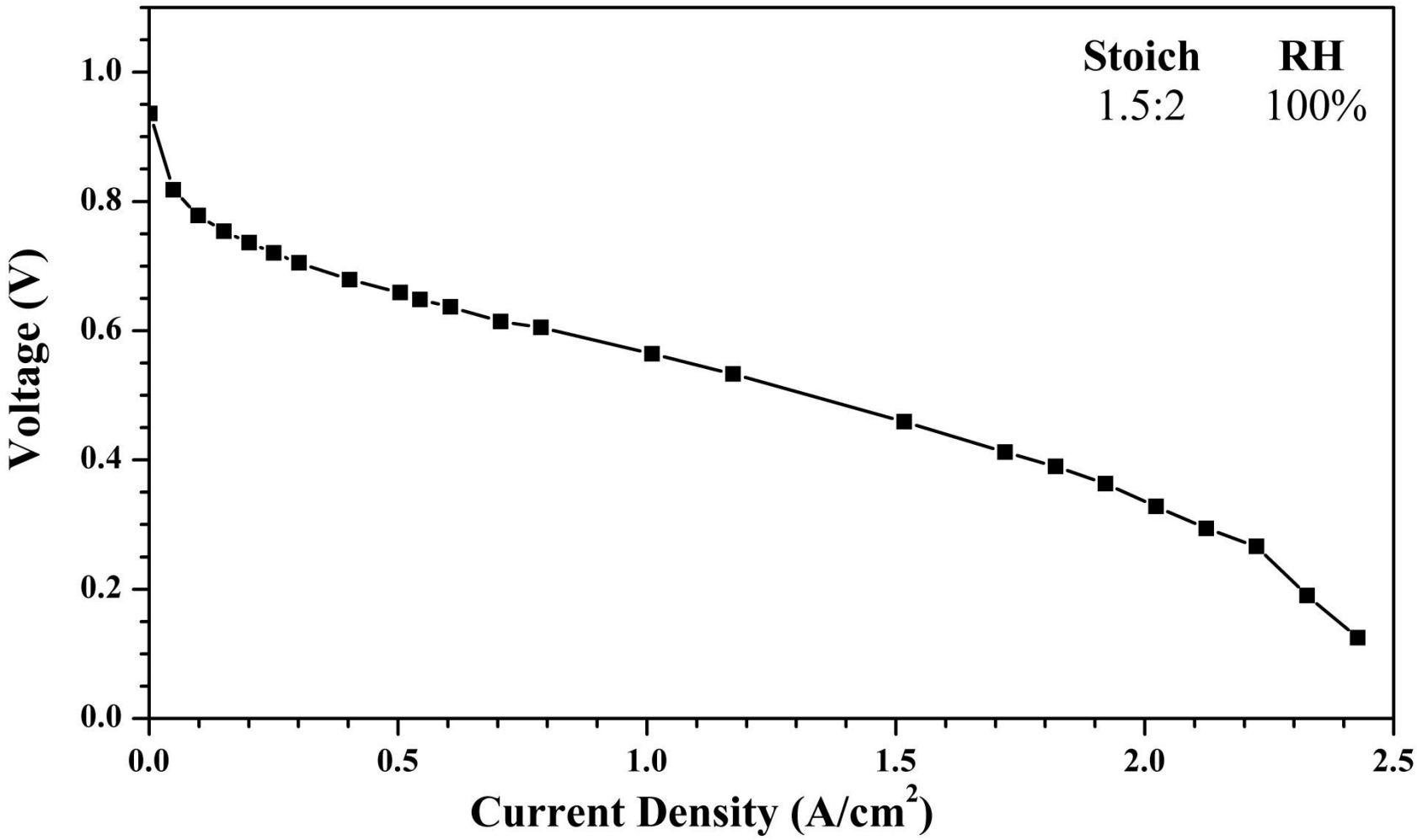

Figure 25 – Performance of Baseline PEM Fuel Cell with MRC-105 GDL

Cell temperature 40 °C, Atmospheric pressure

As shown in Figure 25, the performance of the baseline fuel cell was considerably improved over the visualization cell in high current densities. It attained peak power at 1.82 A/cm^2 and maintained 90% of that power up to 2.1 A/cm^2.

Additionally, as shown in Figure 26, over low current densities the baseline and visualization cell exhibited similar performance. Although the visualization cell exhibited greater activation losses, both cells exhibited comparable ohmic losses over the range of 0.05 to 0.30 A/cm^2. Above 0.35 A/cm^2 minor membrane dehydration was suspected, due to the work by Sergi [39], and severe dehydration was hypothesized above 0.5 A/cm^2. This suggests that cell assembly, interfacial electron resistance, and electrical component resistance was comparable between the two fuel cells and allows for a strong comparison of results.

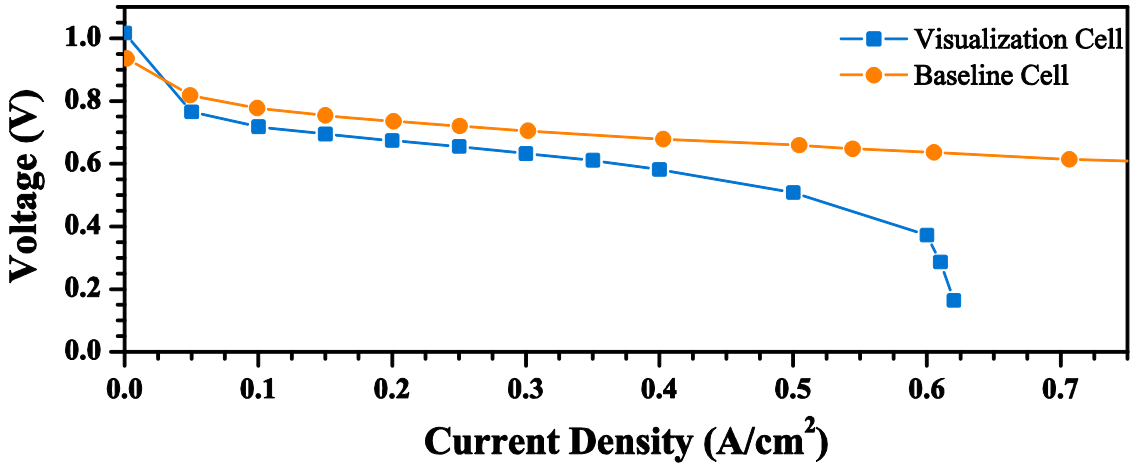

Figure 26 – Performance Comparison of PEM Fuel Cells with MRC-105 GDL

Cell temperature 40 °C, Atmospheric pressure
Stoichiometry: Visualization 1.5:2.5, Baseline 1.5:2

5.2. Thermal Gradients along the Flow Length

Typically, within PEM fuel cells a temperature gradient is seen between the inlet and the outlet of the gas channels. This can be induced by several causes including uneven reaction and poor cooling. In this work, the visualization PEM fuel cell was designed with transparent material that is very insulative. While this caused a decrease in performance at high current densities, as reviewed in Section 5.2, it allowed for study of the effect temperature gradients on two-phase flow and GDLs effect on the gradients within a PEM fuel cell. The thin foil thermocouples describe in Section 3.2.2 were used to measure the temperature just above the membrane at the start and end of the active area.

As shown in Figure 28, Freudenberg showed consistently higher temperature gradients on the cathode side of the visualization fuel cell. However, Freudenberg also showed consistently lower thermal gradients on the anode side. Additionally, in general it should be noted that stoichiometry typically showed a direct relationship with temperature gradients.

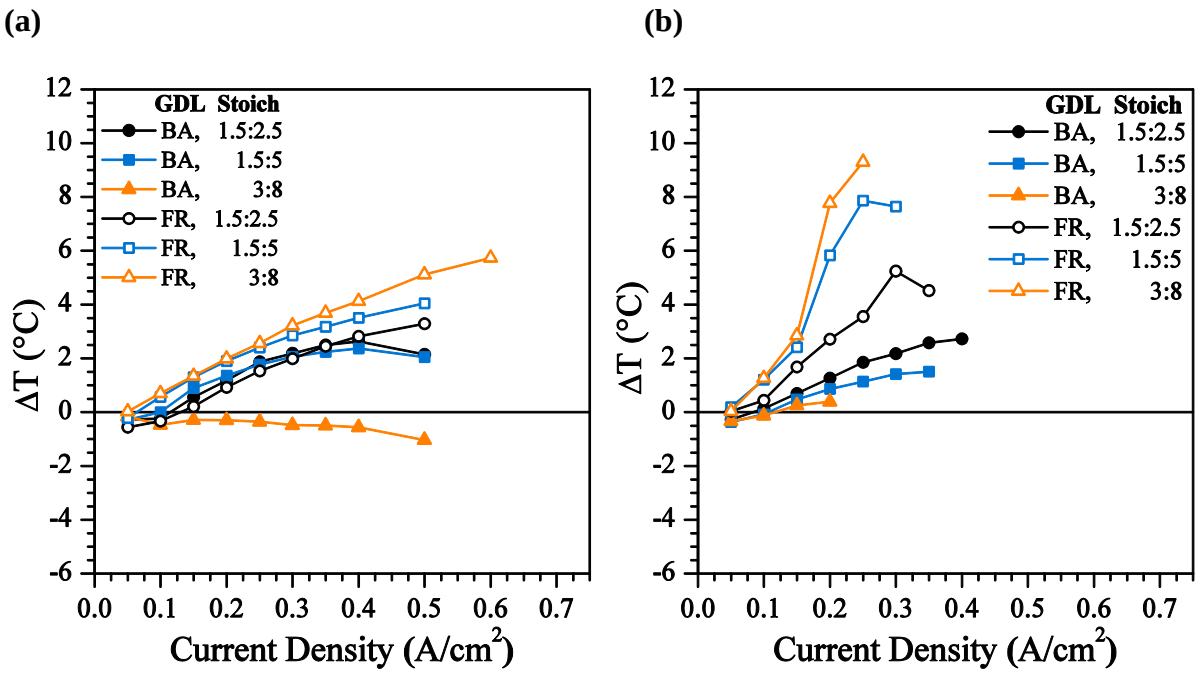

Figure 27 – Thermal Gradient along the flow length of Cathode of the Visualization PEMFC.

(a) 95% RH Inlet (b) 0% RH Inlet

On the cathode side with a fully humidified inlet, the two reported GDLs show notably different trends. The baseline GDL was consistent at lower stoichiometry; however at the highest stoichiometry the temperature gradient was significantly lower. However with the Freudenberg GDL, the temperature gradient increased with stoichiometry.

On the cathode side with a dry inlet, a similar trend was noted. With the baseline GDL, the temperature gradient was observed to decrease with stoichiometry. However with the Freudenberg GDL, the temperature gradient increased significantly with stoichiometry. Up to a 10 °C difference between the inlet and outlet was measured with the Freudenberg GDL, over 4 times higher than the MRC-105 GDL.

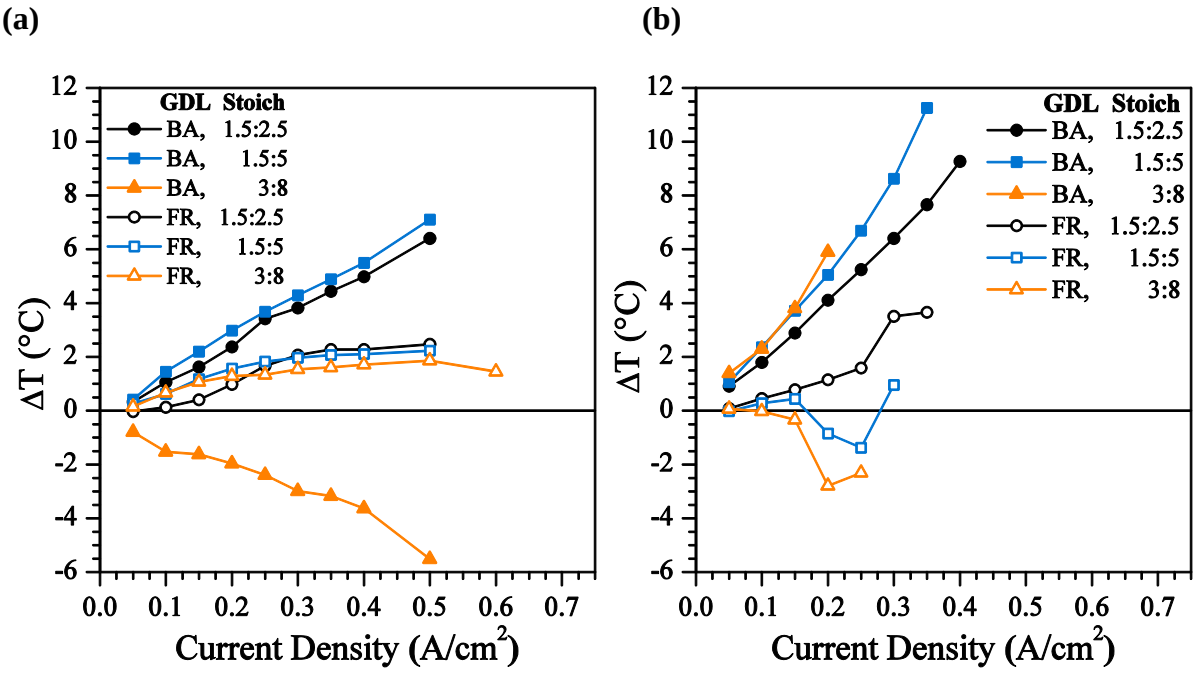

Figure 28 – Thermal Gradient along the flow length of Anode of the Visualization PEMFC.

(a) 95% RH Inlet (b) 0% RH Inlet

As shown in Figure 28, MRC-105 showed consistently higher temperature gradients on the anode side of the visualization fuel cell. On the anode side with a fully humidified inlet, the two reported

GDLs showed reversed trends from the cathode. Relatively large temperature gradients were seen with the MRC-105 GDL at lower stoichiometry; however at the highest stoichiometry the temperature gradient reversed. This was due to overheating of the membrane (50.6 °C) versus the overall cell condition (40 °C). However with the Freudenberg GDL, the temperature gradient remained consistent with stoichiometry.

On the anode side with a dry inlet, a similar trend was noted. With the MRC-105 GDL, the temperature gradient was observed to increase with stoichiometry, however the overheating was not observed. The temperature gradient decreased with stoichiometry with the Freudenberg GDL on the anode side of the membrane. On the anode side, up to an 11 °C difference between the inlet and outlet was measured with the MRC-105 GDL, over 3 times higher than the Freudenberg GDL.

These varying temperature gradients have a direct effect on the pressure drop within the system. A large positive temperature gradient allows for significant water transport in the vapor phase, thus reducing the two-phase multiplier. This was seen to occur with the MRC-105 GDL on the anode side at stoichiometries of 1.5:2.5 and 1.5:5. Conversely, a minimal temperature gradient when combined with a fully humidified inlet can cause significant condensation and lower local channel quality than traditionally predicted. This was seen particularly with the Freudenberg GDL on the anode side. Additionally, over the large range of PEM fuel cell operating conditions variance in temperature causes changes in density and viscosity of the humidified reactants. The temperature gradients reported within this section were used to calculate the local temperature within each element to accuracy represent local flow conditions.

5.3. Flow Pattern Maps

In order to determine local conditions within the PEM fuel cell channel, the mass flux of water and its phase must be determined. In order to quantify the phase of the water in the channel, it is important to determine the type of flow regimes present. Using visual observation, it was seen that flow regime did vary due to many factors including temperature gradient, stoichiometry, and operating temperature. Four observation locations were used and the average quality was used for the observation window. In order to provide a cohesive analysis, all of these factors were incorporated into superficial gas and liquid velocity to provide a basis for comparison. Traditionally within the two-phase flow community flow pattern maps, such as Figure 29, are used to compare the flow regime over set operating conditions. Little variation was seen been the flow pattern maps was seen between GDLs when all factors were accounted for in the analysis. It is important to note that a fully humidified inlet caused a shift in the flow pattern map, exhibiting significantly more slug flow. Additionally, previous ex-situ study by Grimm et al. at low temperature showed transitions at values above 5 m/s superficial gas velocity. The results in this study more closely match the results seen by Mishima and Hibiki [4] and previous studies [10,13] which all see transitions in the range of 1 m/s superficial gas velocity.

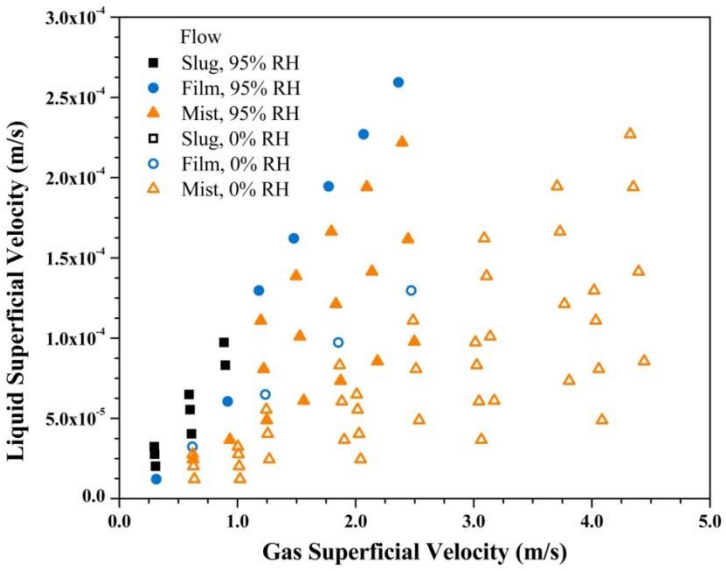

Figure 29 – Flow Pattern Map for Visualization PEMFC with MRC-105 GDL

5.4. Pressure Drop Measurement

The PEM fuel cell testing facility described in Section 3.1 was used to simultaneous measure anode and cathode channel pressure drop during operation. Measurement was assumed to be the steady state pressure drop and the procedure describe in Section 3.5 was utilized to prevent the measurement of transient effects. Significant validation was performed to assure steady state and a representative sample was attained during testing. After reaching steady state, relatively short (< 100 seconds) samples were taken, shown in Figure 30.

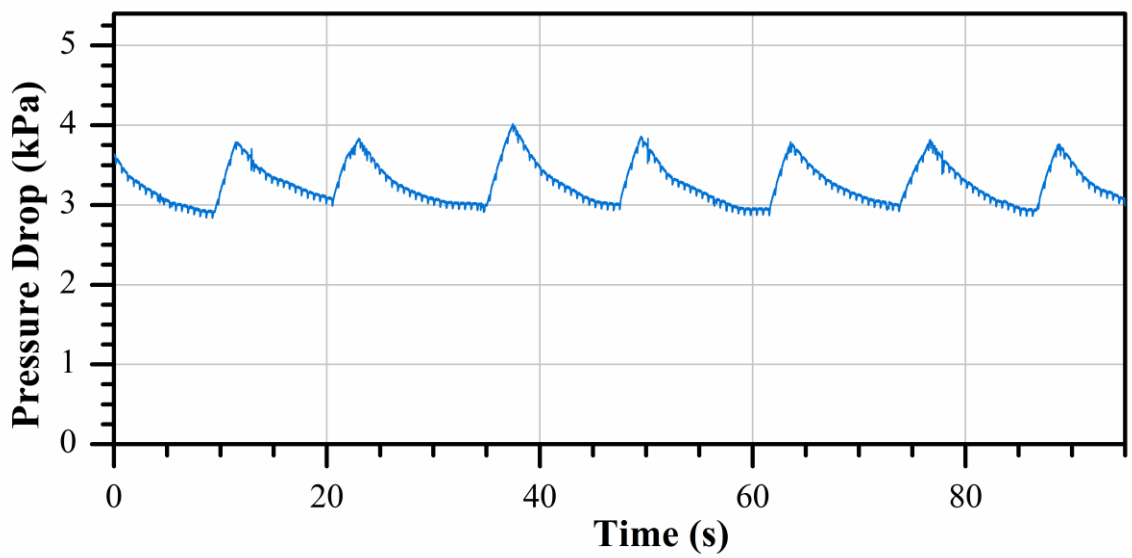

Figure 30 – Pressure drop over a relatively short time scale

Over this time scale, the pressure drop appears to be consistent and provides an acceptable representative sample. The largest spikes represent water ejection from the channel and manifold and are very consistent in frequency and magnitude. Additionally, more frequent fluctuation are seen throughout the time period which have been visually correlated to droplet movement and emergence. Finally, at approximately 14, 50, and 77 seconds intermediate fluctuations are seen. These were visually correlated to the development and coalescence of droplets into small films. Despite the appearance of timescales as short as 30 seconds could provide a representative sample, longer time scales were investigated.

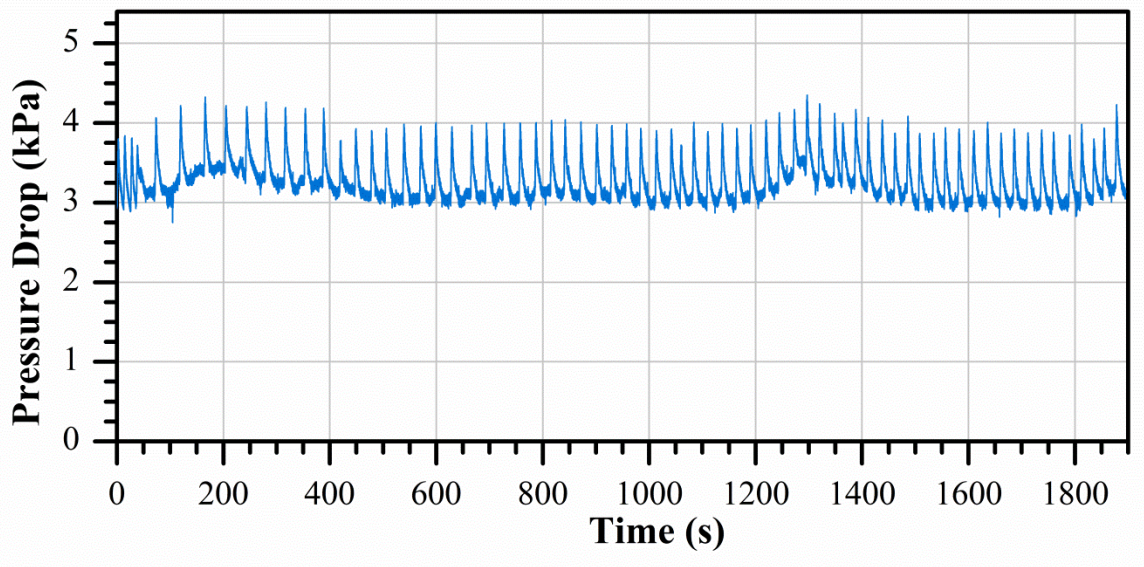

Figure 31 – Pressure drop over a realtively long time scale

Under the same conditions, a relatively long (>2000 seconds) samples were taken, shown in Figure 31. Similar trends were observed to the shorter timescale; however large fluctuations were seen in the overall trend as far as 1000 seconds apart. These fluctuations created as much as 10% variation. In order to provide a representative average for the channel, the pressure drop was recorded for a minimum of 3600 seconds and averaged. Once the length of recording had been established, 198 tests were run each four times generating approximately 800 average pressure drop measurements for each cathode and anode side. Approximately 100 selected conditions were used for the reported figures, which provide a representative sample of the entire data set.

As summarized in Figure 32, on the cathode side with a dry inlet, a linear trend was noted. With the MRC-105 GDL and 1.5:2.5 stoichiometric ratio, the pressure drop remained near constant from 0.15 A/cm^2 to 0.3 A/cm^2 suggesting that the two-phase multiplier should be decreasing as less water is stagnant in the channel. The higher stoichiometries both exhibited a similar non-linear region, however as stoichiometry increased the region was much smaller. Additionally the dry inlet with a stoichiometry of 3:8 was observed to have the highest pressure drop, despite dry conditions typically having lower pressure drop than fully humidified.

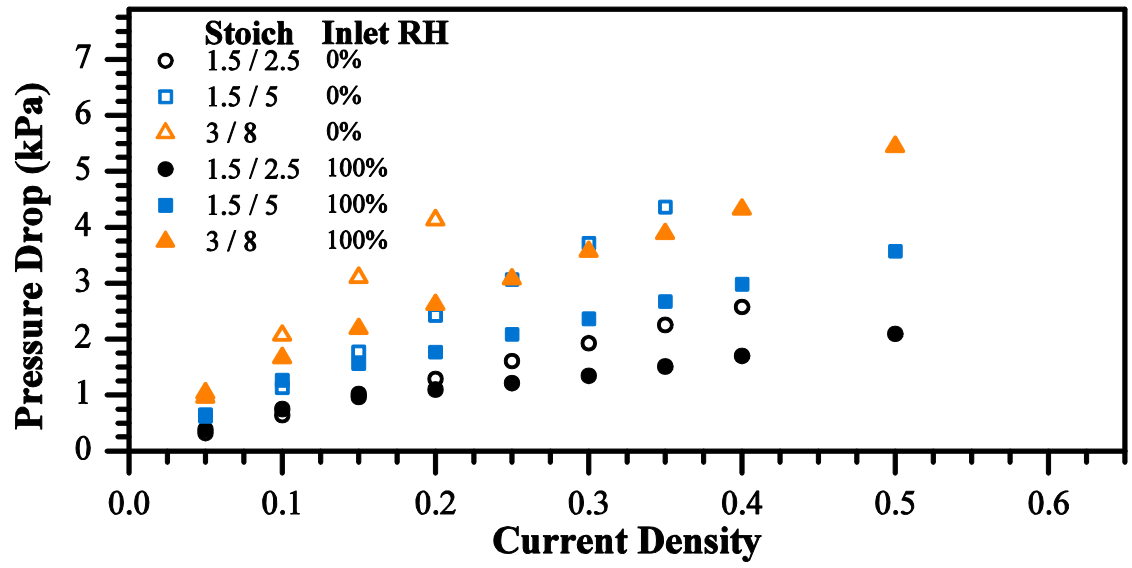

Figure 32 – Summary of Average Pressure Drop on Cathode side of Visualization PEMFC with MRC-105 GDL

As summarized in Figure 33, on the anode side non-linear trends were noted. With the 1.5:2.5 and 1.5:5 stoichiometric ratio, the pressure drop remained near identical suggesting that change in stoichiometry on the cathode side did not have a significant enough effect on water transport across the membrane to affect pressure drop.

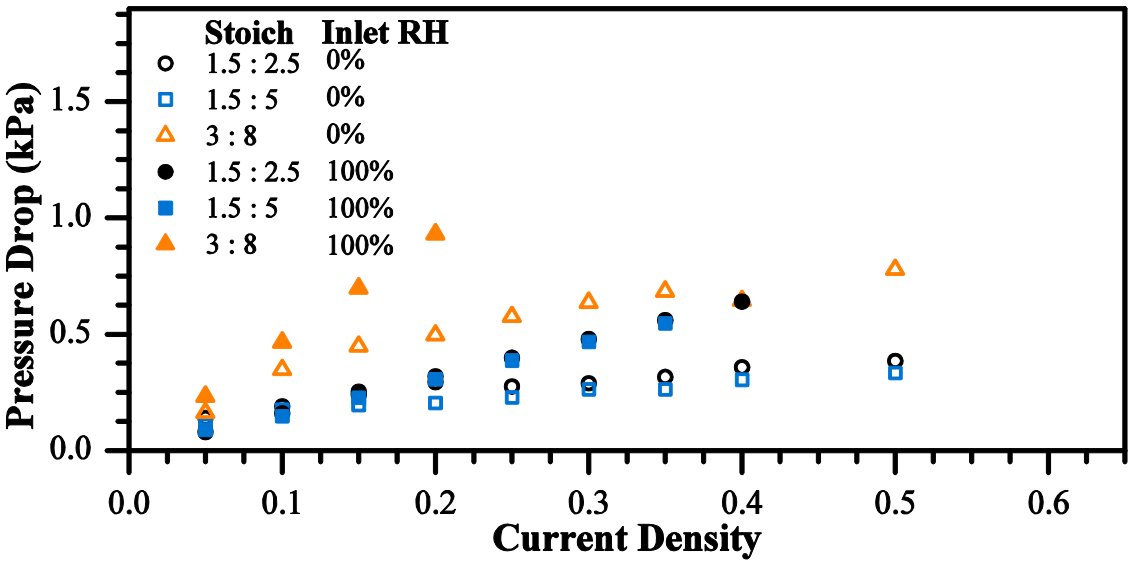

Figure 33 – Summary of Average Pressure Drop on Anode side of Visualization PEMFC with MRC-105 GDL

As summarized in Figure 34, on the cathode side with Freudenberg GDL non-linear trends were noted unlike with MRC-105 GDL. With the 1.5:2.5 and stoichiometric ratio and dry inlet, the pressure drop remained near constant suggesting that two-phase multiplier should be decreasing as less water is stagnant in the channel similar to that of the MRC-105 GDL.

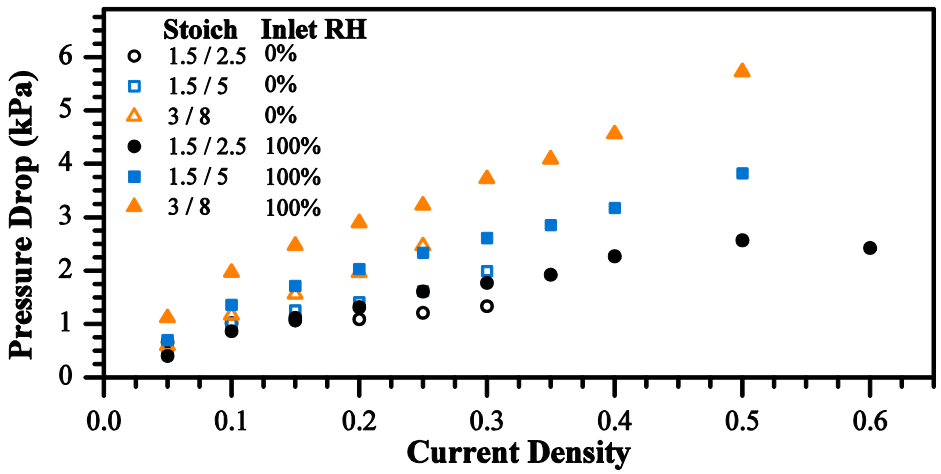

Figure 34 – Summary of Average Pressure Drop on Cathode side of Visualization PEMFC with Freudenberg GDL

As summarized in Figure 35, on the anode side very non-linear trends were noted. The pressure drop was significantly lower than that of the MRC-105 GDL at 1.5:5, and all stoichiometries showed very similar pressure drop below 0.2 A/cm^2. No clear trends were seen without further analysis of the conditions the PEM fuel cell.

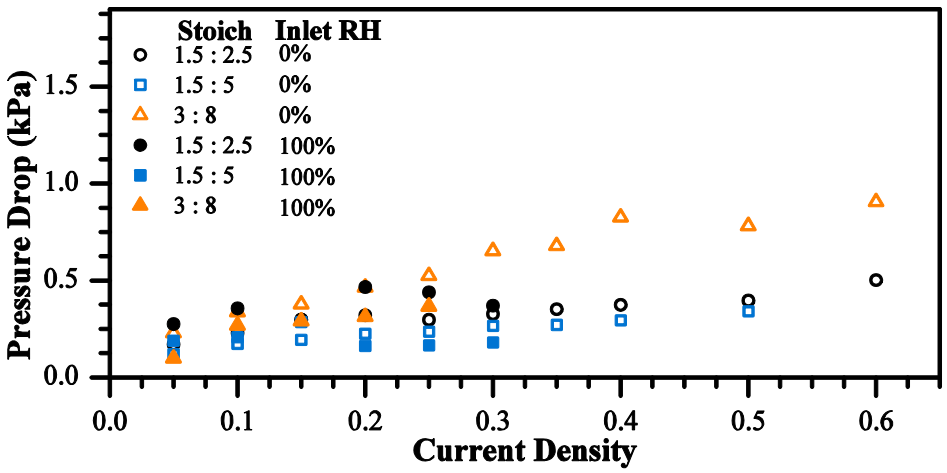

Figure 35 – Summary of Average Pressure Drop on Anode side of Visualization PEMFC with Freudenberg GDL

5.5. Two-Phase Multiplier

In order to directly relate the raw pressure drop data to a metric which is significant for two-phase flow analysis, the two-phase multiplier is utilized. The two-phase pressure drop is often expressed in terms of the two-phase multiplier with respect to the liquid or gas single-phase pressure drop. For this investigation, the two-phase multiplier is given with respect to the single-phase gas pressure drop. In order to achieve these values, pressure drop testing was run with dry gases and no load after the PEM fuel cell had been sufficiently dehumidified.

Over all conditions, the two-phase multiplier was seen to decrease with increased stoichiometry, as shown in Figure 36, Figure 37, and Figure 38. Additionally, generally the two-phase multiplier was seen to decrease with current density. Current densities above 0.6 A/cm^2 were not studied in depth as the two phase multiplier is close to 1.

As shown in Figure 36a, with a fully humidified anode inlet the two-phase multiplier decreased with current density and approaches 1 as current density increases. On the anode two-phase multiplier of 6 was measured with 1.5:2.5 stoichiometry, while the maximum measured at 3:8 stoichiometry was just below 3. By doubling the stoichiometry, the two-phase multiplier was halved. With a dry inlet, the two-phase multiplier exhibited an unexpected constant value on the anode side of approximately 3.5. After comparison of visual observations, performance data from Figure 23, and the thermal gradients from Figure 28b, it became clear that this phenomenon occurred during a membrane dehydration condition.

As shown in Figure 36b, with a fully humidified anode inlet the two-phase multiplier decreased with current density and approaches 1 as current density increases. A maximum two-phase multiplier of 3.3 was measured with 1.5:2.5 stoichiometry, while the maximum measured at 3:8 stoichiometry was just below 2.3. Unlike on the anode, the stoichiometry was increased three-fold, however the two-phase multiplier was only reduced by 50%. With a dry inlet, the two-phase multiplier exhibited an

initial value of approximately 2.5 which decreased with current density at a much lower rate than the humidified condition. Comparing the 3:8 test and 1.5:5 test with dry inlets, despite a large change in stoichiometry a very small change in two-phase multiplier was calculated. This suggests that the increase in stoichiometry did not have a significant effect on water removal.

As shown in Figure 38a, the overall anode two-phase multiplier for tests with Freudenberg GDL follows similar trend to that of the MRC-105, however average two-phase multiplier is higher. For the dry inlet tests, the two-phase multiplier follows the expected pattern of decreasing with stoichiometry and current density. However with fully humidified inlets, the two-phase multiplier only decreased with current density. Comparing the 1.5:2.5 test and 1.5:5 test, despite an identical stoichiometry on the anode side the two-phase multiplier decreases between the two tests. This suggests that the change in cathode stoichiometry caused a change in water balance between the two sides of the membrane, Additionally, the 3:8 stoichiometry tests, showed higher two-phase multiplier than expected, suggesting anode two-phase

As shown in Figure 38b, for most conditions the cathode two-phase multiplier for tests with Freudenberg GDL have very comparable values and trend to that of the MRC-105. However with a dry inlet and stoichiometry of 1.5:5, the two-phase multiplier is 50% higher than the highest value seen with MRC-105. Comparing the tests for 3:8 and 1.5:5 stociometries with fully humidified inlets, despite a large change in stoichiometry a very small change in two-phase multiplier was calculated. This suggests that the increase in stoichiometry did not have a significant effect on water removal due to the relatively low two-phase multiplier.

Overall, between the two GDLs shown in Figure 36 and Figure 37, significant variation is seen between two-phase multipliers. This suggests that local flow conditions varied significantly and factors such as uptake, local temperature, consumption, and water balance are needed to properly quantify the two-phase flow conditions.

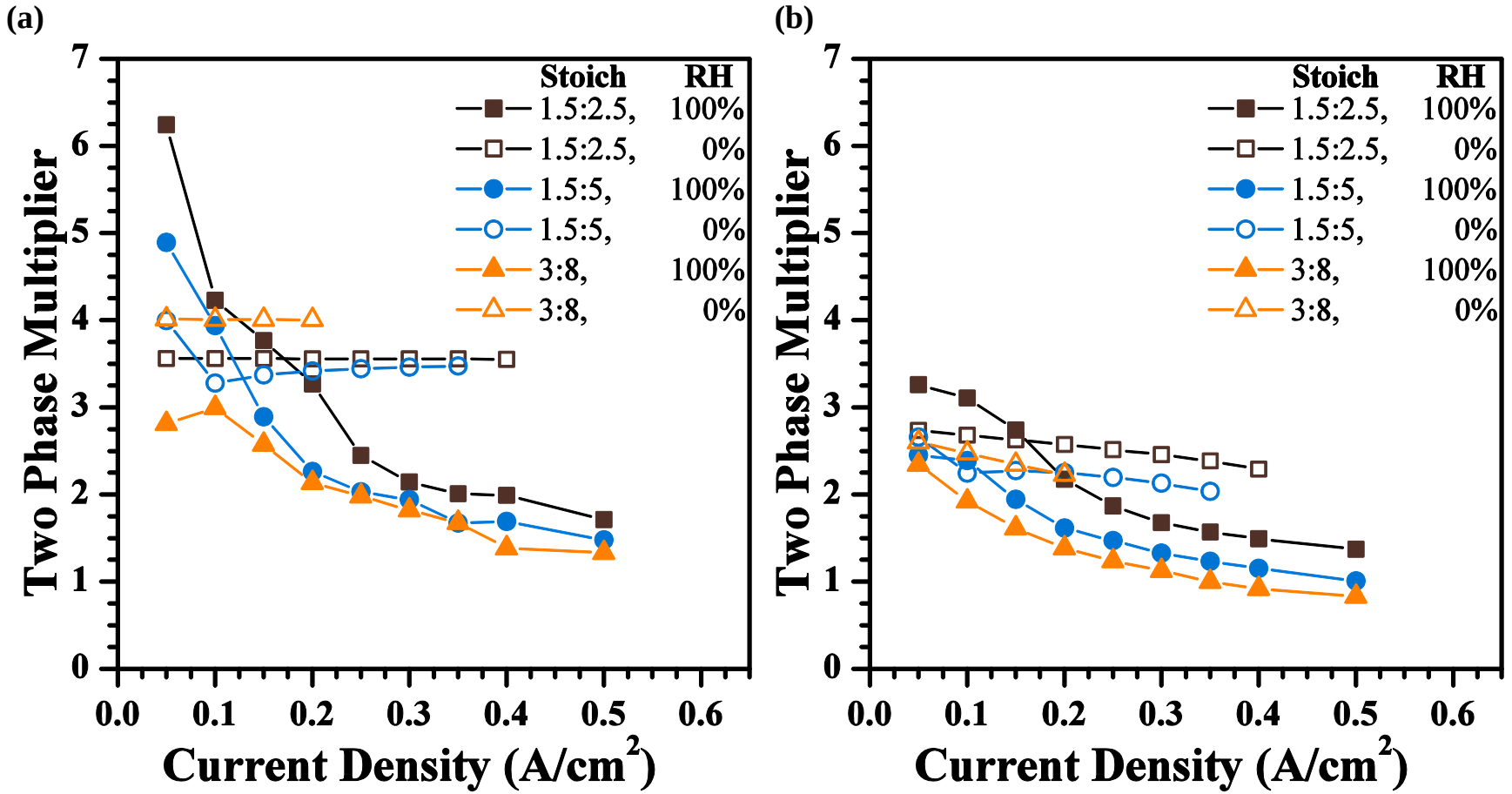

Figure 36 – Two-phase multipiler for Visualization PEM Fuel Cell with MRC-105 GDL

(a) Anode Side (b) Cathode Side

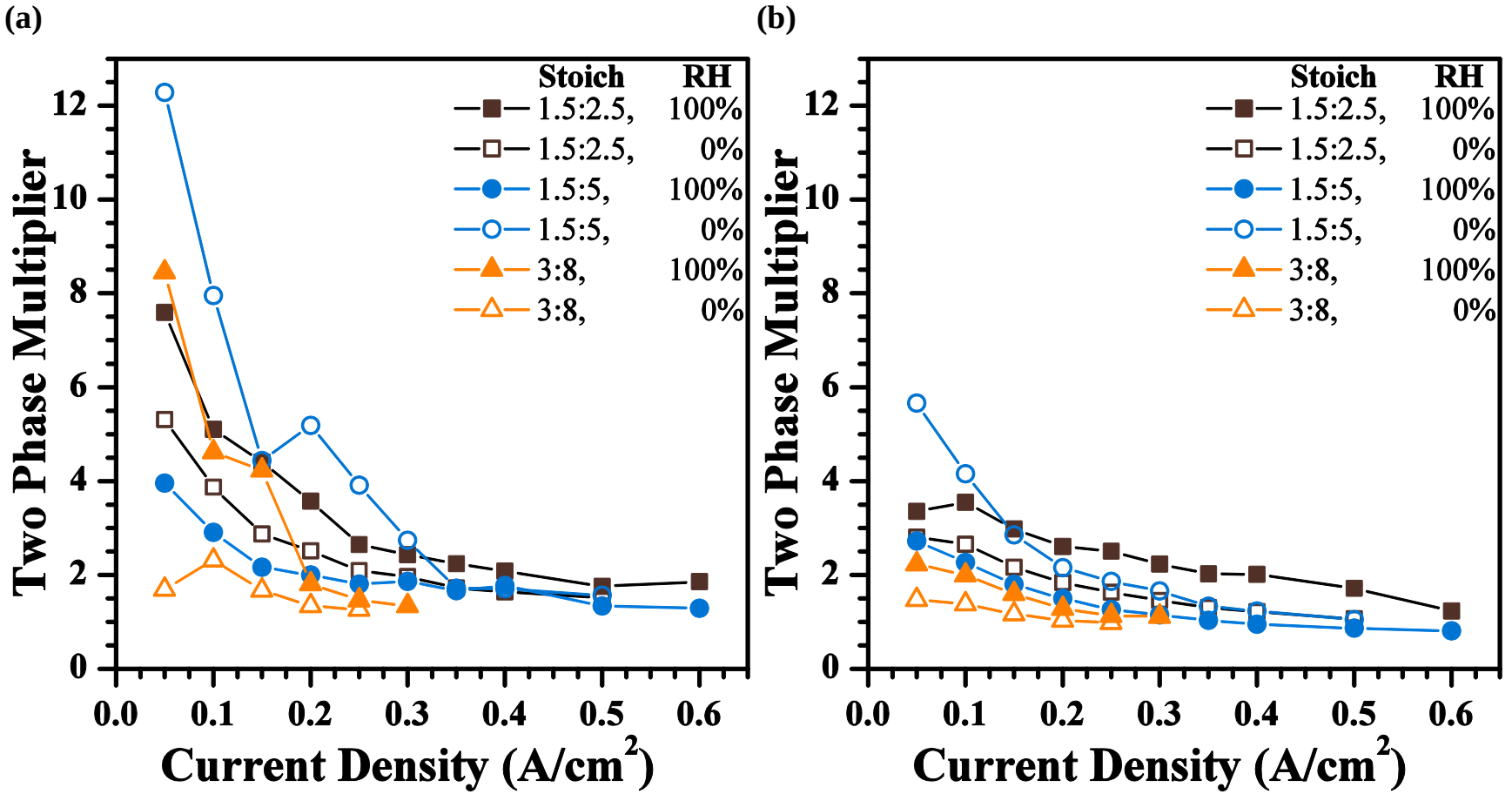

Figure 37 – Two-phase multipiler for Visualization PEM Fuel Cell with Freudenberg GDL

(a) Anode Side (b) Cathode Side

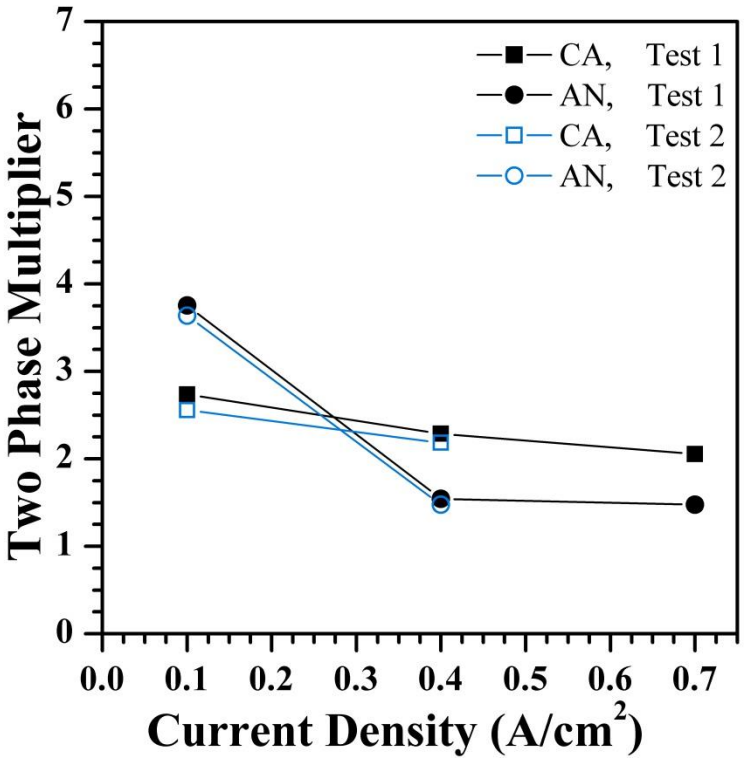

Figure 38 –Two-phase multipiler for Baseline PEM Fuel Cell with MRC-105 GDL.

Stoichiometry 1.5:2, Fully humidified inlet

In order to ensure that the visualization cell did not have inherent flaws in its two-phase pressure drop measurement, the baseline cell was tested under similar operating conditions. As shown in Figure 38, the cathode two-phase multiplier at 0.1 A/cm^2 was approximately 2.7, compared the visualization cell which was just above 3.0. The two-phase multiplier of the baseline cell was expected to be lower than that of the visualization cell due to its near isothermal thermal operation. Similarly, on the anode side the two-phase multiplier was approximately 10% lower than that of the visualization cell.

5.6. Pressure Drop Prediction

Using the thermal gradients reported in Section 5.2, the experimental pressure drop reported in Section 5.4, and the modeling scheme reported in Section 4, predictions for two-phase pressure drop were generated. Six correlations, which were summarized in Table 2, were used within the modeling scheme to assess their applicability and accuracy. These predictions were run for all collected data points (approximately 1500 predictions for each of the six correlations) in order to develop and validate the modeling scheme. For clarity, in the following section only 100 selected conditions were used for figures, which provide a representative sample of the entire data set. The range of conditions included in the selected dataset is summarized in Table 9. All selected conditions are from the visualization fuel cell to allow the comparison of visual observation and the reported figures. The error reported was calculated over the entire dataset.

Table 8 – Range of Variables for Selected Conditions

GDL	Inlet Relative Humidity	Current Density (A/cm^2)*	Stoichiometry
Baseline	0%	0.05	1.5 : 2.5
Freudenberg	95%	0.60	1.5 : 5
			3 : 8

* Increments of 0.05 A/cm^2

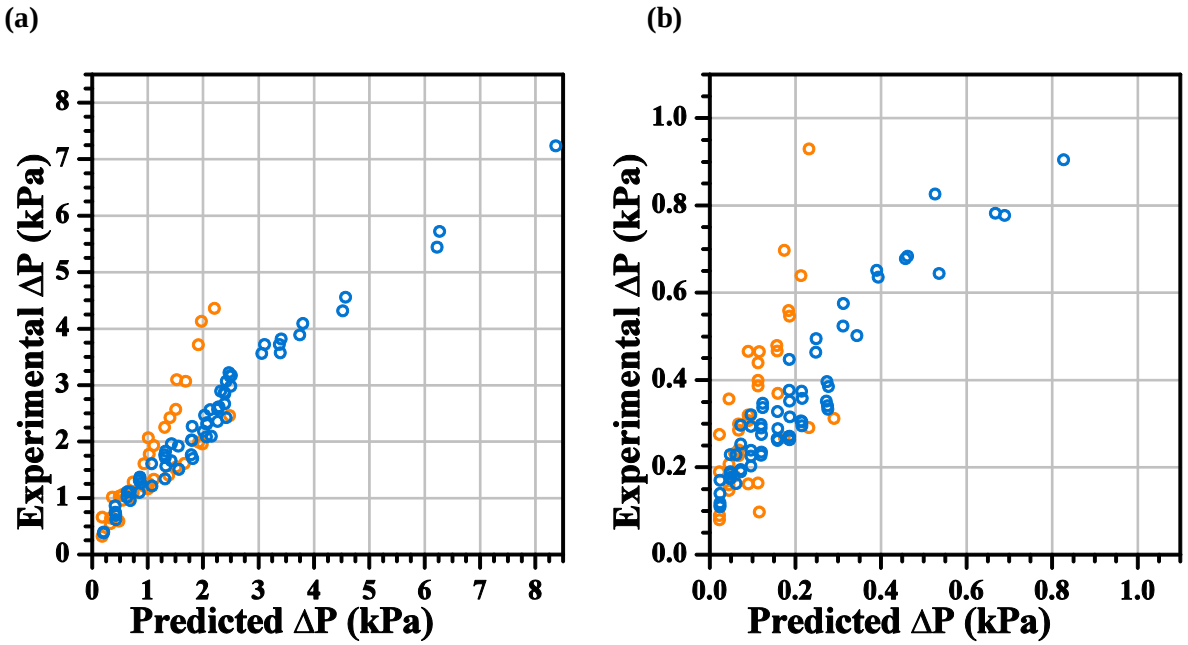

Figure 39 – Comparison between Mishima and Hibiki correlation and database

Cell temperature 40° C, Orange – 0% RH Inlet, Blue – 95% RH Inlet,
(a) Cathode Side Pressure Drop (b) Anode Side Pressure Drop

The comparison of the Mishima and Hibiki correlation used within the proposed modeling scheme and experimental data is shown in Figure 39. A mean error of 13.0% was observed for the cathode with a fully humidified inlet, while a mean error of 23.7% was observed over the entire range. A maximum error of 73.1% was observed. For a fully humidified inlet, the correlation provided a reasonable prediction of pressure drop; however, at higher pressure drops the correlation began to over-predict the data. For a dry inlet, significant under-prediction of pressure drop was noted. This under-prediction was seen in all correlations and is discussed further in Section 5.6.2.

A mean error of 56.1% was observed for the anode over the entire range. A maximum error of 91.8% was observed. Overall, the relative error was quite high; however the absolute error was reasonable, due to the extremely low pressure drop values typically seen on the anode side.

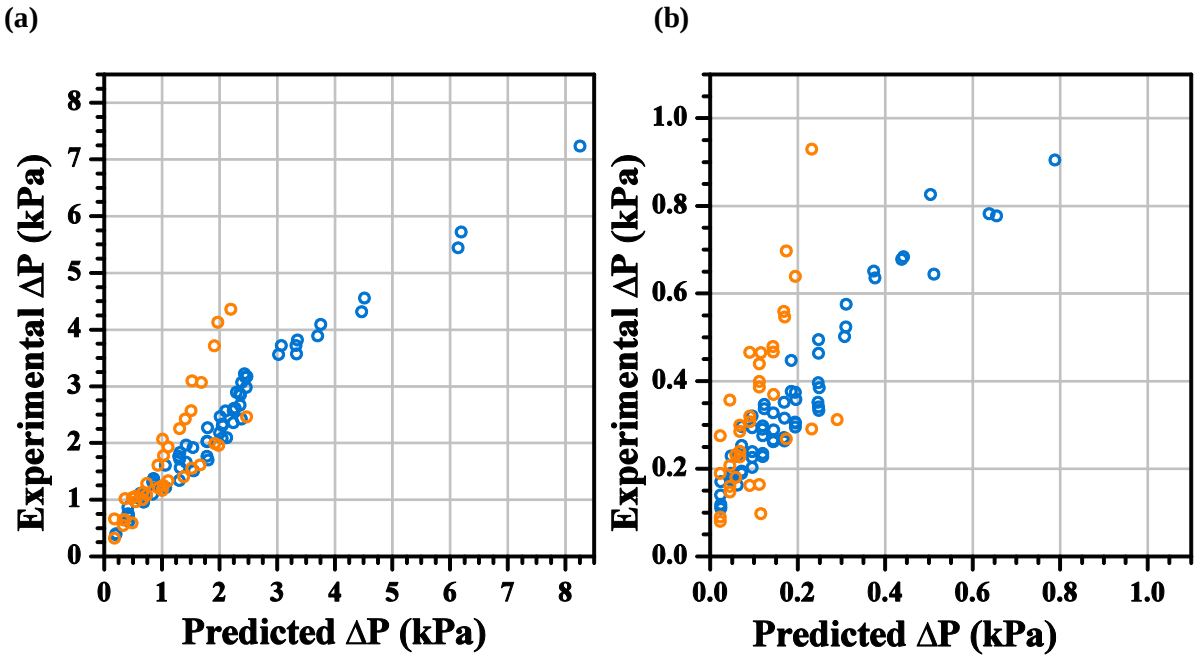

Figure 40 – Comparison between Lee and Lee correlation and database

Cell temperature 40° C, Orange – 0% RH Inlet, Blue – 95% RH Inlet,
(a) Cathode Side Pressure Drop (b) Anode Side Pressure Drop

Using the correlation by Lee and Lee, a mean error of 13.8% was observed for the cathode with a fully humidified inlet, while a mean error of 24.3% was observed over the entire range. A maximum error of 73.2% was observed. As shown in Figure 40, the correlation produced similar results to the Mishima and Hibiki correlation. For a fully humidified inlet, higher pressure drop was predicted marginally better. A mean error of 56.7% was observed for the anode over the entire range. A maximum error of 91.9% was observed.

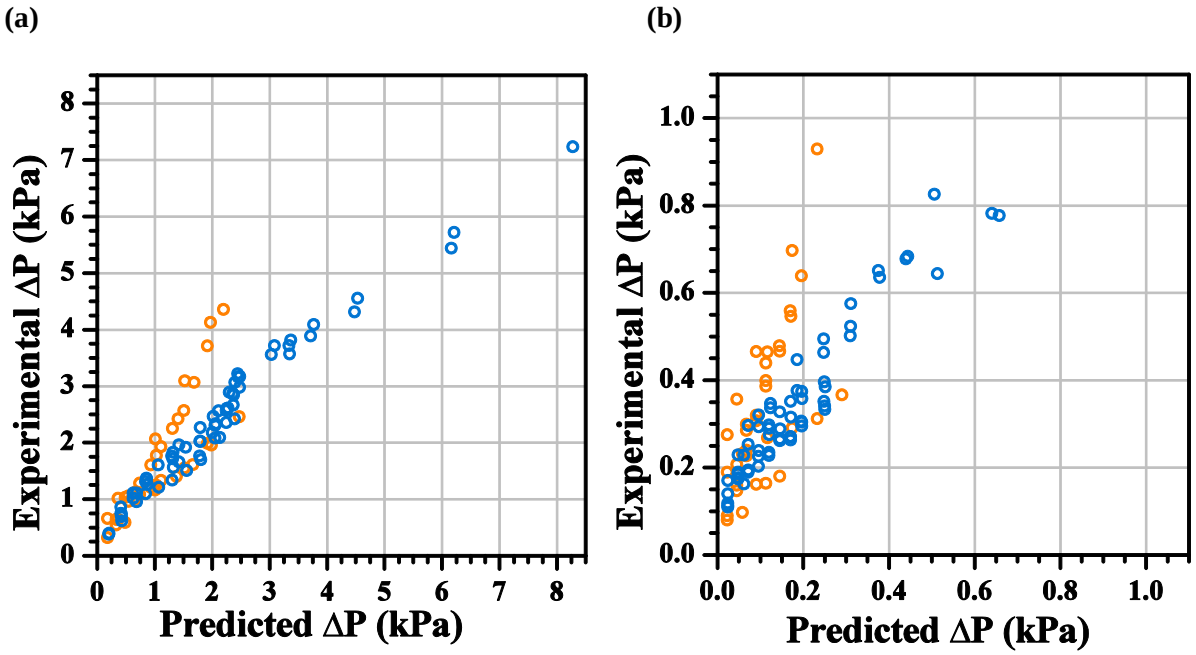

Figure 41 – Comparison between English and Kandlikar correlation and database

Cell temperature 40° C, Orange – 0% RH Inlet, Blue – 95% RH Inlet,
(a) Cathode Side Pressure Drop (b) Anode Side Pressure Drop

Using the English and Kandlikar correlation in the modeling scheme, a mean error of 5.4% was observed for the cathode with a fully humidified inlet, while a mean error of 11.6% was observed over the entire range. A maximum error of 78.4% was observed. For a fully humidified inlet, mean error is low yet consistently under predicted. For a dry inlet, predictions were near identical to that of Mishima and Hibiki and under predicted several conditions. A mean error of 48.7% was observed for the anode over the entire range. A maximum error of 80.2% was observed.

In Figure 42 showing the Saisorn and Wongwises correlation, a mean error of 18.5% was observed for the cathode with a fully humidified inlet, while a mean error of 25.4% was observed over the entire range. A maximum error of 72.9% was observed. For a fully humidified inlet, significant error is seen in the transition to high pressure drop. This is most likely due to the transition between flow regimes within the channel. Visual observations show that these data points are generally in the film to mist transition range. For a dry inlet, the prediction was comparable to the aforementioned

correlations. A mean error of 55.7% was observed for the anode over the entire range. A maximum error of 91.9% was observed.

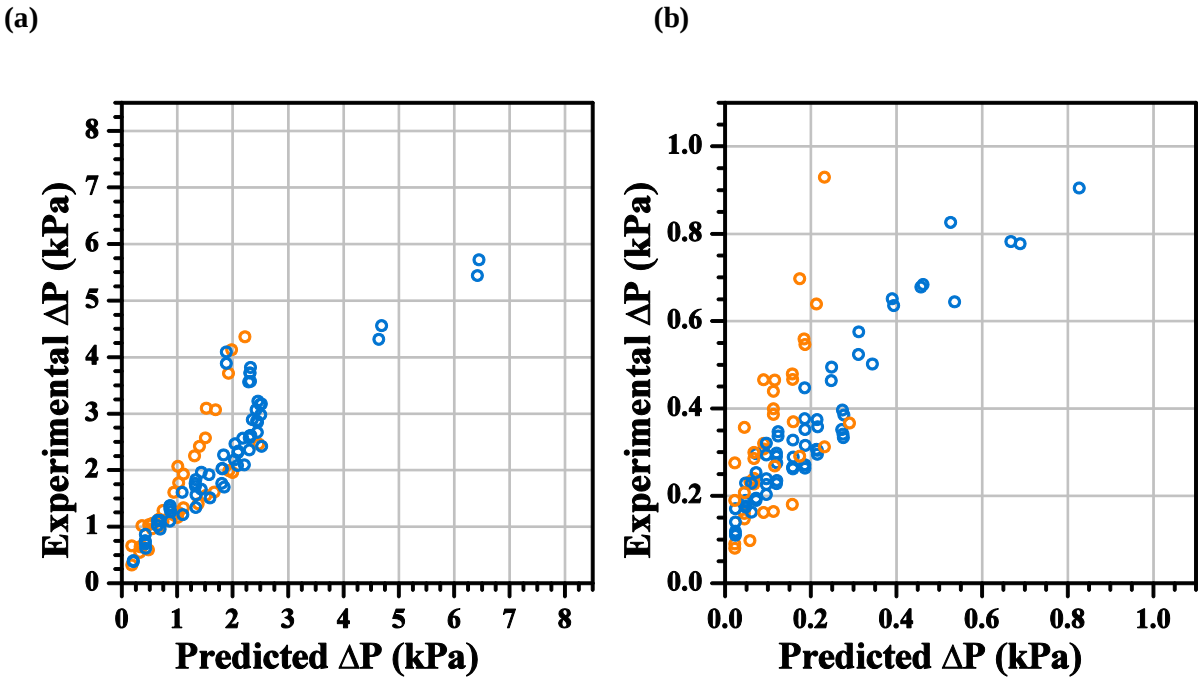

Figure 42 – Comparison between Saisorn and Wongwises correlation and database

Cell temperature 40° C, Orange – 0% RH Inlet, Blue – 95% RH Inlet,
(a) Cathode Side Pressure Drop (b) Anode Side Pressure Drop

Using the modified version of the English and Kandlikar correlation proposed by Grimm et al., a mean error of 5.2% was observed for the cathode with a fully humidified inlet, while a mean error of 11.6% was observed over the entire range. A maximum error of 78.5% was observed. Overall, the results are comparable to that of the original correlation; however a few key differences are seen. For a fully humidified inlet, the mean error is within 0.2% of the English and Kandlikar correlation. The predictions with the modified English and Kandlikar are both over and under predicted evenly unlike the unmodified correlation which only under predicts the data. For a dry inlet, less under prediction was seen than the unmodified correlation. A mean error of 40.2% was observed for the anode over the entire range. A maximum error of 82.4% was observed.

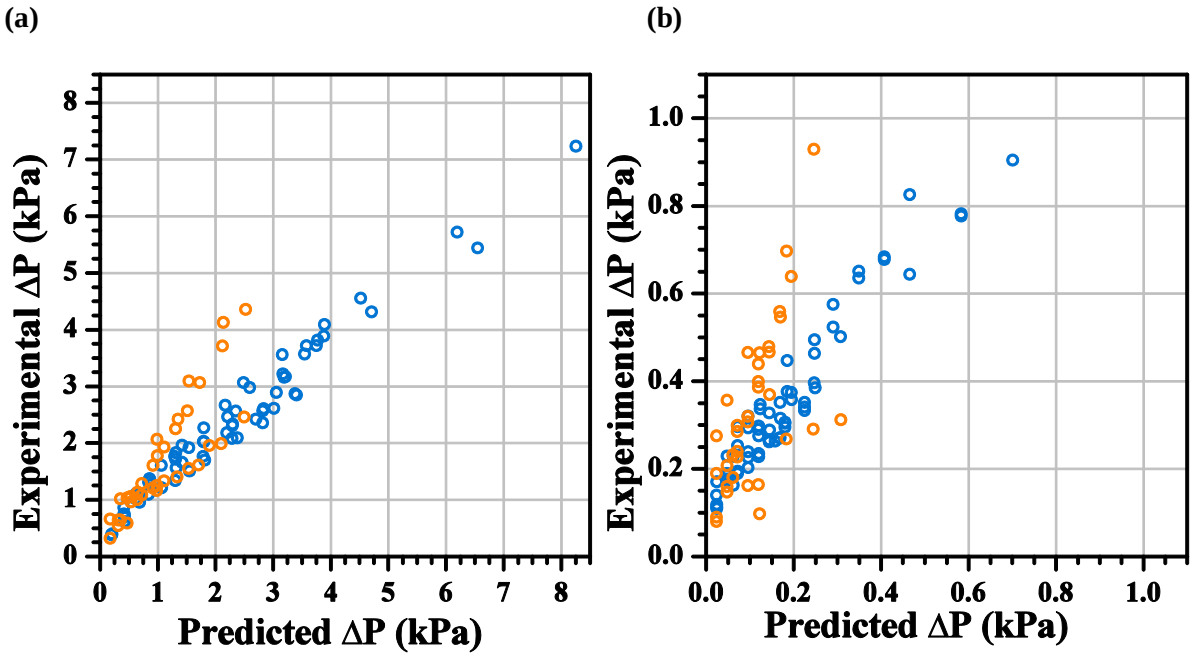

Figure 43 – Comparison between Modified English and Kandlikar correlation and database

Cell temperature 40° C, Orange – 0% RH Inlet, Blue – 95% RH Inlet,
(a) Cathode Side Pressure Drop (b) Anode Side Pressure Drop

Shown in Figure 44, for the "slug correlation" proposed by Grimm et al. [16] mean error of 6.5% was observed for the cathode with a fully humidified inlet, while a mean error of 8.8% was observed over the entire range. It is important to note that for conditions where slug flow was observed a mean error of 3.2% was obtained. A mean error of 106.0% was observed for the anode over the entire range. Although this correlation has extremely low error under very specific sets of conditions, in general it provided some of the poorest predictions.

Using the "film correlation", a mean error of 137.8% was observed for the cathode with a fully humidified inlet, while a mean error of 70.8% was observed over the entire range. A mean error of 893.3% was observed for the anode over the entire range. In general, a very poor fit was seen and results were both extremely under and over predicted.

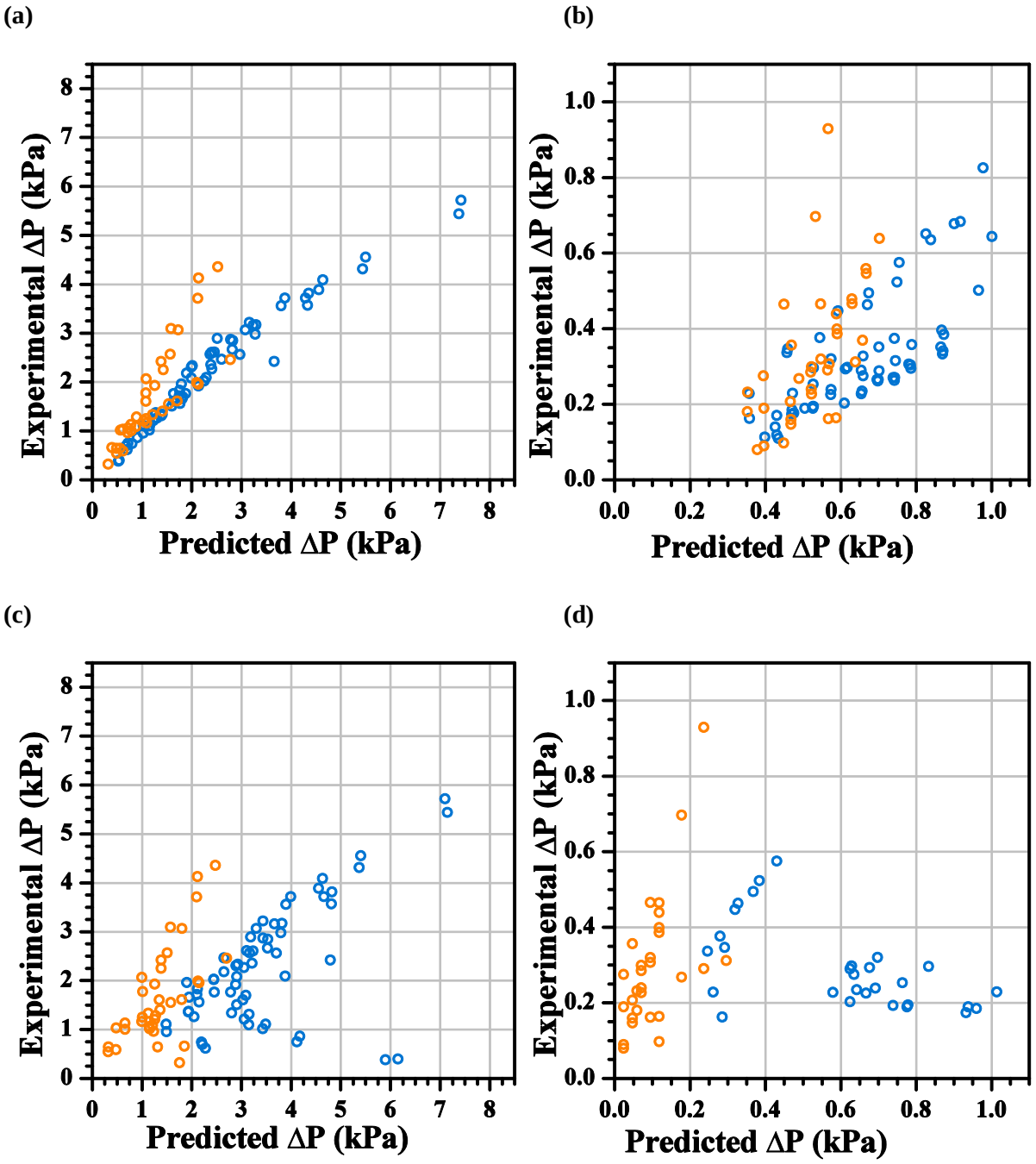

Figure 44 – Comparison between Grimm, See, and Kandlikar correlation and database

Cell temperature 40° C, Orange – 0% RH Inlet, Blue – 95% RH Inlet,
(a) "Slug Correlation" Cathode Pressure Drop (b) "Slug Correlation" Anode Pressure Drop
(c) "Film Correlation" Cathode Pressure Drop (d) "Film Correlation" Anode Pressure Drop

The mean errors for cathode and anode for six correlations are summarized in Table 9. While most provided reasonable mean error, the Modified English and Kandlikar model is suggested due to its low error and the incorporation of quality to allow for better prediction of relatively low qualities and slug flow over the traditional English and Kandlikar model. Although the modified model showed only marginal improvement overall error, in very low superficial gas velocity conditions it provided significantly better prediction. The specialized model proposed by Grimm et al. showed excellent prediction under very specific sets of conditions. However, the transition criteria provided did not match the visual observations of the two-phase flow and presents a substantial roadblock to its widespread application.

Table 9 – Comparison of Mean Error for Selected Correlations

Correlation	Mean error (Cathode 100% RH)	Mean error (Cathode)	Mean error (Anode)
Mishima and Hibiki	13.0%	23.7%	56.1%
English and Kandlikar	5.4%	11.6%	48.7%
Lee and Lee	13.8%	24.3%	56.7%
Saisorn and Wongwises	18.5%	25.4%	55.7%
Modified English and Kandlikar	5.2%	11.6%	40.2%
Grimm et al. "Slug Correlation"	6.5% (3.2%)*	8.8%	106.0%
Grimm et al. "Film Correlation"	137.8%	70.8%	893.3%

*Error when only averaged over conditions where slug flow was seen

5.6.1. Anode Pressure Drop

As noted in Section 5.6, for prediction of anode pressure drop the relative error was quite high. However the average pressure drop on the anode side of the PEM fuel cell was below 1.0 kPa. This relatively low pressure drop, compared to the pressure drop measured on the cathode side. Other minor losses and effects, such as solenoid valve switching can cause significant variation on the order of 0.30 kPa. In Figure 45, the absolute error of the predictions with a fully humidified inlet and MRC-105 GDL are shown. The absolute error for the anode does not exceed 0.35 kPa, while the absolute error of the cathode can be as high as 0.60 kPa. Despite the high relative error, the absolute error is typically lower on the anode side.

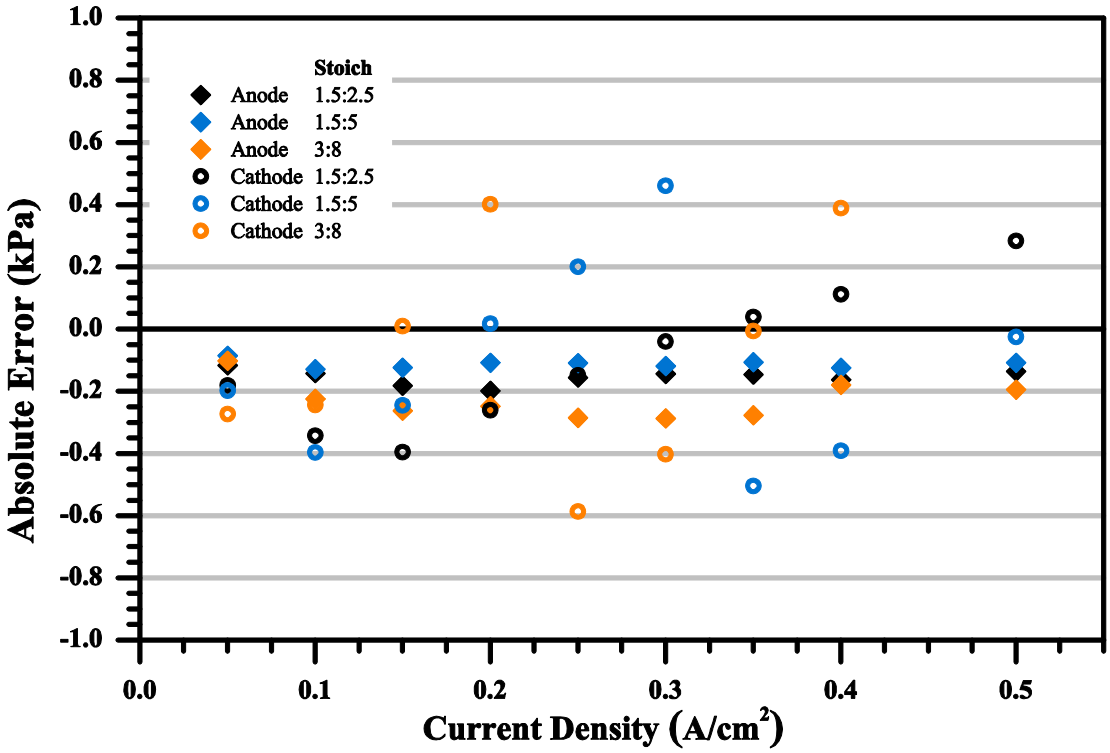

Figure 45 – Summary of Absolute Error

MRC-105 GDL, Fully Humidified Inlet, Cell temperature 40 °C

5.6.2. Pressure Drop under Membrane Dryout Conditions

As stated in Section 5.6, with a dry inlet significant under-prediction of pressure drop was noted for all correlations. As summarized in Table 9, the mean error over all cathode conditions is significantly higher than that of only the fully humidified conditions for almost all correlations. The largest error was primarily seen in selected dry conditions. While some conditions with a dry inlet are well predicted, others have significant error as shown in Figure 46.

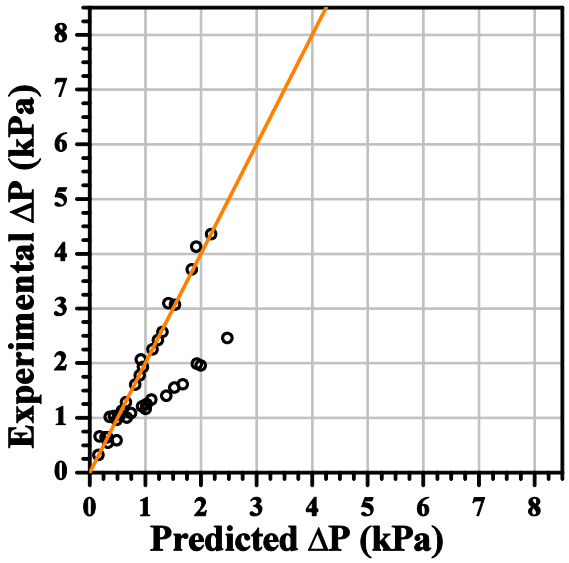

Figure 46 – Modified English and Kandlikar correlation for Cathode with dry inlet.

Across all correlations, as shown in Figures 38-43, two distinct trends are seen in each dry dataset. After analyzing the conditions which are severely under-predicted, it was seen that all were during a severe dry condition (i.e. high current density and stoichiometry). Membrane dehydration was observed during all of these conditions, and verified through HFR measurement. The orange line in Figure 46 has a slope of 2, illustrating an under prediction of 100%. Conditions that were identified as a "dryout" condition, in which membrane dehydration was likely, were predicted with a mean error of approximately 5% when using this adjustment. This in turn allows for the use of pressure drop in a non-visualization cell to be used to identify a "dryout" condition without additional instrumentation. This is extremely advantageous as other methods such as HFR can require additional equipment and introduces AC signal into the load causing variation.

6. Conclusions

A two-phase 1-D pressure drop modeling scheme has been developed that incorporates a step-wise marching technique and control volume analysis to incorporate the key issues presented. The model provides a basis for extending fundamental adiabatic two-phase flow literature to pressure drop within PEMFC reactant channels. In order to develop this modeling scheme, an exhaustive experimental study of two-phase flow within PEM fuel cells was performed and subsequently provided the following contributions the PEM fuel cell research community:

Contribution #1

- Implemented two small scale PEM fuel cells which represent actual automotive geometry using both traditional and optically transparent materials

Contribution #2

- Developed a large database of pressure drop, performance, and visual data targeted at low operating temperature and current density
  - 198 experimental tests representing over 500 hours of PEM fuel cell data acquisition and over 1500 hours of operation were systematically run to cover the relevant ranges of operating parameters for authomotive fuel cells

Contribution #3

- Developed a 1D PEM fuel cell gas channel two-phase pressure drop modeling scheme
  - Expansion of an elemental modeling technique for two-phase flows for two-phase pressure drop analysis
  - Provide methodology for characterization and prediction of local water saturation in PEMFC gas channels

Based on the study performed in this work the following conclusions are drawn:

- The performance of the baseline and visualization fuel cells was comparable under low current density operation. Under higher current density operation the lack of cooling caused performance degradation in the visualization cell due to membrane dehydration. The visualization cell saw comparable performance between GDLs, and with a dry inlet performance decreased with increasing stoichiometry.
- The effect of thermal gradients along the channel length was studied using the visualization cell. The thermal gradient within the PEM fuel cell was seen to vary with stoichiometry, GDL, and inlet humidity. The Freudenberg GDL showed the largest gradient on the cathode side, while the MRC-105 showed the largest gradient on the anode. A large positive temperature gradient allowed for significant water transport in the vapor phase, thus reducing the two-phase multiplier.
- Through visual observation, two-phase flow events such as water ejection, droplet movement, and the development and coalescence of droplets into small films were correlated to pressure drop signatures. Despite the appearance of timescales as short as 30 seconds could provide a representative sample, longer time scales were required as large fluctuations were seen in the overall trend as far as 1000 seconds apart.
- The use of a combination of elemental modeling techniques and methodology for characterization and prediction of local water saturation provided a modeling scheme which achieved reasonable error with 6 correlations from literature. The use of the Modified English and Kandlikar correlation is suggested for use due to its mean error of approximately 5% over the primary conditions of interest and ease of calculation.
- Using the model developed in this work, a “dryout” condition in a non-visualization cell can be identified using pressure drop data without additional instrumentation. Conditions that were identified as “dryout”, in which membrane dehydration was likely, were observed to be under-predicted by 100% within a 5% mean error.

This modeling scheme can be used for the prediction of pressure drop within experimental and commercial PEM fuel cells and subsequently accelerate system design. This ability to precisely predict pressure drop within the PEMFC allows for accurate sizing of the auxiliaries of a PEMFC stack and allow for shorter design cycle. The incorporation of localized condition prediction minimizes the need for modifications to commercial hardware for two-phase condition monitoring. The prediction of pressure drop in a dry-out condition provides an additional diagnostic method to monitor the potential for membrane dehydration and performance degradation. The model provides a unique and comprehensive basis for extending fundamental adiabatic two-phase flow pressure drop models available in the literature to PEMFC reactant channels.

7. Recommendations for Future Work

The investigation of two-phase flow within PEM fuel cell reactant channels is critical to the performance and optimization of thermal and water management. The newly developed method of modeling has opened several areas of interest within PEMFC research.

7.1. Sub-Component Model Investigation

Sub-component models within the modeling scheme merit further in depth analysis and additional intensive modeling efforts. Specifically, net water drag and evaporation rates within microchannels merit further research and analysis within the modeling scheme.

7.2. Fundamental Investigation of Pressure Drop due to Flow Structures

While this modeling scheme analyzes pressure drop in PEMFCs from a systems level approach, a fundamental understand of how each flow structure (slugs, films, and mist) affect the pressure drop in a micro channeled system. The measurement of the pressure drop required to remove a slug from a reactant channel, analysis of film morphology, and parametric studies of flow structures observed within PEM fuel cell reactant channels would provide a further understanding of the phenomena.

7.3. Expansion of Operating Conditions

This work focuses on key operating ranges where significant liquid water is seen within the reactant channels of PEM fuel cells. Further expansion of the already extensive database would further aid in the understanding of two-phase flow within PEM fuel cells throughout the entire range of operating conditions.

7.4. Transient Pressure Drop Analysis

This work focuses on the steady state prediction of pressure drop and its implications on performance. Significant value is seen in the extension of the work to include transience within the two-phase flow and pressure drop under changing operating conditions.

8. References

[1] Bosco, Fronk, 2000, “Fuel cell flooding detection and correction.”

[2] Anderson R., Zhang L., Ding Y., Blanco M., Bi X., and Wilkinson D. P., 2010, “A critical review of two-phase flow in gas flow channels of proton exchange membrane fuel cells,” Journal of Power Sources, **195**(15), pp. 4531–4553.

[3] Kandlikar S. G., Garimella S., Li D., Colin S., and King M. R., 2006, Heat Transfer and Fluid Flow in Minichannels and Microchannels, Elsevier.

[4] Mishima K., and Hibiki T., 1996, “Some characteristics of air-water two-phase flow in small diameter vertical tubes,” International Journal of Multiphase Flow, **22**(4), pp. 703–712.

[5] Saisorn S., and Wongwises S., 2008, “An inspection of viscosity model for homogeneous two-phase flow pressure drop prediction in a horizontal circular micro-channel,” International Communications in Heat and Mass Transfer, **35**(7), pp. 833–838.

[6] Dukler, A. E., Wicks, M. and Cleveland, R. G., 1964, “Frictional pressure drop in two-phase flow,” AIChE J., **10**, pp. 44–51.

[7] R. W. Lockhart and R. C. Martinelli, 1949, Chemical Engineering Progress, **45**, p. 39.

[8] Chisholm D., 1967, “A theoretical basis for the Lockhart-Martinelli correlation for two-phase flow,” International Journal of Heat and Mass Transfer, **10**(12), pp. 1767–1778.

[9] Nathan J. English and Satish G. Kandlikar, 2006, “An Experimental Investigation into the Effect of Surfactants on Air-Water Two-Phase Flow in Minichannels,” Heat Transfer Engineering, **27**(4), pp. 99–109.

[10] Ju Lee H., and Yong Lee S., 2001, "Pressure drop correlations for two-phase flow within horizontal rectangular channels with small heights," International Journal of Multiphase Flow, **27**(5), pp. 783–796.

[11] Saisorn S., and Wongwises S., 2010, "The effects of channel diameter on flow pattern, void fraction and pressure drop of two-phase air–water flow in circular micro-channels," Experimental Thermal and Fluid Science, **34**(4), pp. 454–462.

[12] Hibiki T., and Mishima K., 2001, "Flow regime transition criteria for upward two-phase flow in vertical narrow rectangular channels," Nuclear Engineering and Design, **203**(2–3), pp. 117–131.

[13] Sun L., and Mishima K., 2009, "Evaluation analysis of prediction methods for two-phase flow pressure drop in mini-channels," International Journal of Multiphase Flow, **35**(1), pp. 47–54.

[14] Zhao T. ., and Bi Q. ., 2001, "Pressure drop characteristics of gas–liquid two-phase flow in vertical miniature triangular channels," International Journal of Heat and Mass Transfer, **44**(13), pp. 2523–2534.

[15] Chung P. M.-Y., and Kawaji M., 2004, "The effect of channel diameter on adiabatic two-phase flow characteristics in microchannels," International Journal of Multiphase Flow, **30**(7–8), pp. 735–761.

[16] Grimm M., See E. J., and Kandlikar S. G., "Modeling gas flow in PEMFC channels: Part I – Flow pattern transitions and pressure drop in a simulated ex situ channel with uniform water injection through the GDL," International Journal of Hydrogen Energy.

[17] Mench M. ., Dong Q. ., and Wang C. ., 2003, "In situ water distribution measurements in a polymer electrolyte fuel cell," Journal of Power Sources, **124**(1), pp. 90–98.

[18] Xiao-Guang Yang, Nick Burke, Chao-Yang Wang, Kazuya Tajiri, and Kazuhiko Shinoharab, 2005, "Simultaneous Measurements of Species and Current Distributions in a PEFC under Low-Humidity Operation," Journal of The Electrochemical Society, **152**(4), pp. A759–A766.

[19] Chao-Yang Wang*, 2004, "Fundamental Models for Fuel Cell Engineering," Chemical Review, **104**, pp. 4727–4766.

[20] Gu W., Baker D. R., Liu Y., and Gasteiger H. A., 2009, Proton Exchange Membrane Fuel Cell (PEMFC) Down-the-Channel Performance Model, in Handbook of Fuel Cells, John Wiley & Sons, England.

[21] Lu G. Q., Liu F. Q., and Wang C.-Y., 2007, "An approach to measuring spatially resolved water crossover coefficient in a polymer electrolyte fuel cell," Journal of Power Sources, **164**(1), pp. 134–140.

[22] A. Ullmann and N. Brauner, 2007, "The Prediction of Flow Pattern Maps In Mini Channels," Multiphase Science and Technology, **19**, pp. 49–73.

[23] Y. Taitel, 1990, "Flow pattern transition in two phase flow," 9th International Heat Transfer Conference, pp. 237–254.

[24] Kandlikar S. G., Lu Z., Domigan W. E., White A. D., and Benedict M. W., 2009, "Measurement of flow maldistribution in parallel channels and its application to ex-situ and in-situ experiments in PEMFC water management studies," International Journal of Heat and Mass Transfer, **52**(7–8), pp. 1741–1752.

[25] Lu Z., Kandlikar S. G., Rath C., Grimm M., Domigan W., White A. D., Hardbarger M., Owejan J. P., and Trabold T. A., 2009, "Water management studies in PEM fuel cells, Part II:

Ex situ investigation of flow maldistribution, pressure drop and two-phase flow pattern in gas channels," International Journal of Hydrogen Energy, **34**(8), pp. 3445–3456.

[26] Lu Z., Rath C., Zhang G., and Kandlikar S. G., 2011, "Water management studies in PEM fuel cells, part IV: Effects of channel surface wettability, geometry and orientation on the two-phase flow in parallel gas channels," International Journal of Hydrogen Energy, **36**(16), pp. 9864–9875.

[27] Kandlikar S. G., Lu Z., Lin T. Y., Cooke D., and Daino M., 2009, "Uneven gas diffusion layer intrusion in gas channel arrays of proton exchange membrane fuel cell and its effects on flow distribution," Journal of Power Sources, **194**(1), pp. 328–337.

[28] Sergi J. M., and Kandlikar S. G., 2011, "Quantification and characterization of water coverage in PEMFC gas channels using simultaneous anode and cathode visualization and image processing," International Journal of Hydrogen Energy, **36**(19), pp. 12381–12392.

[29] Gopalan P., and Kandlikar S. G., 2012, "Droplet-Sidewall Dynamic Interactions in PEMFC Gas Channels," Journal of Electrochemical Society, **159**(8), pp. F1–F8.

[30] Dai W., Wang H., Yuan X.-Z., Martin J. J., Yang D., Qiao J., and Ma J., 2009, "A review on water balance in the membrane electrode assembly of proton exchange membrane fuel cells," International Journal of Hydrogen Energy, **34**(23), pp. 9461 – 9478.

[31] Atiyeh H. K., Karan K., Peppley B., Phoenix A., Halliop E., and Pharoah J., 2007, "Experimental investigation of the role of a microporous layer on the water transport and performance of a PEM fuel cell," Journal of Power Sources, **170**(1), pp. 111–121.

[32] Kuhn R., Krüger P., Kleinau S., Dawson M., Geyer J., Roscher M., Manke I., and Hartnig C., 2012, "Dynamic fuel cell gas humidification system," International Journal of Hydrogen Energy, **37**(9), pp. 7702–7709.

[33] US Department of Energy, 2007, Hydrogen, fuel cells, and infrastructure technology programs: multi-year research, development and demonstration plan, Section 3.4 fuel cells.

[34] Hentall P. L., Lakeman J. B., Mepsted G. O., Adcock P. L., and Moore J. M., 1999, "New materials for polymer electrolyte membrane fuel cell current collectors," Journal of Power Sources, **80**(1-2), pp. 235–241.

[35] W A HAMMOND DRIERITE CO LTD, 2012, "DRIERITE DESICCANTS." www.drierite.com.

[36] W. M. Kays and A. L. London, 1984, Compact Heat Exchangers, McGraw Hill, New York.

[37] Mench M. M., 2008, Fuel Cell Engines, John Wiley & Sons, Inc., Hoboken, New Jersey.

[38] Tsilingiris P. T., 2008, "Thermophysical and transport properties of humid air at temperature range between 0 and 100 °C," Energy Conversion and Management, **49**(5), pp. 1098–1110.

[39] Jacqueline M. Sergi, 2011, "Characterization of Two-Phase Flow in a Transparent PEM Fuel Cell using Simultaneous Anode and Cathode Visualization and Digital Image Processing."

9. Appendix

9.1. Equations for the calculation of Chisholm Parameter

Lee and Lee

$$C = A * Re_L^r * \lambda^q * \psi^b$$

Saisorn and Wongwises

$$C = 7.599x10^{-3} * \lambda^{-0.631} * \varphi^{0.005} * Re_L^{-0.008}$$

Mishima and Hibiki

$$C = 21\left(1 - e^{-.319D_h}\right)$$

English and Kandlikar

$$C = 5\left(1 - e^{-.319D_h}\right)$$

Grimm, See, and Kandlikar - Mass Quality Adjusted

$$C = C^* * 5\left(1 - e^{-.319D_h}\right)$$

$$C^* = A\left(\frac{1-x}{x}\right)^b ; \quad A = 0.0856(u_L)^{-1.202} ; \quad b = 0.004(u_L)^{-0.526}$$

Grimm, See, and Kandlikar - Flow Regime Differentiated

Slug

$$C = 0.772 Re_L^{0.051} \lambda^{0.016} \psi^{-1.716} X^{0.034}$$

Film

$$C = 1.9087 Re_L^{-0.405} \lambda^{-0.134} \psi^{-0.421} \chi^{-0.107}$$

where:

$$Re_L = \frac{\rho_L U_L D_h}{\mu_L} ; \quad \lambda = \frac{\mu_L^2}{\rho_L \sigma D_h} ; \quad \psi = \frac{\mu_L (U_G + U_L)}{\sigma} ; \quad \chi = \frac{1-x}{x}$$

9.2. Laser confocal imagery of selected GDLs

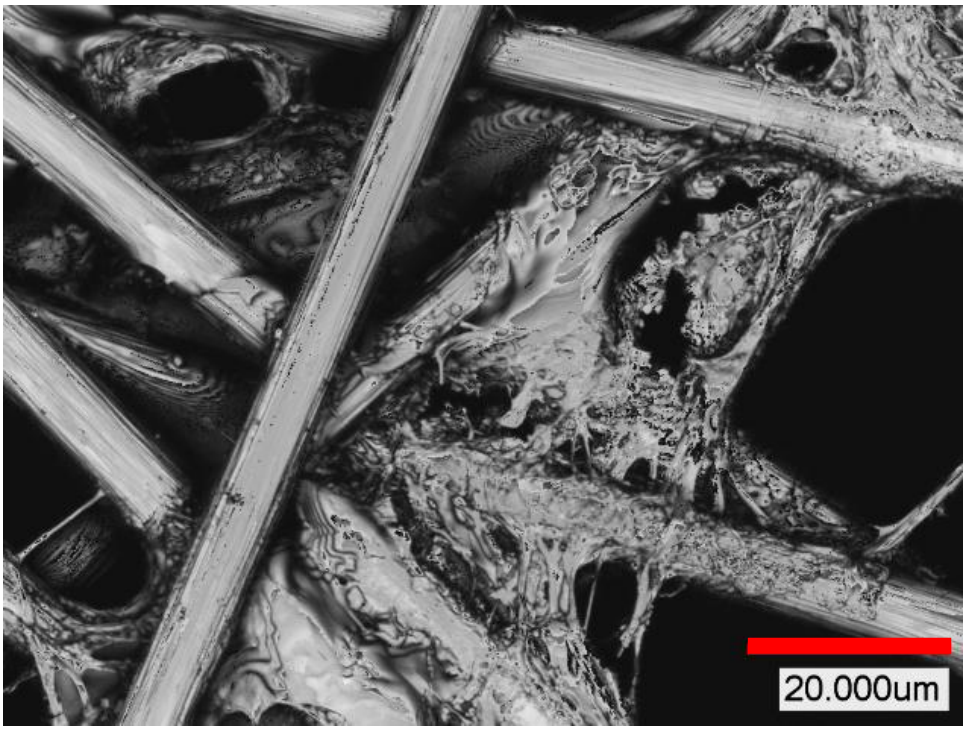

Figure 47 – Laser confocal microscopy image of MRC-105 GDL

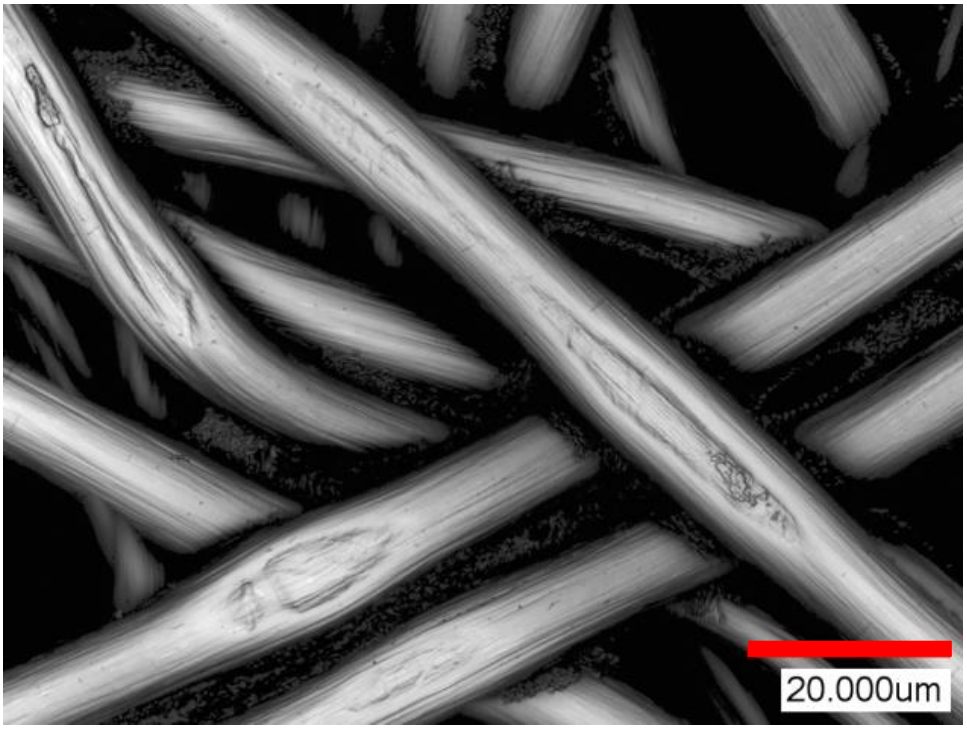

Figure 48 – Laser confocal microscopy image of Freudenberg GDL

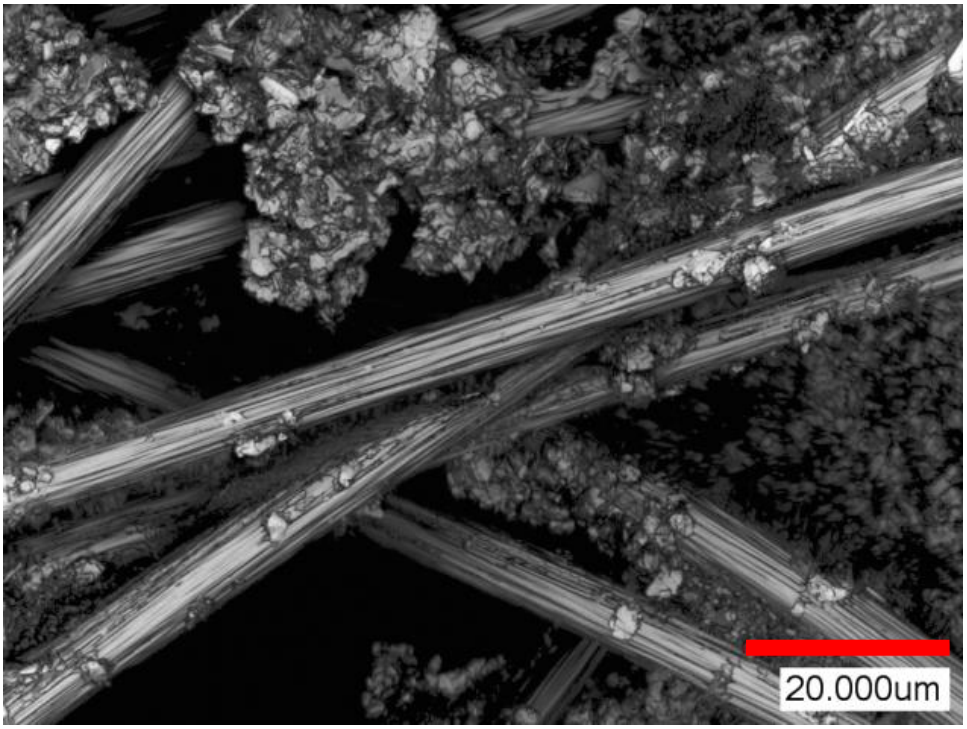

Figure 49 – Laser confocal microscopy image of SGL-25BC GDL

9.3. Appendix - List of Tested Conditions

Visualization Cell

GDL	Stoich	Inlet RH	Current Density
SGL 25BC	1.5/2.5	0	0.05
			0.10
			0.15
			0.20
			0.25
			0.30
	1.5/5		0.05
			0.10
			0.15
			0.20
			0.25
			0.30
			0.35
			0.40
	3/8		0.05
			0.10
			0.15
			0.20
			0.25
			0.30
			0.35
	1.5/2.5	100	0.05
			0.10
			0.15
			0.20
			0.25
			0.30
			0.35
			0.40
			0.45
	1.5/5		0.05
			0.10
			0.15
			0.20
			0.25
			0.30
			0.35
			0.40
			0.50
			0.60
	3/8		0.05
			0.10
			0.15
			0.20
SGL 25BC	3/8	100	0.25
			0.30
			0.35
			0.40
			0.50
			0.60
Freudenberg	1.5/2.5	100	0.05
			0.10
			0.15
			0.20
			0.25
			0.30
			0.35
			0.40
			0.50
			0.60
			0.05
			0.10
			0.15
			0.20
			0.25
			0.30
			0.35
			0.40
			0.50
Baseline	1.5/2.5	100	0.05
			0.10
			0.15
			0.20
			0.25
			0.30
			0.35
			0.40
			0.50
	1.5/5		0.05
			0.10
			0.15
			0.20
			0.25
			0.30
			0.35
			0.40
			0.50
	3/8		0.05
			0.10
			0.15
			0.20

GDL	Stoich	Inlet RH	Current Density
MRC-105	3/8	100	0.25
			0.30
			0.35
			0.40
			0.50
	1.5/2.5	0	0.05
			0.10
			0.15
			0.20
			0.25
			0.30
			0.35
			0.40
	1.5/5		0.05
			0.10
			0.15
			0.20
			0.25
			0.30
			0.35
	3/8		0.05
			0.10
			0.15
			0.20
Freudenberg	1.5/2.5	100	0.05
			0.10
			0.15
			0.20
			0.25
			0.30
			0.35
			0.40
			0.50
			0.60
	1.5/5		0.05
			0.10
			0.15
			0.20
			0.25
			0.30
			0.35
			0.40
			0.50
	3/8		0.05
			0.10
			0.15
			0.20

GDL	Stoich	Inlet RH	Current Density
Freudenberg	3/8	100	0.25
			0.30
			0.35
			0.40
			0.50
			0.60
	1.5/5		0.05
			0.10
			0.15
			0.20
			0.25
			0.30
			0.35
			0.40
			0.50
			0.60
	1.5/2.5	0	0.05
			0.10
			0.15
			0.20
			0.25
			0.30
			0.35
	1.5/5		0.05
			0.10
			0.15
			0.20
			0.25
			0.30
	1.5/2.5		0.05
			0.10
			0.15
			0.20
			0.25
Toray 060	1.5/2.5	100	0.05
			0.10
			0.15
			0.20
			0.25
			0.30
			0.35
			0.40
			0.50
			0.60

Baseline Cell

GDL	Stoich	Inlet RH	Current Density
MRC-105	3/3	100	0.10
			0.10
			0.10
	1.5/2		0.40
			0.40
			0.70
			0.70
			0.40
			1.00
			1.00
			0.40
			0.40

9.4. LabVIEW code for data acquisition

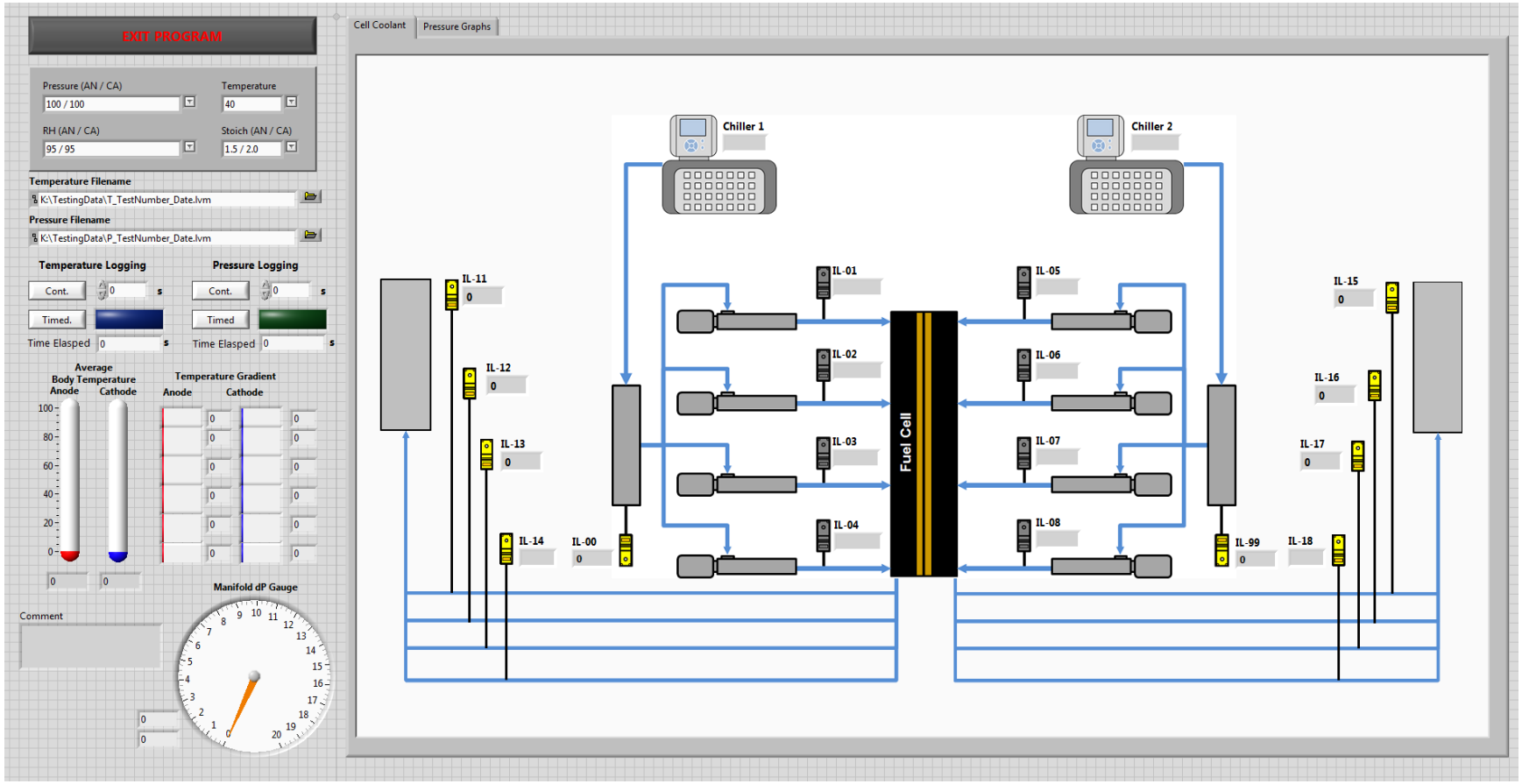

Figure 50 – Front panel of the data acquisition VI

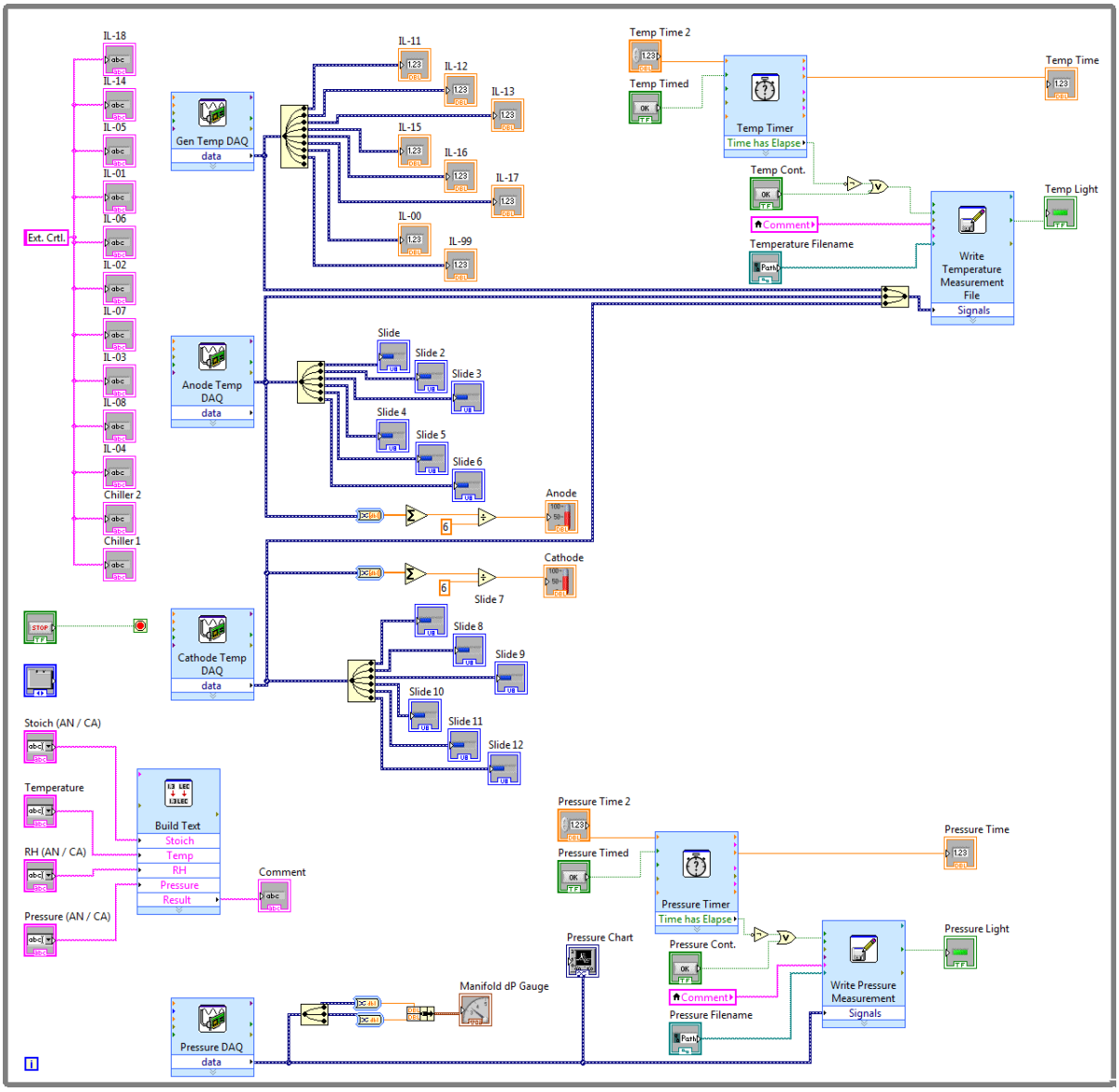

Figure 51 – Block diagram of data acquisition VI